UC San Diego

UC San Diego Electronic Theses and Dissertations

Title

Advanced characterization and modeling of next generation lithium ion electrodes and interfaces

Permalink

https://escholarship.org/uc/item/0x9564q0

Author

Wynn, Thomas Andrew

Publication Date

2020

Peer reviewed|Thesis/dissertation

UNIVERSITY OF CALIFORNIA SAN DIEGO

Advanced characterization and modeling of next generation lithium ion electrodes and interfaces

A dissertation submitted in partial satisfaction of the
requirements for the degree Doctor of Philosophy

in

Materials Science and Engineering

by

Thomas Andrew Wynn

Committee in charge:

Professor Ying Shirley Meng, Chair
Professor David Fenning
Professor Eric Fullerton
Professor Javier Garay
Professor Shyue Ping Ong

2020

The Dissertation of Thomas Andrew Wynn as it is listed on UC San Diego Academic Records is approved, and it is acceptable in quality and form for publication on microfilm and electronically:

_____

_____

_____

_____

_____
Chair

University of California San Diego

2020

DEDICATION

To my family.

TABLE OF CONTENTS

LIST OF FIGURES

ix

LIST OF TABLES

ACKNOWLEDGEMENTS

I would like to acknowledge Professor Shirley Meng for her support and guidance as the chair of my committee and as my academic advisor, helping me grow as a scientist and a human. Despite juggling countless roles, Shirley was always ready with answers and advice, and provided me with countless opportunities for which I am grateful.

To my committee members for their time and support.

To the Thin Film Crew, Dylan Cheng, Ryosuke Shimizu, Dr. Jungwoo Lee, Dr. Thomas Brenner, Dr. Jean-Marie Doux, Dr. Xuefeng Wang, and Dr. Cyrus Rustomji. Their help and discussion made all this work possible.

To all the LESC team, past and present, for the good times and boundless help.

To my collaborators and coauthors through the years, Dr. Maxwell Marple, Dr. Jamie Weaver, Dr. Rohan Dhall, Dr. Khim Karki, Dr. Nancy Dudney, Dr. Huolin Xin, Dr. Kang Xu, Dr. Marshall Schroeder, Prof. Kuan-Zung Fung.

And to my family, for their endless patience and support.

Chapter 3, in part, is a reprint of the material as it appears in the Journal of Materials Chemistry A. Wynn, Thomas A.; Fang, Chengcheng; Zhang, Minghao; Liu, Haodong; Davies,

Daniel M.; Wang, Xuefeng; Lau, Derek; Lee, Jungwoo Z.; Huang, Bo-Yuan; Fung, Kuan-Zong; Ni, Chung-Ta; Meng, Ying Shirley, Journal of Materials Chemistry A, 6 (2018) 24651-24659. The dissertation/thesis author was the co-primary investigator and author of this paper.

Chapter 6, in part, is a reprint of the material as it appears in the MRS Bulletin and the Journal of Visualized Experiments. Wynn, Thomas A.; Lee, Jungwoo Z.; Banerjee, Abhik,; Meng, Ying Shirley, MRS Bulletin, 43 (2018) 768-774 and Lee, Jungwoo Z.; Wynn, Thomas A.; Meng, Ying Shirley; Santhanagopalan, Dhamodaran, Journal of Visualized Experiments, 133 (2018) e56259. The dissertation/thesis author was the co-primary investigator and co-first author of these papers.

2009	Bachelor of Science, The Ohio State University
2009-2013	Research Technologist, Los Alamos National Laboratory
2013-2015	Teaching Assistant, University of California, Davis
2015	Master of Science, University of California, Davis
2015-2020	Research Assistant, University of California, San Diego
2020	Doctor of Philosophy, University of California, San Diego

PUBLICATIONS

(* authors contributed equally to the work)

B. Qiu, M. Zhang, S.-Y. Lee, H. Liu, Y. Xia, **T.A. Wynn**, L. Wu, Y. Zhu, W. Wen, C. Brown, Z. Liu, Y.S. Meng, "Structural metastability and reversibility in an anionic-redox-based cathode for next generation high energy rechargeable battery", Cell Reports Physical Science, 1, 100028 (2020).

E. Zhao, M. Zhang, X. Wang, E. Hu, J. Liu, X. Yu, M. Olguin, **T.A. Wynn**, Y.S. Meng, K. Page, F. Wang, H. Li, X.-Q. Yang, X. Huang, L. Chen, "Local Structure Adaptability through Multi Cations for Oxygen Redox Accommodation in Li-Rich Layered Oxides", Energy Storage Materials, 24, 384 (2020).

A. Banerjee, H. Tang, X. Wang, J. Cheng, M. Zhang, H. Nguyen, D. Tan, **T.A. Wynn**, E. Wu, J.-M. Doux, T. Wu, L. Ma, G. Sterbinsky, M. Dsouza, S.P. Ong, Y.S. Meng, "Revealing nanoscale solid-solid interfacial phenomena for long life high energy all-solid-state batteries", ACS Applied Materials & Interfaces, 11, 43138 (2019).

*J. Z. Lee, ***T.A. Wynn**, M.A. Schroeder, J. Alvarado, X. Wang, K. Xu, Y.S. Meng, "Cryogenic focused ion beam characterization of lithium metal anodes", ACS Energy Letters, 4, 489 (2019). *co-first authorship.

J. Alvarado, M. A. Schroeder, T.P. Pollard, X. Wang, J.Z. Lee, M. Zhang, **T.A. Wynn**, M. Ding, O. Borodin, Y.S. Meng, K. Xu, "Bisalt ether electrolyte for coupling lithium metal with high nickel content cathodes". Energy & Environmental Science, 12, 780-794 (2019).

T.A. Wynn, J.Z. Lee, A. Banerjee, Y.S. Meng, "In situ and operando probing of solid-solid interfaces in electrochemical devices", Invited perspective to the MRS Bulletin, 43, 768 (2018).

*T.A. Wynn, *C. Fang, M. Zhang, H. Liu, D.M. Davies, X. Wang, D. Lau, J.Z. Lee, B.-Y. Huang, K.-Z. Fung, C.-T. Ni, Y.S. Meng, "Mitigating oxygen release in anionic-redox-active cathode materials by cationic substitution through rational design", Journal of Materials Chemistry A, 5, 24651 (2018).

A. Singer, M. Zhang, S. Hy, D. Cela, C. Fang, **T.A. Wynn**, B. Qiu, Y. Xia, Z. Liu, A. Ulvestad, N. Hua, J. Wingert, H. Liu, M. Sprung, A. V. Zozulya, E. Maxey, R. Harder, Y. S. Meng, O. G. Shpyrko, "Nucleation of dislocations and their dynamics in layered oxide cathode materials during battery charging", Nature Energy, 3, 641 (2018).

*J.Z. Lee, ***T.A. Wynn**, D. Sanagopolan, Y.S. Meng, "Focused ion beam fabrication of LiPON-based solid-state lithium-ion nanobatteries for in situ testing", Journal of Visualized Experiments, 133 (2018). *co-first authorship

J.Z. Lee, Z. Wang, H.L. Xin, **T.A. Wynn**, Y.S. Meng, "Amorphous lithium lanthanum titanate for solid-state microbatteries", Journal of the Electrochemical Society, 164, A6268 (2017).

R.V. Chopdekar, B. Li, **T.A. Wynn**, M.S. Lee, Y. Jia, Z.Q. Liu, M.D. Biegalski, S.T. Retterer, A.T. Young, A. Scholl, Y. Takamura, "Nanostructured complex oxides as a route toward thermal behavior in artificial spin ice systems", Physical Review Materials, 1, 024401 (2017).

M.S. Lee, **T.A. Wynn**, E. Folven, R.V. Chopdekar, A. Scholl, S.T. Retterer, J.K. Grepstad, Y. Takamura, "Temperature dependence of ferromagnetic-antiferromagnetic spin alignment and coercivity in epitaxial micromagnetic bilayers", Physical Review Materials, 1, 014402 (2017).

*M.S. Lee, ***T.A. Wynn**, E. Folven, R.V. Chopdekar, A. Scholl, A.T. Young, S.T. Retterer, J.K. Grepstad, Y. Takamura, "Tailoring spin textures in complex oxide microstructures", ACS Nano, 10, 8545 (2016). *co-first authorship

C.-F. Chen, Q.R. Marksteiner, M.T. Reiten, **T.A. Wynn**, D.R. Guidry, "Lamination of magnesium oxide spacers to barium strontium zirconium titanate ceramics", Journal of Materials Science, 49, 5218 (2014).

J.S. Carpenter, R.J. McCabe, S.J. Zheng, **T.A. Wynn**, N.A. Mara, I.J. Beyerlein, "Processing Parameter Influence on Texture and Microstructural Evolution in Cu-Nb Multilayer Composites Fabricated via Accumulative Roll Bonding", Metallurgical and Material Transactions A, 45, 2192 (2014).

C.-F. Chen, Q.R. Marksteiner, G. King, **T.A. Wynn**, M.B. Treiman, D.A. Dalmas, A. Llobet, W. B. Haynes, D.R. Guidry, P.A. Papin, "Slip Casting of Sol-Gel Synthesized Barium Strontium Zirconium Titanate Ceramics", Journal of Materials Science, 48, 5788, (2013).

N.A. Mara, J. Crapps, **T.A. Wynn**, K. Clarke, A. Antoniou, P. Dickerson, D.E. Dombrowski, B.

Mihaila, "Microcantilever Bend Testing and Finite-Element Simulations of Al-Al HIP Bonded Interfaces", Philosophical Magazine, 93, 2749 (2013).

J.S. Carpenter, R.J. McCabe, I.J. Beyerlein, **T.A. Wynn**, N.A. Mara, "A Wedge-Mounting Technique for Nanoscale Electron Backscatter Diffraction", Journal of Applied Physics, 113, 094304 (2013).

K.J. Hollis, N.A. Mara, R.D. Field, **T.A. Wynn**, P.O. Dickerson, "Bond Strength Characterization of Plasma Sprayed Zirconium on Uranium Alloy by Microcantilever Testing", Journal of Thermal Spray Technology, 22, 233, (2013).

T.A. Wynn, D. Bhattacharyya, D. Hammon, A. Misra, N.A. Mara, "Large Strain Deformation of Bimodal Layer Thickness Cu/Nb Nanolaminar Composites", Materials Science and Engineering: A, 564, 213 (2013).

I.J. Beyerlein, N.A. Mara, J.S. Carpenter, T. Nizolek, W. Mook, **T.A. Wynn**, R. McCabe, J. Mayeur, K. Kang, S.J. Zheng, J. Wang, T.M. Pollock, "Interface-driven microstructure development and ultra high strength of bulk nanostructured Cu/Nb multilayers fabricated by severe plastic deformation", Journal of Materials Research, 28, 1799, (2013).

E.J. Payton, **T.A. Wynn**, M.J. Mills, "Experimental measurement of the kinetics of gamma prime dissolution during supersolvus heat treatment of powder metallurgical Ni-base disk superalloys", Journal of Materials Science, 47, 7305, (2012).

M. Tang, **T.A. Wynn**, M.K. Patel, J. Won, N.A. Mara, K.E. Sickafus, "Structure and mechanical properties of swift heavy ion irradiated Tungsten-bearing delta-phase oxides $Y_6W_1O_{12}$ and $Yb_6W_1O_{12}$", Journal of Nuclear Materials, 425, 193, (2012).

ABSTRACT OF THE DISSERTATION

Advanced characterization and modeling of next generation lithium ion electrodes and interfaces

by

Thomas Andrew Wynn

Doctor of Philosophy in Materials Science and Engineering

University of California San Diego, 2020

Professor Ying Shirley Meng, Chair

Lithium ion batteries have proven to be a paradigm shifting technology, enabling high energy density storage to power the handheld device and electric automotive revolutions. However relatively slow progress toward increased energy and power density has been made since the inception of the first functional lithium ion battery. Materials under consideration for next generation lithium ion batteries include anionic-redox-active cathodes, solid state electrolytes, and lithium metal anodes. Li-rich cathodes harness anionic redox, showing increased first charge

capacity well beyond the redox capacity of traditional transition metal oxides, though suffer from severe capacity and voltage fade after the first cycle. This is in part attributed to oxygen evolution, driving surface reconstruction. Solid-state electrolytes (SSEs) offer the potential for safer devices, serving as physical barriers for dendrite penetration, while hoping to enable the lithium metal anode. The lithium metal naturally exhibits the highest volumetric energy density of all anode materials.

Here, we employ simulation and advanced characterization methodologies to understand the fundamental properties of a variety of next generation lithium ion battery materials and devices leading to their successes or failures. Using density functional theory, the effect of cationic substitution on the propensity for oxygen evolution was explored. Improvement in Li-rich cathode performance is predicted and demonstrated through doping of 4d transition metal Mo. Next, lithium phosphorus oxynitride (LiPON), an SSE utilized in thin film batteries, was explored. LiPON has proven stable cycling against lithium metal anodes, though its stability is poorly understood. RF sputtered thin films of LiPON are examined via spectroscopic computational methods and nuclear magnetic resonance to reveal its atomic structure, ultimately responsible for its success as a thin film solid electrolyte. A new perspective on LiPON is presented, emphasizing its glassy nature and lack of long-range connectivity. Progress toward in situ methodologies for solid-state interfaces is described, and a protocol for FIB-produced nanobatteries is developed. Cryogenic methodologies are applied to a PEO/NCA composite electrode. Cryogenic focused ion beam was shown to preserve polymer structure and morphology, enabling accurate morphological quantification and preserving the crystallinity, as observed via TEM. Last, development of *in situ* solid-state interface characterization is discussed.

Chapter 1. Background and Introduction

1.1 Lithium ion battery: enabling a revolution

As we the global population rises we observe commensurate increases in global energy demand, with the approximate amount of annual energy consumption has exceeding 150 TWh. This number has increased steadily as populations rise and economies develop. These rises are accompanied by rises in global carbon emissions, which are theorized to be responsible for global climate change with other adverse environmental effects such as reduced air quality as well as the acidification of the oceans. In response to projected increases in energy demand as well as from growing environmental concerns, efforts to move to renewable resources and low-carbon technology are highly sought after. However, despite progress toward functional renewable energies, the percentage of energy derived from fossil fuels remains above 85% (Figure 1.1).[1]
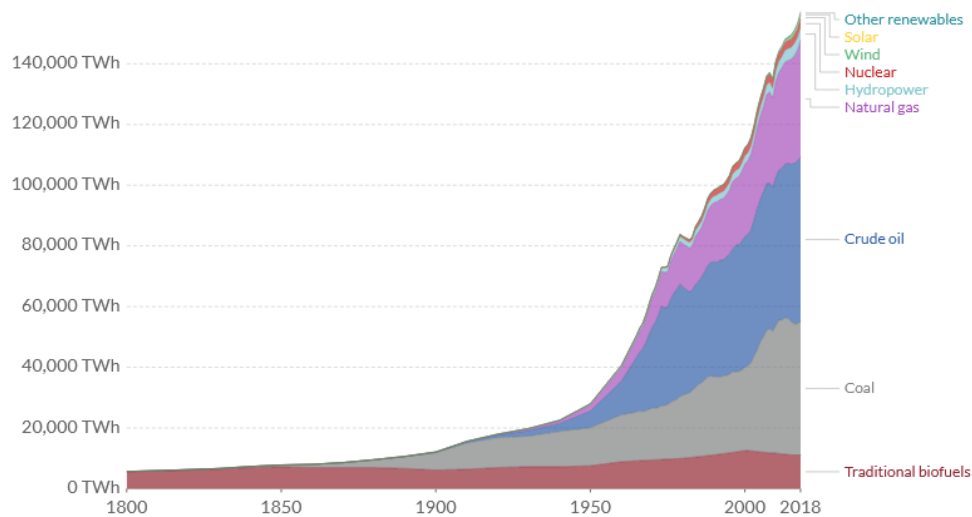
Figure 1.1. Annual trends in global energy consumption by energy source.[1]

To curb carbon emissions, electric vehicles have seen a recent resurgence. Immediately following their implementation by Tesla motors, nearly all major vehicle manufacturers have followed suit, and offer electric and hybrid-electric vehicles—all made possible by the

development of the lithium ion battery (LIB). LIBs have proven to be transformative technology, storing tremendous amounts of energy, enabling handheld devices, powering electric automobiles capable of traveling in excess of 300 miles, and inspiring a grid-storage revolution. However, electric vehicles demand longer ranges due to their limited cycling the limited energy density of the lithium ion battery. Modern vehicles generally consist of packages of commercialized LIB cells, most commonly 18650 type cells, with a specific capacity of 85 kWh. On the system-level, this corresponds to operating ranges nearing 300 miles. In order to increase the range of these vehicles, as well as the lifetime of portable devices, efforts to improve the modern lithium ion battery have been long underway.

1.2 Lithium ion battery: general mechanisms

The modern LIB was enabled by the combination of a robust, electrically conductive intercalation electrode, liquid electrolytes of organic solvents and lithium salts, and the fortunate formation of a stable solid electrolyte interface (SEI) on the surface of the graphitic anode permitted such implementation from Sony in 1991. Despite its success, growing energy consumption is driving the need for longer lasting, more compact, lighter secondary electrochemical storage devices. This need has been attempted to be answered by countless research groups across the globe, performing research on a broad range of next-generation electrochemical devices with improved power, capacity, and safety. Before discussing next generation electrochemical storage devices, we will take a closer look at the operating principles of the modern lithium ion battery.

In general, a lithium-based electrochemical energy storage device exhibits a voltage based on the difference in chemical potential of the Li in the anode and the Li in the cathode (ΔG). This is quantitatively expressed by $\Delta G = -zEF$, where z is charge of the ions, E is the potential, and F

is the Faraday constant.[2] LIB electrodes also require a species capable of accommodating multiple redox states and reversible reactions with the intercalation ion. While studying layered dichalcogenides, a high free energy of reaction with alkali ions was observed, leading to the exploration of TiS_2 (Figure 1.2) as the first lithium intercalation cathode for energy storage. Here, Li ions are stably shuttled in and out of from between the TiS_2 layers, resulting in a change in the chemical potential of lithium.[3] The chemical potential of the cathode itself may be determined by the change in Gibbs free energy observed with the change in the mole fraction of species removed ($\mu_i=\partial G_j/\partial n_i$). Interestingly, a lot can be gleaned from the shape of a potential curve. The Gibbs phase rule, $F = C - P + 2$ dictates that the number of degrees of freedom (F) is coupled by the number of components (C) minus the number of phases (P) minus 2. A flat voltage plateau is so due to the reduced degree of freedom from a the incorporation of a second phase.[2]
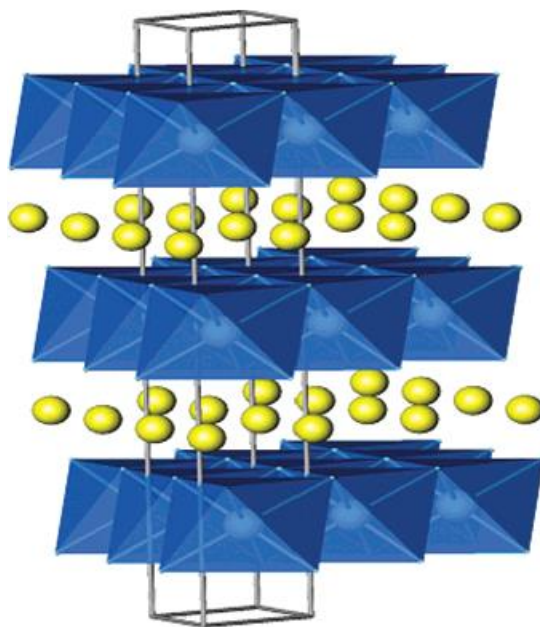
Figure 1.2. Structure of $LiTiS_2$, where Li is yellow and TiS_2 polyhedra are blue.[3]

While the layered dichalcogenides didn't exhibit a phase change, they exhibited relatively low voltages, and were quickly overtaken by layered oxide analogues. $LiMO_2$, where M is a

transition metal, showed generally higher potentials with acceptable electronic conductivities to promote kinetics. The most common layered lithium oxides, $LiNiO_2$, $LiMnO_2$ and $LiCoO_2$, exhibit higher potentials, and hence power density, although both materials have their limitations. $LiCoO_2$ is observed to undergo a phase change when half of the lithium is removed, resulting in large strain accumulation as well as the formation of an insulating phase, and also exhibits a notable drop in electronic conductivity, due to a semiconductor-insulator transition. $LiMnO_2$ suffers from phase instability upon delithiation and $LiNiO_2$ from oxygen evolution which poses safety hazards. More recent variants have employed mixtures of transition metals, and currently commercialized variants include $LiNiCoAl_{0.05}O_2$ (NCA) and $LiNiMnCoO_2$ (NMC), exhibiting a balance of cyclability, increased voltage, and acceptable capacity. Shortly after the discovery of $LiCoO_2$'s delithiation behavior, Sony developed the first commercially viable secondary lithium ion battery with the incorporation of the graphitic anode, allowing the incorporation of lithium with 1-300 mV reduction in cell potential relative to the Li metal anode. It is important to note that the graphitic anode exhibits a low volumetric capacity, prompting intense research into the use of the Li metal anodes.

1.3 Beyond lithium ion batteries

The desired next generation LIBs will exhibit increased the energy density, operate at increased voltages, offer faster charging rates, all while maximizing capacity retention, all while performing safely. The current state of lithium ion batteries is dominated by stoichiometric $LiMO_2$ layered oxides, liquid carbonate electrolytes, and graphite anodes. Each of these components exhibits some fundamental constraints, limiting the overall capacity and rate capability of lithium ion batteries. Efforts to mechanistically explore these factors will be outlined in the sections below.

1.3.1 Anionic-redox active cathodes

The positive electrode, most commonly $LiMO_2$ layered oxides (where M is a transition metal), having been demonstrated as commercially viable, is still lacking in the accessible capacity. Interestingly, experiments exploring increased Li:M ratios have uniquely shown a first charge capacity far in excess of that theoretically attained through transition metal redox coupled to lithium extraction.[4] Li doping in the M layer is shown schematically in Figure 1.3.
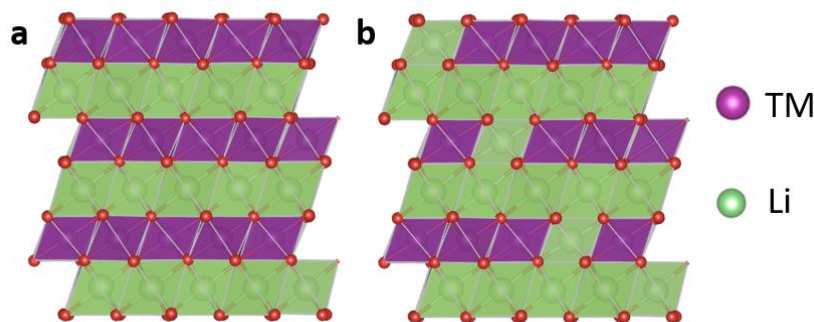
Figure 1.3. (a) Conventional $LiMO_2$ cathode and (b) a lithium-rich variant.

Lithium-rich layered oxide cathodes provoked interest for nearly two decades, as they exhibit notably large capacity on first-charge, as shown in Figure 1.4. After which, notable capacity fade is observed, as well as the loss of the characteristic high voltage plateau.[5] This plateau has been attributed to many effects, including irreversible oxygen evolution, phase separation, surface reconstruction, increased stacking fault density,[6] and transition metal migration.[7] The effects appear to be material system dependent, and are remarkably difficult to pinpoint. Though despite countless manuscripts focusing on degradation mechanisms, they have yet to be implemented commercially, due to notable capacity and voltage fade, among other issues.[8] Nevertheless, the material class continues to amaze, having demonstrated unique defect evolution behavior[6] and most importantly reversible oxygen redox.[9] Great progress has been made to understand the nature of this reversible anionic redox, including computational work drawing

attention to the importance of the Li-O-Li bond, producing labile states and promoting weakly bound electrons available for participation in redox.[10]
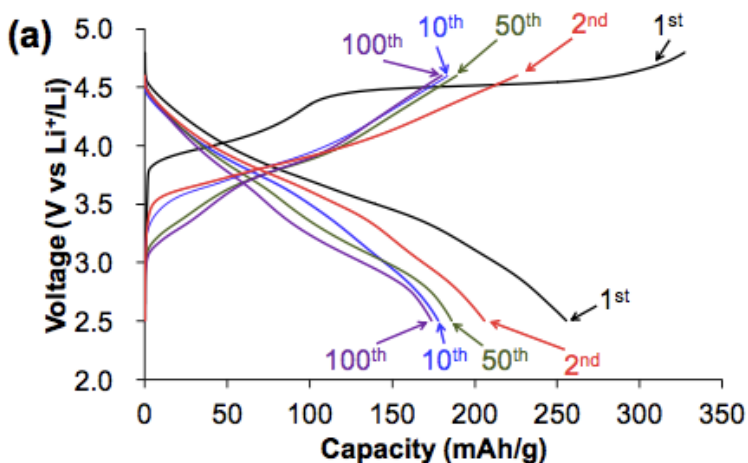
Figure 1.4. Cycling data for a lithium-rich compound, $Li_{1.2}Mn_{0.54}Co_{0.13}Ni_{0.13}O_2$.[5]

Attempts to improve cyclability of these materials include exploration of morphology,[11] surface treatments,[12] surface coatings,[13] and compositional exploration,[14] among others. The extensive amount of literature generally shows minimal improvement without clear differentiation of the mechanisms promoting the improved cyclability. Indeed, solutions to this rapid capacity fade strongly depend on the mechanisms of degradation, and deconvolution of performance enhancement. Work in this thesis focuses on cationic substitution, applying density functional theory to screen dopants modifications to the oxygen vacancy formation energy, which are then used in experimental doping.

1.3.2 Solid-state batteries

Liquid carbonate electrolytes have been crucial in the implementation of high energy density lithium ion batteries present in modern handheld devices and electric automobiles alike. These generally consist of a lithium salt dissolved in mixtures of organic solvents, such as LiFSI

in ethylene carbonate (EC):diethylene carbonate (DEC), and conductivity of lithium ions in these solutions is on the order of 10^{-3} S/cm. However, organic electrolytes suffer from a few issues such as a poor low-temperature performance, high flammability, and the formation of complex solid-electrolyte interfaces (SEIs). Solid state electrolytes (SSEs) provide solutions for many of these shortcomings, the most common of which are oxide, sulfide, and polymer varieties. Over the past decade, high ionic conductivity SSEs have been developed with ionic conductivities exceeding that of their liquid counterparts (Figure 1.5), and even far in excess, as in the case of $Li_{10}GeP_2Si_{12}$, in excess of 10 mS cm^{-1},[15] and even in sodium analogues such as Cl-doped Na_3PS_4, exhibiting room temperature ionic conductivity exceeding 1 S/cm.[16] Solid electrolytes are also considered for their mechanical rigidity, thought to be a key to preventing lithium dendrite propagation—a critical factor for safe lithium ion battery operation.
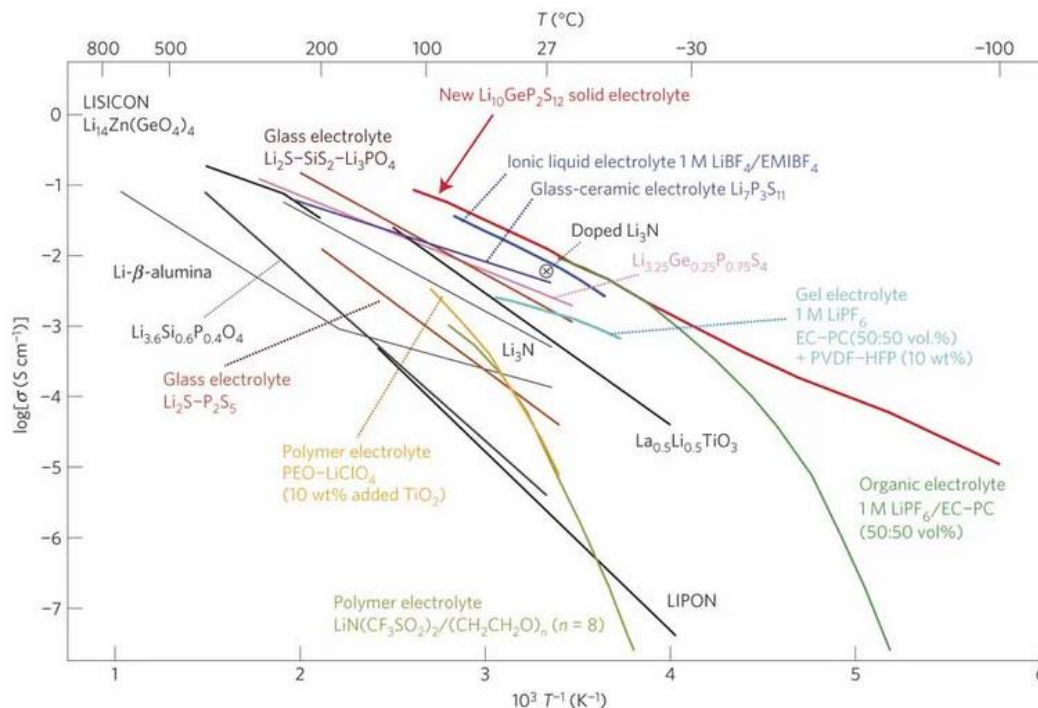
Figure 1.5. Arrhenius plot of solid-state lithium conductors.[15]

However, high ionic conductivity is only one of many factors toward enabling solid state batteries. Interfacial compatibility has been more of a hindrance, as the physical contact between two solids will potentially create phase instability—particularly when elevated temperature processing is required for bonding, as in oxide-oxide interfaces. Indeed, interfacial instability was predicted through a wide density functional theory screening, where grand canonical phase diagrams were calculated to determine voltage stability windows.[17,18] Materials originally considered chemically stable against Li metal, such as lithium phosphorus oxynitride (LiPON) were suggested to electrochemically decompose (Figure 1.6), which was also confirmed via in situ XPS of Li metal deposited on LiPON.[19]
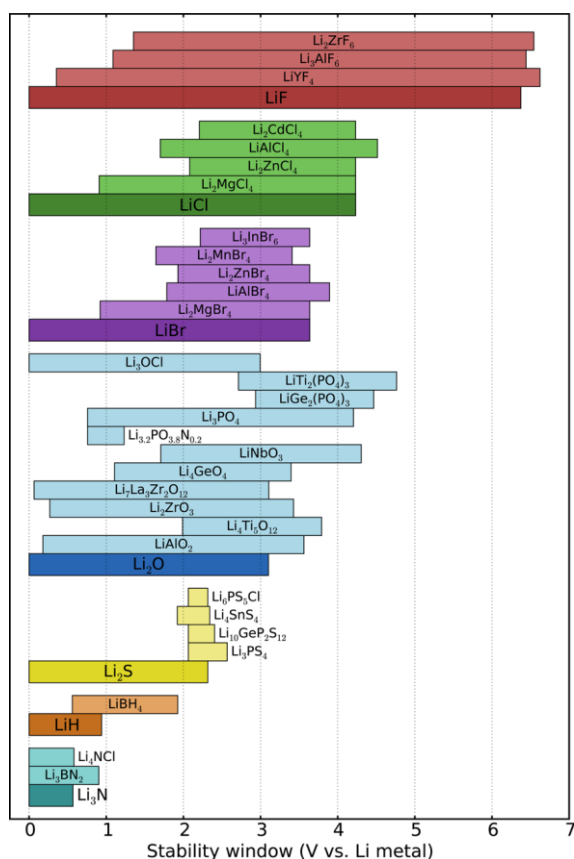
Figure 1.6. Computationally predicted electrochemical stability windows for a variety of lithium ion conductors.[18]

Despite this decomposition, stable cycling may occur, given the decomposition products are both ionically conducting and electrically insulating, as in the case of the Li/LiPON interface. However, other couples which are chemically stable, such as the case of the interface between lithium lanthanum zirconium oxide (LLZO)/Li still exhibit dendrite penetration,[20] drawing more attention to LiPON for its unique cyclability.[21] Work presented in this thesis will combine nuclear magnetic resonance (NMR) with computational spectroscopy to take a structural look of LiPON, observing its glassy nature as a potential source of this stability. We further develop in situ methodologies for characterizing these interfaces in situ.

1.3.3 Lithium metal anodes

Energy storage roadmaps continue to purport lithium metal as the next-generation anode of choice for lithium ion batteries, though their implementation has been postponed for decades with issues of poor coulombic efficiency and potential safety concerns from lithium dendrite propagation.[22] This is due to a variety of effects, including the formation of inactive Li, mass transport variability and electric field nonuniformity, summarized in Figure 1.7.[23] Recently, using a novel gas chromatography setup, the primary source of reduced coulombic efficiency was quantifiably attributed to the formation of electrochemically inactive Li.[24]
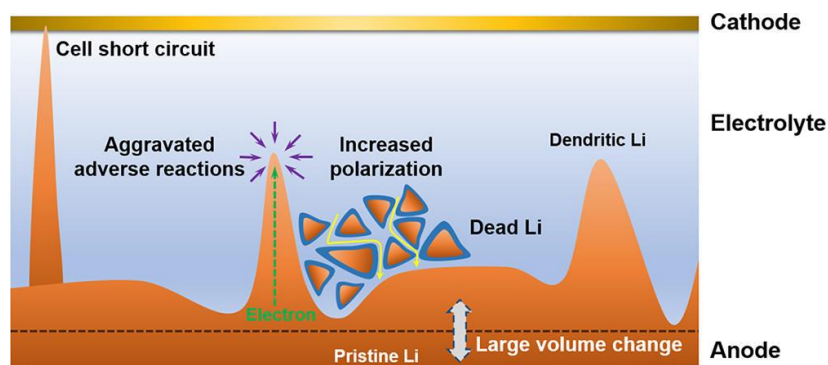
Figure 1.7. Schematic of issues with Li metal anodes resulting in catastrophic failure or poor coulombic efficiency.

Solid-state electrolytes (SSE's) are considered less susceptible to physical dendrite propagation, though issues of lithium metal formation and penetration persist.[25] Further into the future, anode-free cells are looked to for their potential to further increase the energy density of lithium ion batteries, though such cells suffer from pressure effects from an effectively infinite volume change.[22,26] Such issues drive research on lithium metal and dendrite growth studies; while nucleation behavior has been captured in liquid media, a first principles view of lithium nucleation and propagation is lacking. Current views of dendrite growth are largely influenced by the physical presence of liquid electrolytes, forming the solid-electrolyte interface (SEI). While SSE's may serve as physical barriers (questionably at grain boundaries[27]), they still suffering from chemical/electrochemical compatibility issues.[28] As such, an unambiguous view of lithium nucleation is required for an understanding of nucleation mechanisms.

Lithium plating and nucleation has an exhausting background, though most dynamic views of lithium plating and dendrite nucleation stem from the liquid phase. Countless reviews identify the various forms of plating and growth and have been observed to nucleate and grow in multiple stages. The seminal review by Cheng et al.[23] summarizes dendritic growth in 4 stages: (1) spherical Li nucleation; (2) dendrites grow from root and push the formed Li away from the electrode; (3) growth rate decreases due to newly formed SEI; and (4) kinks form on Li whiskers. Of these points, we may simplify our model through (a) removal of the liquid electrolyte's SEI and (b) the removal of lithium concentration surrounding the dendrite itself—the only source of Li is through the solid-electrolyte and the plated Li metal base. This will further mean that kinking will likely be removed as a potential side effect, as Li growth is purely base-driven. As such, future efforts should be focused on isolating lithium nucleation events and simplified growth.

Numerous models for nucleation and propagation of Li dendrites in liquid electrolytes exist; Akolkar [29] has provided a simplified view of the noteworthy work of Monroe and Newman,[30] emphasizing the importance for non-steady-state transport at surfaces and an electrochemical reaction model to couple activation concentration and surface potential. In comparison with the existing lithium dendrite nucleation and growth models, the most critical factors to include in the models will be the modified surface overpotential.[29] In the liquid electrolyte systems, the overpotential is the sum of the activation overpotential and concentration overpotential, and overpotential due to surface energy of the curved dendrite tip. This is typically inversely proportional to the tip radius.

Interestingly, little literature exists focusing on lithium nucleation against solid electrolytes, though recent work by Sagane observes Li plating and stripping at the LiPON/Cu interface.[31] However, here the observed lithium dendrite growth occurs through the Cu, not providing an adequate view of the initial stages of lithium nucleation. Nevertheless, they conclude that the nucleation reactions are the rate-determining step during the plating process and provide further motivation to describe the fundamental nature of Li plating.

Chapter 2. Methodologies

2.1 Physical vapor deposition

Physical vapor deposition (PVD) is a form of materials synthesis where atomic and molecular units are deposited onto a substrate using a variety of methods. Given the controlled nature of deposition and shaping of the energy landscape of a material, a variety of phases may be produced using the same starting material, with the ability to control the deposition rate and temperature. Deposition temperature both aids the surface mobility of sputtered atoms and also provides energy for crystallization. Most techniques create the unique ability to produce metastable and non-equilibrium structures, otherwise unobtainable through conventional processing. Three techniques used for the fabrication of thin film batteries in this thesis are sputtering, pulsed laser deposition, and thermal evaporation.

Based on the deposition type, different growth modes are achievable, shown in Figure 2.1. Depending on the wettability of deposited atoms (adatoms) relative to the substrate, the mobility of the adatoms on the surface of the substrate, and the rate of deposition, island, layer, and Stranski-Krastanov modes are accessible. Step-flow growth (not shown) is also observed in specific orientations of single-crystal substrates. Island growth occurs when adatoms experience low mobility and poor wettability on the substrate, promoting polycrystalline growth. Highly wettable, mobile adatoms may form in layer-by-layer growth, commonly used to produce single crystal, epitaxial films. Intermediate growth modes may occur, such as Stranski-Krastanov growth, where the preferred growth mode rapidly evolves in a convolution of layer and island modes. One final consideration, low temperature deposition may produce films of amorphous nature, as in the case of LiPON, by limiting the surface mobility of adatoms.[32]
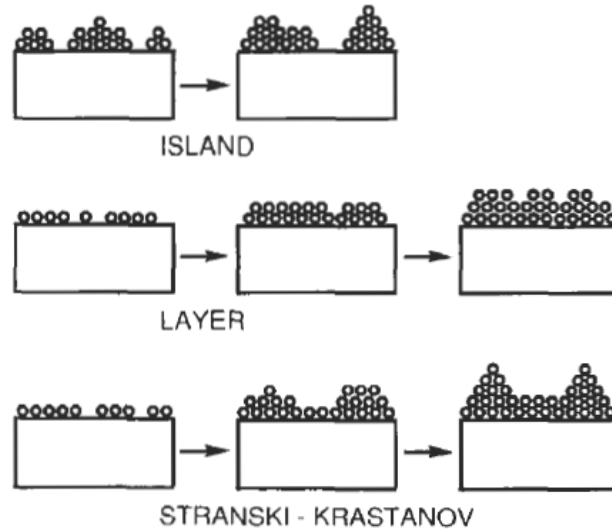
Figure 2.1. Crystalline growth modes in PVD.[32]

2.1.1 Sputtering

Sputtering is a PVD method that utilizes a high electric field to ionize gas, producing a glow discharge plasma. Ionized gas atoms are accelerated in the field toward a charged target material, causing target material to be physically ablated. This ablated material is then deposited onto a substrate, which may be biased and/or heated as required on a system-by-system basis. Direct current (DC) sputtering is often used in metals, where charge accumulation on the metallic target surface does not occur. However, in the case of ceramic targets, radio frequency (RF) sputtering is employed to prevent such charge build up. Sputtering configurations are shown in

Figure 2.2 2.2. To increase the sputtering rate, magnetron sputtering is common, where a static magnetic field is applied to the target, confining electrons to a magnetic field, and enhancing the plasma content at the target surface. This PVD method also maintains target stoichiometry, though some loss of anions is expected, and is compensated by incorporation of a process gas.
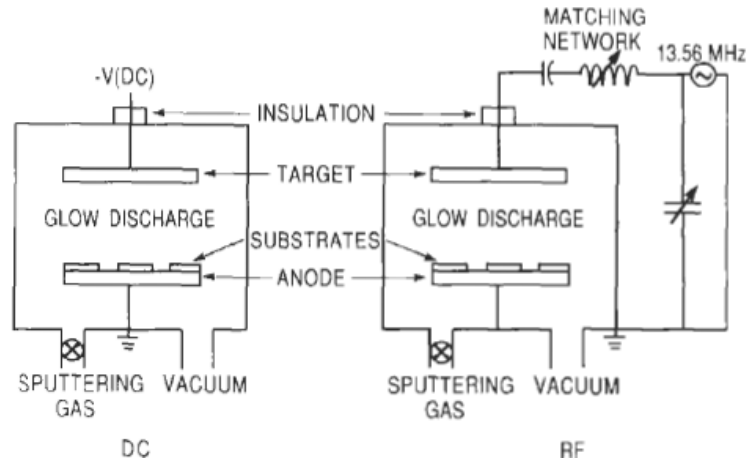
Figure 2.2. Schematics of DC and RF plasma sputtering systems.[32]

2.1.2 Pulsed laser deposition

Pulsed laser deposition (PLD) uses a high energy laser pulse to physically ablate material from a target, generally providing higher degrees of control than sputtering through the manipulation of pulse rate. PLD provides a route to produce thin films with remarkable control of the deposited structure. Importantly, the deposited material generally maintains the stoichiometry of the target material, with the potential for loss of anions which is accounted for by careful control of deposition gas pressure. The PLD process is shown schematically in Figure 2.3. A laser is fired at a fixed position on a rotating target, making sure to prevent laser ablation of the same place on the target. Control of the deposition conditions, including the deposition pressure, pulse rate, and substrate temperature, provide the ability to produce thin films of near-atomic smoothness, easily confirmed by scanning probe methodologies such as atomic force microscopy (AFM). Ultraviolet lasers are typically used for ablation of ceramic targets due to their absorption properties. As such, PLD is not generally performed for metal thin film generation.
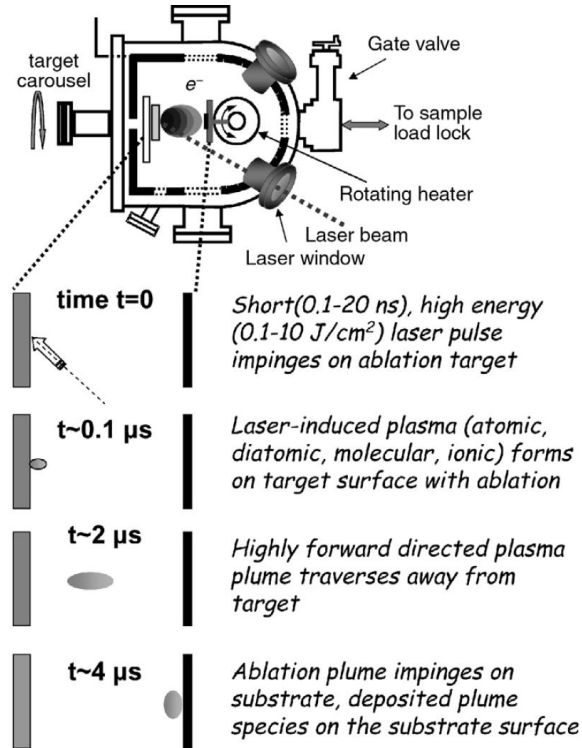
Figure 2.3. Schematic of the PLD process.[33]

2.1.3 Thermal evaporation

Thermal evaporation takes advantage of the reduced evaporation temperature at low pressures. One advantage of thermal evaporation includes low kinetic energy of evaporated atoms, minimizing damage and implantation of the substrate or material. However, the thermalization of atoms is element specific and as such is a non-stoichiometric process, dependent on the vapor pressure of individual elements, as shown in Figure 2.4. Nevertheless, thermal evaporation remains the most effective method of producing uniform interfaces of lithium metal, ensuring conformal coatings of solid electrolytes and generally improved cyclability. Thermal evaporation is performed by through resistive heating of a boat of a material non-reactive with the material to be evaporated. A low base pressure is required for the evaporation of lithium metal, to minimize oxygen content.[32]
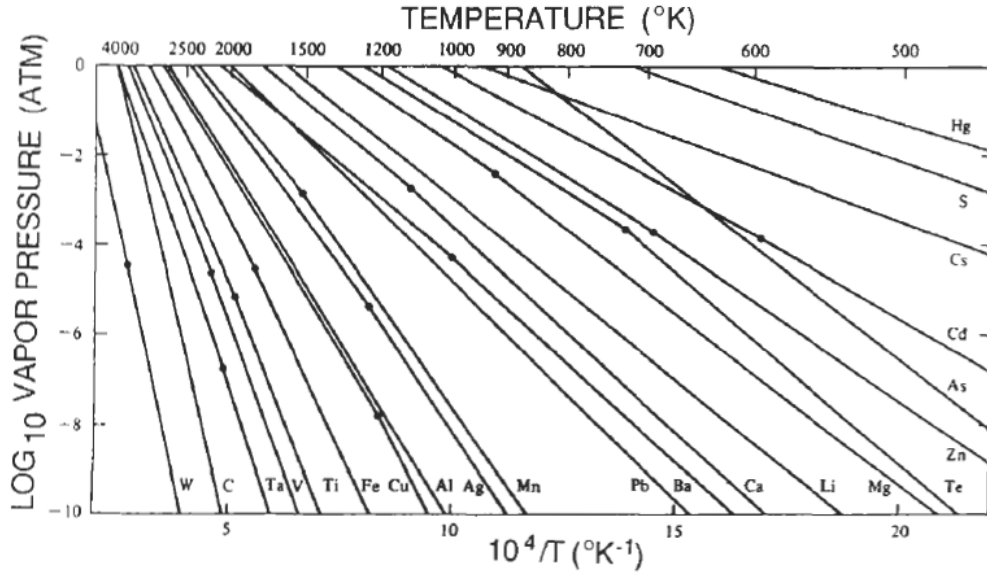
Figure 2.4. Vapor pressure as a function of temperature for selected elements.[32]

2.2 Density functional theory

Density functional theory (DFT) refers to methodologies for calculating approximate solutions of the Schrödinger equation:

$$\left[\frac{h^2}{2m} \sum_{i\,1}^{N} \nabla_i^2 + \sum_{i\,1}^{N} V(\boldsymbol{r}_i) + \sum_{i\,1}^{N} \sum_{j<i} U(\boldsymbol{r}_i, \boldsymbol{r}_j) \right] \Psi = E\Psi$$

most commonly the nonrelativistic, time-independent Schrödinger equation (consisting of an electron kinetic energy term, nuclear-electron interaction term, and electron-electron repulsion term), where the ground state energy is a unique functional of the electron density. Based on the work of Kohn and Hohenberg, the electron density that minimizes the energy of the overall functional is the true electron density, corresponding to a full solution of the Schrödinger equation.[34] The situation is further simplified due to the Born-Oppenheimer approximation, which states that since the mass of the nucleus is approximately 1800 times larger than that of an electron, the nuclei may be approximated to be in static positions.[35] Theoretically, solutions of the

16

Schrödinger equation permit the determination of electron densities, n(r), which are intimately linked to nature of molecular bonding:

$$n(r) = 2 \sum_i \Psi_i^*(r) \, \Psi_i \, (r)$$

Direct solutions of the Schrödinger equation of a crystalline solid are computationally impossible, being a many body problem with a high number of electrons. However, the Kohn-Hohenberg theorem permits treatment of a many body problem with interacting electrons in a static potential to be reduced to a problem of noninteracting electrons in an effective potential.[34] This is reflected in the Kohn-Sham equation[36]:

$$\left[\frac{h^2}{2m} \nabla_i^2 + V(\boldsymbol{r}) + V_H(\boldsymbol{r}) + V_{XC}(\boldsymbol{r}) \right] \Psi = E_i \Psi_i(\boldsymbol{r})$$

Where V_H is the Hartree potential [37]:

$$V_H(\boldsymbol{r}) = e^2 \int \frac{n(\boldsymbol{r}')}{|\boldsymbol{r} \ \boldsymbol{r}'|} d^3 r'$$

And V_{XC} is the exchange correlation, which corrects for electron self-interaction associated with the Hartree potential and takes a variety of forms. To account for this, the local-density approximation (LDA) was employed, applying a static potential.[36] However, the LDA is notably inaccurate in the case of systems with localized electronic occupations, prompting the development of a gradient generalized approximation (GGA), which applies a nonuniform potential.[38] To further correct self-interaction error associated with electro-electron interactions in highly correlated systems, empirical, element-specific Hubbard corrections (GGA+U) have been applied to address inaccuracies.

Solid-state crystalline solids have the added benefit of being periodic structures, which lend themselves to plane wave solutions. Indeed most periodic codes use plane wave methods in their

calculations. Within the implementation of plane wave methodologies, high energies may be removed from the calculations, by limiting the energy, or wavelength of plane waves. This is even more efficiently performed with the implementation of pseudopotentials, which approximate core electrons with a diffuse electron density; this serves two purposes: (1) to remove the total number of electrons in a calculation and (2) to reduce the cutoff energy, as core electrons generally require higher energy plane waves.[39]

2.3 X-ray diffraction

X-ray diffraction (XRD) is a technique permitting the determination of crystal structure and many parameters related to the crystallinity and morphology of a crystal. In laboratory XRDs, x-rays are generated by the injection of thermal electrons, generally from a tungsten electrode. These electrons are accelerated to a target of a variety of target materials, most commonly copper. Cu-Kα excitation is the most common wavelength used in laboratory XRDs which is an average of Cu-Kα_1 ($\lambda = 1.54056$ Å) and Cu-Kα_2 ($\lambda = 1.54443$ Å). Cu-Kβ X-rays are also produced but are generally removed through application of a diffraction-based monochromator or a thin layer of metal with an absorption edge between that of Cu-Kα and Cu-Kβ (a Ni filter is used for Cu sources).

Signal from XRD depends on the coherent diffraction of these x-rays through one or many crystallographic planes in a crystal. To diffract coherently, a Bragg condition must be met, as defined described by Bragg's law:

$$n \lambda = 2d_{hkl}Sin(\Theta_{hlk})$$

where n is a whole number describing the number of planes between which the calculation is performed for, λ is the XRD source wavelength, d is the lattice spacing between the planes in question, and theta is the Bragg angle. This is shown schematically in Figure 2.5.
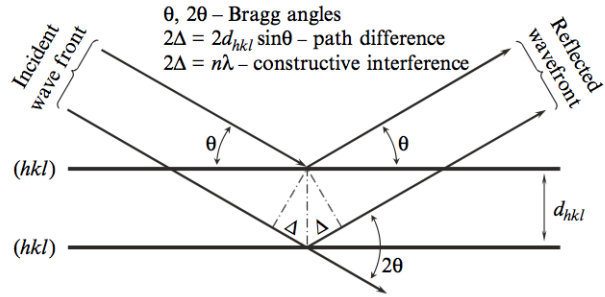
Figure 2.5. Schematic of the Bragg condition for coherent diffraction.[40]

Specific techniques used in this work primarily includes typical theta two-theta (TTH) and grazing incidence x-ray diffraction (GIXRD) modes. TTH scans fix a sample while increasing the angle of the source and detector simultaneously. However, performing a TTH scan on a thin film sample will produce a high signal from the substrate itself. To reduce the impact of the substrate, GIXRD is performed, where the incident beam is fixed at a low angle, generally between 0.5 and 2 degrees.[40]

2.4 Electron microscopy

The electron microscope has proven to be one of the most versatile tools in materials science, providing the potential to extract morphological, structural, and chemical information simultaneously. Before the electron microscope, the optical limit was approximately 300 nm, described by the Rayleigh criterion for visible light microscopy:

$$\delta = \frac{0.61\lambda}{\mu \, sin\beta}$$

Here, the smallest resolvable distance, δ, is determined by the wavelength λ, refractive index μ, and the semi-angle of collection β. Following the development of the theory of the wave-like

nature of electrons by de Broglie in 1925, electrons were explored as methods of surpassing the resolution limits of the optical light microscope. Based on the energy of electrons (E, in eV), their wavelength can be increased according to the relation $\lambda = 1.22\ E^{-1/2}$, so an electron with an energy of 200keV would achieve a wavelength of 2.7 pm. Shortly after, the first scanning electron micrograph was demonstrated experimentally in 1932, and it took only 4 more years to develop the first TEM. However, it wasn't until many years later when sample preparation techniques were developed to thin materials to electron transparency that the first atomic resolution images were acquired. Since this first implementation, both scanning electron microscopy (SEM) and transmission electron microscopy (TEM) have become ubiquitous in materials characterization.[41]
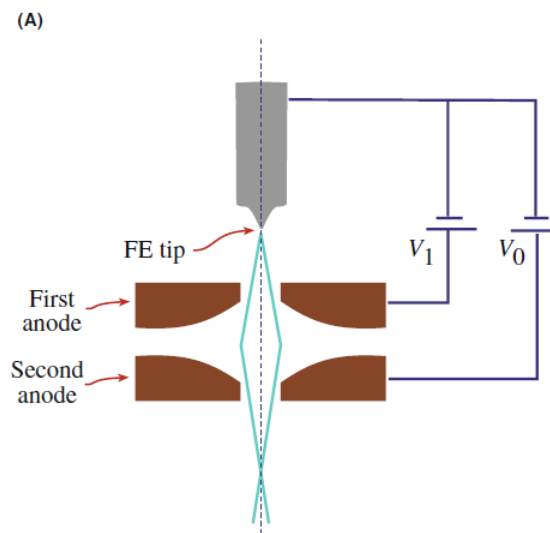
Figure 2.6. Schematic of a field emission gun with a first anode for electron extraction and a second anode to accelerate electrons.[41]

2.5.1 Scanning electron microscopy

Production of an electron beam is commonly achieved through the extraction of electrons in ultra high vacuum by application of an extraction voltage to a tungsten field emission gun (Figure 2.6). The tungsten tip forms a sharp tip to reduce the work function for electron extraction. A potential is applied by an extraction anode, which removes electrons from the gun electrons

which are then accelerated by a second anode and then through a series of electromagnetic lenses and apertures. The energy of the electrons is controlled by the acceleration voltage, which will impact the interaction between the electron and the solid. These are then directed through a series of scanning lenses to raster a focused electron beam across the surface of a sample. The interaction of the electron beam with a material produces a wide range of distinctly different signals, as shown in Figure 2.7. First, a large amount of low energy secondary electrons is generated through secondary scattering events with the incident electron beam. Detection of these low energy electrons is generally collected by an Everhart-Thornley detector (ETD), which applies a voltage to a cage, accelerating these low energy secondary electrons toward the detector. The electrons are then detected by a photomultiplier tube and measured as a signal intensity. As the electron beam is rastered across the sample, an image is produced based on the spatial location of the probe and the intensity of the electrons being generated. An ETD is typically placed at a wide angle from the sample, producing topographical contrast.
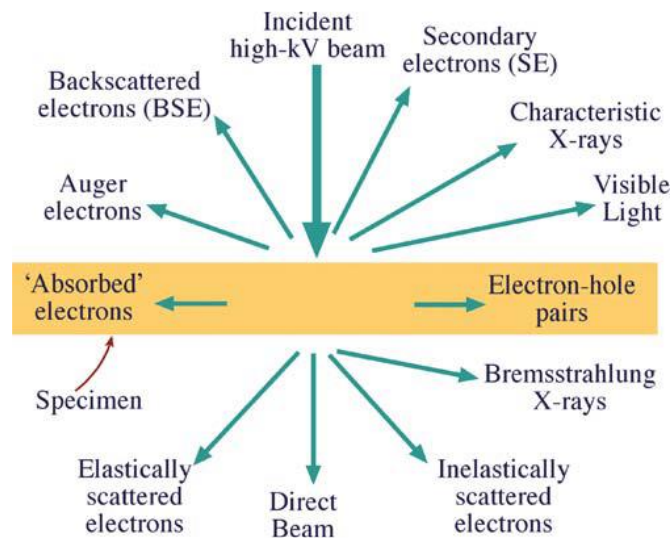
Figure 2.7. Signals produced when a high voltage incident electron makes contact with a piece of material.[41]

Backscattered electrons are another common signal produced. These result in interactions of the incident beam with nuclei and signal is characteristic of atomic mass, providing phase contrast information. X-rays are also emitted, and X- are collected in a technique called X-ray energy dispersive spectroscopy (EDS). EDS is based on the emission of element-specific X-rays, emitted from the decay of a higher energy electron to an electron hole generated by the electron beam. Figure 2.8 shows the process by which characteristic x-rays are generated, here a Kα transition. As energy levels are discretized, these characteristic wavelengths are well defined, and may easily be used to quantitatively determine the composition of the elemental sources of the radiation within 1%. However, the technique is generally limited to elements on the periodic table above C. This limitation is primarily a hardware issue, where absorption of the x-rays through a protective window reduces the low signal generated from the light elements, though modern windowless detectors offer the potential to quantify elements as low as Li.[41]
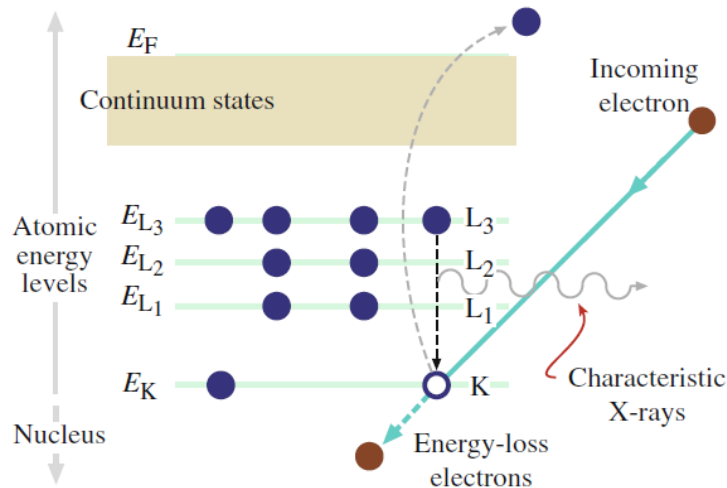
Figure 2.8. Process for generation of characteristic x-rays by an incident electron.[41]

2.5.1 Transmission electron microscopy

Transmission electron microscopy (TEM) utilizes a similar beam to that of the scanning electron microscope, though electrons are accelerated at much higher voltages so that they may be

transmitted through thin samples of material, and a parallel beam is desired when passing through

the sample. Sample preparation is crucial for quality TEM microscopy, requiring samples on the

order of 100 nm thick. TEM imaging is based on the electron diffraction, and schematic of the

pathways of diffracted electrons are shown in Figure 2.9.[41]
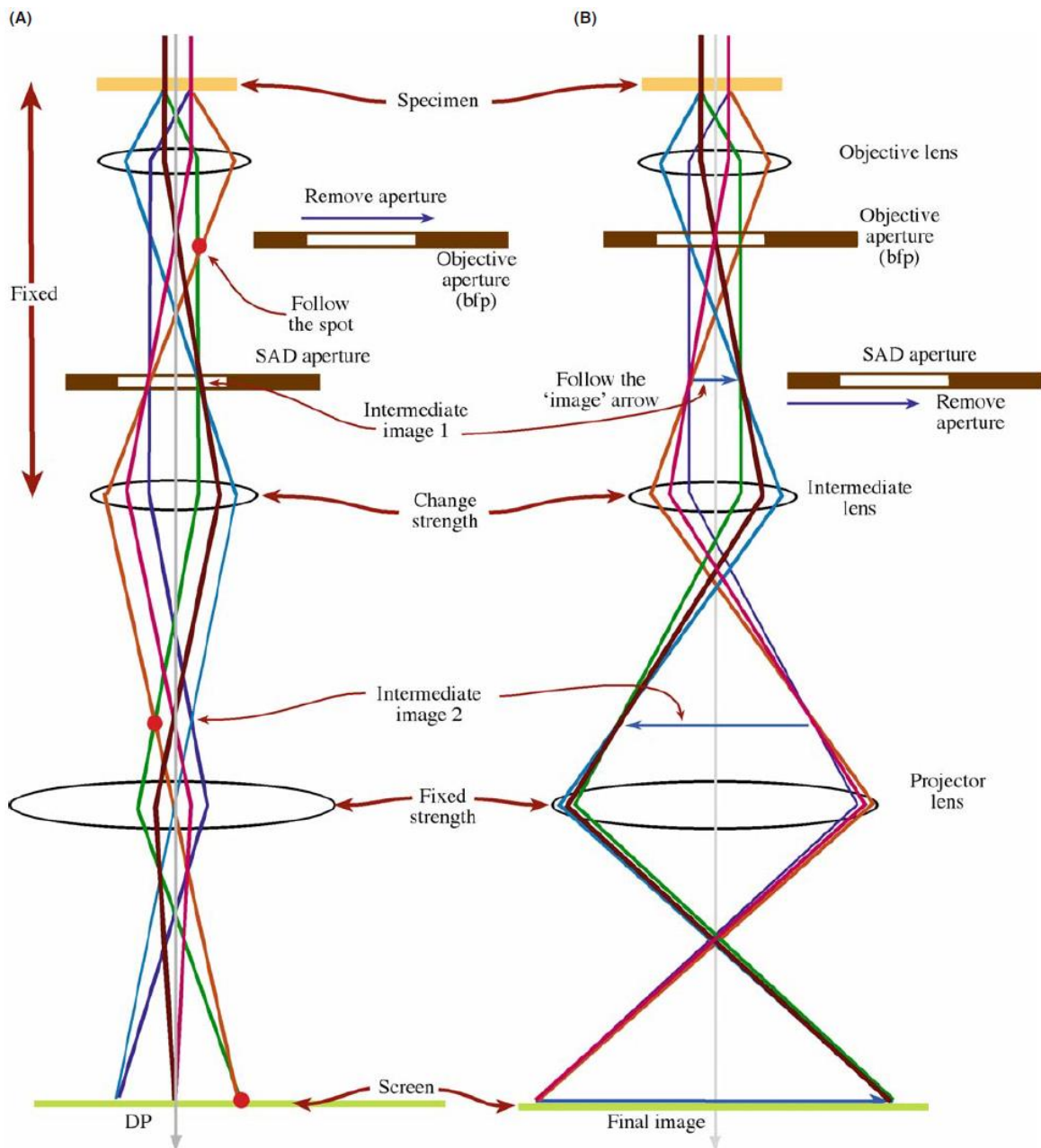
Figure 2.9. The path of the electron beam is adjusted by lens strength based on the desired imaging mode: (a) diffraction mode or (b) imaging mode.[41]

Alternately, the TEM may be operated in a similar fashion to a SEM, rastering a fine, high

energy probe across the sample, called scanning transmission electron microscopy (STEM). STEM

resolution is dictated by the size and alignment of the probe, with a much higher resolution than

SEM due to both the increased electron energy and the reduced interaction volume due to the small

sample thickness. STEM may also be used for chemical mapping using EDS, as mentioned

previously, and energy loss dispersive spectroscopy (EELS), a high-resolution chemical

spectroscopy method which may be used to probe a variety of phenomena from basic

quantification to plasmonic behavior. Imaging signals may be determined through the directly

transmitted beam, known as bright field (BF) imaging, or by annular dark field (ADF) detection,

which is measured at a higher scattering angle (Figure 2.10). ADF contrast is based on Z-contrast

due to Rutherford-scattering effects, and may be more sensitive to lighter elements. BF imaging is

complementary to ADF, though contrast is generally inverted, but lacks the sensitivity for lower

Z elements.[41]
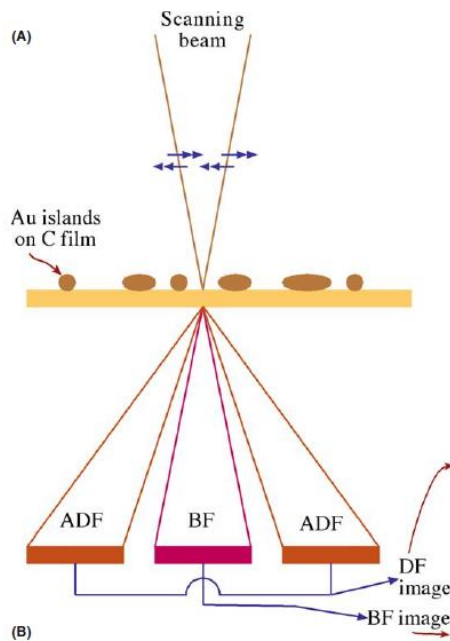
Figure 2.10. Scanning transmission electron microscopy detection by bright field and annular dark field modes. [41]

2.5 Focused ion beam

Focused ion beams (FIBs) operate on similar principles of electron microscopes, but rather than using electrons as a probe, large ions are manipulated. The FIB has proven a remarkably effective tool for TEM preparation, capable of producing thin lamella of regions pre-determined by SEM and its related spectroscopies. FIB may also be used to produce a variety of nano and microstructures, for further means of advanced characterization, as demonstrated in the field of nanomechanics.[42] Ga^+ is the most common ion used in the FIB, due to its melting point near room temperature (29.8°C) and low vapor pressure. Once the Ga is molten, application of a field produces a Ga source in the shape of a Taylor cone, balancing electrostatic force and surface tension. This is similar to that used in tungsten field emission guns, and are similarly accelerated and rastered as in a SEM. However, the high mass of the Ga+ creates a cascade of sputtering events, as shown in Figure 2.11. Generally, an atom will be sputtered if the energy of the Ga+ transmitted exceeds that of the surface binding energy. Ga implantation also generates a large number of secondary electrons (approximately equal to the number of ions injected), permitting live imaging of the ion milling process.[43]
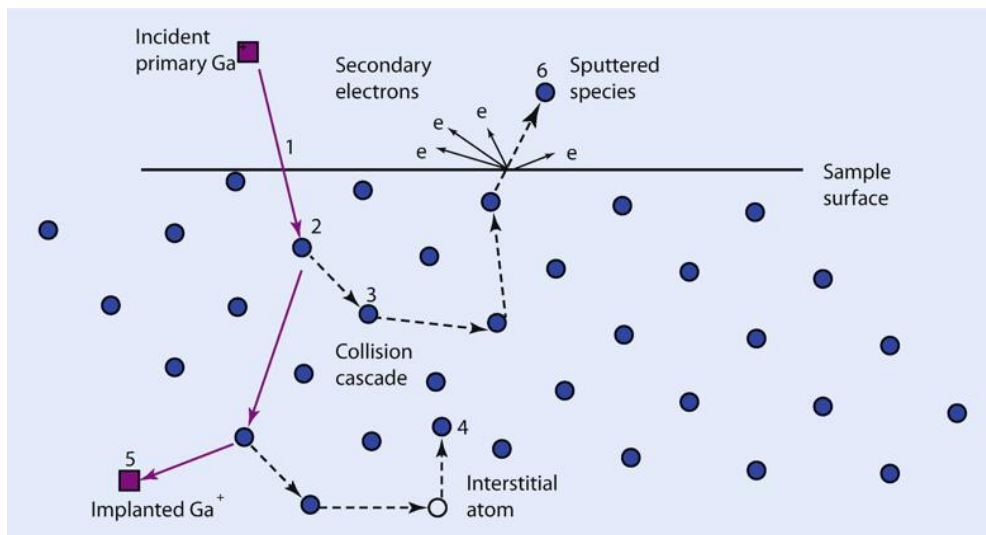
Figure 2.11. Ga ion pathways during focused ion beam operation.[43]

During the milling process, many deleterious effects occur. First, many Ga ions are also be implanted into the sample. This is exaggerated when milling normal to the material surface. Second, sputtered ions will redeposit locally. Both require careful control of the milling process to ensure that the surface you desire to analyze is free of implanted Ga and redeposited material. This is achievable through a series of low energy cleaning steps on the exposed, milled surface. Focused ion beams are also equipped with metallic gas sources which may be deposited by ion and electron beams. A common example is organometallic platinum. When heated under vacuum, the organometallic platinum forms a vapor. These gas molecules must have a sufficiently high probability of sticking to the surface of the region of interested and must decompose when in contact with the electron or ion probe faster than the rate that it is sputtered away.[44] Modern FIBs have employed gas plasmas with larger atomic mass, such as Xe^+, to increase sputtering rates while reducing the effects of implantation.[45]

2.6 Solid State Nuclear Magnetic Resonance

Solid state nuclear magnetic resonance (ssNMR) is one of the few techniques capable of characterizing local bond configurations in disordered solids. This technique places solid samples into a probe which experiences strong magnetic field (on the order of 10 Tesla), causing the nuclear spins of elements (those with nonzero angular momentum) in a sample to precess around the static magnetic field vector at the Larmor frequency. Samples are placed into a rotor at an angle (a so-called magic angle, coining the term magic angle spinning NMR, or MASNMR) to reduce the effects from weak dipolar coupling. This rotor is spun at a high frequency, which similar removes dipolar effects (dominant at low rotation speeds) and may time-average the chemical shielding; at high enough rotation speeds, the chemical shielding may be completely averaged, producing a purely isotropic chemical shift. This nuclear chemical shielding is the result of the electron density

distribution associated with molecular bonding and causes deviations from ideal nuclear precession. Such chemical shifts, δ, is calculated by

$$\delta = \frac{\omega_{sample} - \omega_{reference}}{\omega_{reference}}$$

where ω are the NMR frequencies of the sample and reference, measured in ppm. Radio frequency pulse sequences are applied to a solenoid surrounding the spinning rotor, creating a time-dependent oscillation of the external magnetic field, resulting in an off-axis precession of the spin. The relaxation of this precessing nucleus (Block decay) is then measured by the same solenoid used to produce the pulse. Pulse sequence application is a complex field and are highly materials and process dependent. A wide range of phenomena can be explored through the application of complex pulse sequences, the application of secondary pulse sources may be applied to perform cross-polarization measurements, and many more, beyond the scope of this background.[46]

Chapter 3. Lithium-rich layered oxide cathodes

3.1 Background for anionic-redox-active cathodes

Lithium ion battery technology has enabled the advancement of handheld devices and electric vehicles, and has reached to grid-scale storage markets. To further these technologies, improving battery life and extending electric vehicle ranges, the energy density of LIB cathodes must increase well beyond the current reach of commercially available cathodes.[47,48] Lithium rich layered oxide cathodes have sparked intense interest due to their strikingly high capacities, in excess of 250 mAh/g—well beyond the capacity of current commercial cathodes such as $LiCoO_2$, $LiMn_2O_4$ and $LiFePO_4$ (160, 120, and 168 mAh/g, respectively).[49] This is generally attributed to anionic redox behavior—a phenomenon under intense scrutiny, yet widely accepted as the source of this capacity.[50–52] Unfortunately, the increased capacity is accompanied by a host of issues, including sensitivity to processing method,[8] transition metal (TM) migration,[53] surface phase transformations,[54] and the irreversible release of oxygen.[9,55,56] Further, this oxygen loss subsequently reduces the barrier for transition metal migration.[57] A combination of these effects leads to characteristic voltage decay and capacity fade. Many methods have been employed to combat this rapid degradation, including surface modification[12,58] and coating,[59] morphological control,[11] and incorporation of dopants;[14] each method shows a degree of improvement in one aspect of cycling, yet a comprehensive solution to Li-rich layered oxide cathodes shortcomings is still lacking. Despite the clear role of surface phase evolution in lithium rich layered oxide cathodes, the majority of oxygen activity occurs in the bulk, and doping remains an effective strategy for modifying bulk properties.

Most recent computational advances have described the notion of anionic redox in terms of two general phenomena: reorientation of oxygen ions into peroxo-like oxygen dimers, in the

case of 4d transition metal layered oxides,[50,60] and more relevant to 3d transition metal elements, the alignment of two lithium ions across an oxygen atom creating labile oxygen states, susceptible to redox.[10] With respect to doping in particular, an extensive amount of ab initio calculations and experiments have been performed in Li-rich layered oxide cathodes. Computationally, density functional theory (DFT) studies generally provide insight into structural modification, band structure, voltage, and diffusion behaviour. Though the majority of these studies lack experimental interpretation, and, similarly, if experimental doping studies exist, these experiments lack description in terms of this computational work. A few noteworthy exemptions include the work of Deng et al.,[14] Wang et al.,[61] Xiao et al.,[62] and Gao et al.[63] Deng et al.[14] and Wang et al.[61] performed a range of cationic substitution experiments on lithium-rich NiMn layered oxides for a range of TM stoichiometries; results showed an increased initial charging plateau for the Co substitution and decreased plateau for the Ti substitution, attributed to the degree of overlap between the dopant t_{2g} and O 2p orbitals, correlated to the extent of electron localization.[14] This work was followed up by a computational explanation of the impact of cation substitution on oxygen evolution, attributing increased oxygen loss to an effective decrease in band gap. The band gap is viewed as an impediment to charge transfer, a prerequisite for oxygen evolution.[62] Gao et al.[63] and Kong et al.[64] have performed the most comprehensive computational screening, both applied to Li_2MnO_3, Kong performing a comparative study between the classical layered and Li-rich analogue. Gao et al.[63] calculate oxygen release energies by removing anions with the lowest Bader charge on delithiation, predicting Nb-doping as a stabilizing agent, and Kong et al.[64] shows that typical dopants are thermodynamically stable within the Li-rich layered oxide framework and have the potential to alter electronic conductivity through hole polaron formation. Prior to this work, Gao et al.[65] had also calculated the impact of doping Mo into Li_2MnO_3, predicting a reduced

29

band gap and improved Li mobility between Li and TM layers. Aforementioned doping experiments are generally difficult to describe via computation due to the potential for effects beyond purely bulk doping; as such, low doping amounts are used in this study to aid ease of dopant incorporation and prevent notable surface effects. Other experimental doping includes Ba into Li-rich NiMn layered oxide (LNMLO) cathode, showing improved rate capability[66] and B-doping into Li-rich NiMnCo showing modified crystallization[67] and improved oxygen redox reversibility[68], not calculated in this study due to interstitial incorporation rather than substitution. A multitude of other doping studies generally show that substitution of a small percentage of metal cations significantly alters cathode performance, though most experimental studies generally lack experimental evidence of incorporation and further lack the theoretical framework to understand the role of the dopant in these changes. Moreover, the importance of local environment to the dopant is not addressed in most computational work.

This work uniquely combines ab initio calculations of oxygen stability in LNMLO cathode material with experimental synthesis and characterization based on these findings, focusing on the notion of site-dependent anion stabilization in the lithium rich layered oxides. Analysis of the delithiated structure, subsequent structural changes, and bonding environment changes increase the complexity of the model, more closely resembling the true nature of an experimental material. Using first principles approaches, we show that oxygen vacancy formation is highly dependent on the local bonding environment, which has been shown to vary with the state of charge of the cathode. Using this site-based approach, we relate oxygen stability to the local environment changes during cycling. Findings of formation energies are rationalized using calculated data, showing a strong influence of doping on the charge density distribution, affecting the potential to form of oxygen vacancies. Doping of LNMLO with Al, Ti, Co, and Mo is then performed, clearly

30

impacting the initial charging plateau associated with oxygen redox and loss. Al and Ti doping show little change to the oxygen redox plateau, as predicted by computation of the E_{Ov}^{F} calculations. Co-doping shows the opposite effect, due to increased oxygen loss from the lattice, again as predicted. When co-doped with Co and Mo, reduced oxygen loss, reduced voltage fade and improved capacity retention are observed. Incorporation of the Mo dopant is evident through X-ray diffraction, X-ray photoemission spectroscopy and energy dispersive X-ray spectroscopy. These findings demonstrate that ab initio calculations can be used to rationally select cation dopants to improve oxygen stability within the bulk of lithium rich layered cathode materials, while leaving oxygen available for reversible redox.

3.2 Methodologies

3.2.1 Density Functional Theory

A spin-polarized GGA+U approximation to the Density Functional Theory (DFT) was employed, to account for electron correlations in transition metal and rare earth elements. Projector augmented-wave method (PAW) pseudopotentials were used as implemented in the Vienna Ab initio Simulation Package (VASP). The Perdew-Burke-Ernzerhof exchange correlation and a plane wave representation for the wavefunction with a cut-off energy of 450 eV were used. The Brillouin zone was sampled with a k-points mesh of 5 x 4 x 7 for structural relaxations and oxygen vacancy formation energy calculations and 10 x 8 x 14 for density of states (DOS) calculations, both by Gamma packing. Atomic coordinates and lattice vectors were fully relaxed for each structure. Effective U values used in the calculations are provided in the Supplemental Information, applied with the rotationally invariant approach.[69]

3.2.2 Cathode Synthesis

Pristine $Li[Li_{0.2}Ni_{0.2}Mn_{0.6}]O_2$ (LNMLO), Co-doped $Li[Li_{0.144}Ni_{0.136}Co_{0.136}Mn_{0.544}]O_2$ (LNMLO-Co), and Mo-co-doped $Li[Li_{0.144}Ni_{0.136}Co_{0.136}Mn_{0.544}]_{0.99}Mo_{0.01}O_2$ (LNMLO-CoMo) materials were synthesized by carbonate co-precipitation method (CCP). TM nitrate solutions (Ni:Mn = 1:3, Ni:Co:Mn = 1:1:4, 1M) were titrated into $NaCO_3$ solution (0.2 M) under stirring. The pH value during the co-precipitation process was carefully controlled between 7.80 and 7.85 to avoid hydroxide precursor generation. The slurry was then aged at 80 °C for 12 hours. After washing and drying, the TM carbonate precursor was sufficiently mixed with a stoichiometric amount of Li_2CO_3 and MoO_2. The two-step calcination conditions are 500 °C for 5 hours and 850 °C for 15 hours.

3.2.3 X-ray diffraction

X-ray powder diffraction (XRD) spectra were acquired using a Bruker D8 Advance diffractometer with a Bragg-Brentano θ-2θ geometry and a Cu Kα source (λ = 1.54 Å). Samples were scanned from 10° to 80° at a scan rate of 0.05°/step. Rietveld refinement was performed using FullProf software.

3.2.4 Electron microscopy

High-angle annular dark-field (HAADF) imaging was carried out on a Cs-corrected FEI Titan 300 kV transmission electron microscope (TEM)/scanning transmission electron microscope (STEM). All HAADF images were acquired at 300 kV and with a beam size of ~0.7 Å. To minimize possible electron beam irradiation effects, HAADF images were acquired from areas without pre-beam irradiation. STEM/energy dispersive spectroscopy (EDS) was performed on primary particles using a JEOL JEM-2800 at 200 kV in ADF mode. Scanning electron microscopy

(SEM)/EDS spectra were collected from focused ion beam (FIB) cross-sections of pristine secondary particles. FIB cross-sections were prepared using an FEI Scios™ Dualbeam™ FIB.

3.2.5. X-ray photoelectron spectroscopy

X-ray photoelectron spectroscopy (XPS) was performed using a Kratos AXIS Supra with the Al anode source operated at 15 kV. The chamber pressure was $< 10^{-8}$ Torr during all measurements. High-resolution spectra were calibrated using the hydrocarbon C1s peak at 284.6 eV. Data fitting was performed using CasaXPS software using a Shirley-type background.

3.2.6 Electrochemical Measurement

Cathodes consisting of 80 wt % of active materials, 10 wt % of Super P carbon, and 10 wt % of poly(vinylidene fluoride) (PVDF) binder were assembled into standard 2016 coin cells with Li metal as the anode and 1 M LiPF6 in ethylene carbonate/dimethyl carbonate (EC:DMC in 3:7 weight ratio) as the electrolyte. The electrodes were assembled in a R2016 coin cells, where the active materials are the working electrodes and Li metal serves as the counter electrode. The mass loading is ~ 3 mg/cm2. Electrochemical performance was measured using an Arbin battery cycler in galvanostatic mode between 2.0 – 4.8 V vs. Li/Li+, at a current density of 12.5 mA/g for the first cycle and 25 mA/g for following cycles. The plateau length refers to the capacity above 4.4 V after normalizing the plateau voltage of doped materials to that of pristine materials. Electrochemical impedance spectroscopy (EIS) measurements were carried out using a Solatron 1287 potentiostat, with a 10 mV perturbation and AC frequencies from 0.01 to 1×106 Hz on as assembled electrodes and after 30 cycles. An equivalent circuit model was fit to the data to analyse the reactions that took place using Z view software (v. 3.4a, Scribner Associates, Inc.).

3.3 Results and Discussion

3.3.1 Oxygen Vacancy Formation Energy

A model supercell was used containing 14 Li (2 within the transition metal layer), 3 Ni, 7 Mn and 24 O, corresponding to a stoichiometry of $Li[Li_{2/12}Ni_{3/12}Mn_{7/12}]O_2$. In this manuscript, the fully lithiated state is referred to as "pristine", and the material lacking dopants as "undoped". For doping studies, one dopant ion, M, is substituted for Mn, resulting in a stoichiometry of $Li[Li_{2/12}Ni_{3/12}Mn_{6/12}M_{1/12}]O_2$, referred to as "M-doped". Optimal coordination of atoms within the transition metal layer were determined through structural relaxations, and are consistent with previously published work.[54]
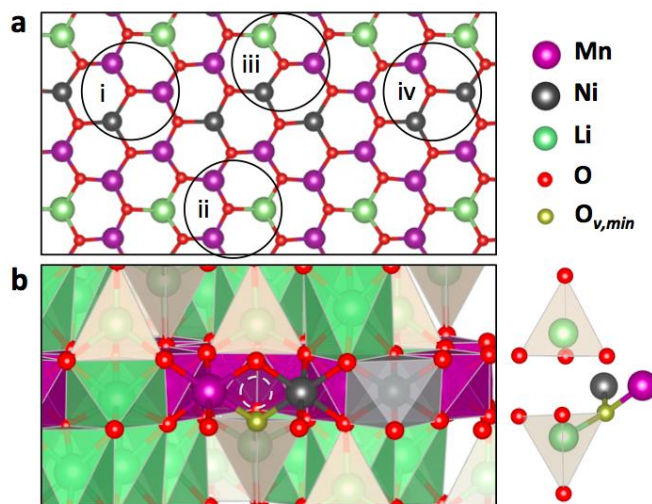
Figure 3.1. (a) The undoped structural model used in this study contains four general TM environments for each oxygen atom: (i) Mn-Mn-Ni, (ii) Mn-Mn-Li, (iii) Mn-Ni-Li, and (iv) Mn-Ni-Ni; (b) Relaxed structure contains a wider range of neighbouring configurations, including the formation of lithium dumbbells, isolated at right, around lithium vacancies within the transition metal layer (dashed circle).

This configuration, shown in Figure 3.1a, creates four local TM environments surrounding oxygen ions, though this number is expanded with the incorporation of dopants and delithiation of the structure. Li-rich materials' initial charging plateau following transition metal redox is attributed to oxygen evolution.[8] As such, the state of delithiation selected for analysis of oxygen

evolution is at a lithium concentration of 8/14, referred to as "delithiated". The relaxed structure on delithiation of the supercell was determined by analyzing energies of all permutations of lithium removal. From this relaxed supercell, each oxygen atom was removed and a final calculation was performed. The oxygen vacancy formation energy, E_{Ov}^F, was calculated by

$$E_{Ov}^F = E\left(Li_{\frac{8}{12}} Ni_{\frac{3}{12}} Mn_{\frac{6}{12}} M_{\frac{1}{12}} O_{2-\frac{y}{12}}\right) + \frac{y}{24} E(O_2) - E\left(Li_{\frac{8}{12}} Ni_{\frac{3}{12}} Mn_{\frac{6}{12}} M_{\frac{1}{12}} O_2\right) - 1.36$$

where the -1.36 eV correction factor is included to account for overbinding of GGA in molecular oxygen calculations. E_{Ov}^F was determined by removal of an oxygen ion from each oxygen site.[70] A similar process was performed for dopant incorporation, first determining the most stable site of the particularly dopant, delithiating, and extracting oxygen, further described in the Supplemental Information. Simulations with and without oxygen vacancies are relaxed and produce charge neutral supercells. Scaling was performed to ensure no spurious interactions between defects.

To briefly discuss current understanding of oxygen redox in Li-rich cathode materials, there are a few theories pertaining to the mechanism leading to oxygen oxidation: most prevalent theories are the formation of a peroxo-like species[50,71] and the formation of electron holes in certain oxygen bonding environments.[9,10] The notion of the peroxo-like formers has been experimentally viewed, but further computational and experimental work suggests that this phenomenon is limited to the case of 4d and 5d transition metal oxides, which may be phenomenologically viewed as having weaker localized bonding with oxygen, and allow more flexible bond angles with the subsequent formation of O-O bonds.[10,71,72] In the case of more traditional, commercially relevant materials consisting of 3d TM elements, TM-O bonds are viewed as more rigid. Both computation and experiment view the formation of peroxo-groups in these materials unlikely, and further evidence supports the presence of localized electron holes.[9,10] A similar rigidity is observed both

in literature[10] and in our model calculations, for TM-O bonds. It is further noted that through the application of GGA+U, similar to the previously demonstrated use of hybrid functionals,[10] an increased partial density of states is observed near the Fermi energy for oxygen ions exhibiting a Li-O-Li bond (Supplemental Information). Despite the advantage of labile oxygen, as reflected in the initial charge capacity of lithium rich layered oxides, these easily oxidized anions also exhibit reduced bonding stability and are subject to removal. As such, calculation of E_{Ov}^F is critical in understanding anion stabilization.

From the calculated E_{Ov}^F results, a wide range of E_{Ov}^F is observed in the undoped, delithiated structure. To understand this E_{Ov}^F variation, it is first necessary to examine the relaxed structure of the undoped material, delithiated to the point where oxygen is experimentally observed to release from the lattice. The broad range of local atomic environments in the relaxed structure is seen to directly impact E_{Ov}^F, and is generally overlooked in simulated oxygen vacancy formation energy calculations. A critical feature of this relaxed structure is the formation of the lithium dumbbell or the migration of lithium ions to tetrahedral sites surrounding a TM-layer lithium vacancy, shown in Figure 3.1b.[54] Explicit representations of oxygen coordination environments with respect to the transition metal layer are provided in the Supplementary Information. A few trends are observed related to the variation in E_{Ov}^F in Figure 3.2. The lowest energy sites contain three critical environmental factors: (1) the presence of a Ni nearest neighbours generally results in a lower oxygen vacancy formation energy, due to reduced electrostatic repulsion between the oxygen vacancy (effectively a positive charge) and the less positive Ni cation;[57] (2) a minimized coordination with cations; and (3) subsequently occurs near a TM layer lithium vacancy and hence is in proximity to a tetrahedral lithium ion. The migration of lithium to the tetrahedral site creates a local environment loosely resembling a trigonal plane with a tetrahedral lithium, Ni ion, and Mn

ion as vertices. Intuitively, this distorted trigonal planar environment does not well suit the orbital symmetry of oxygen ions, and the reduced bonding stability is evident through the reduced E_{Ov}^{F}.
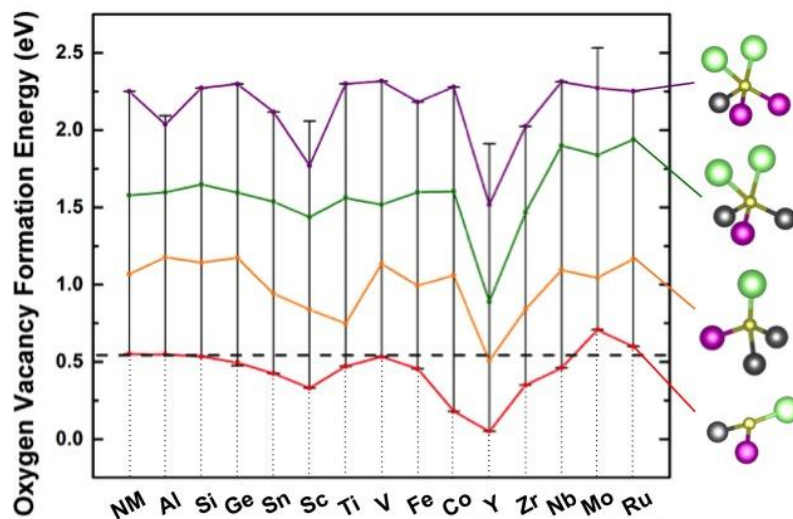
Figure 3.2. Distribution of oxygen vacancy formation energies, E_{Ov}^{F}, for each oxygen site for a full range of dopants. Representative bonding environments are indicated to reflect their relative E_{Ov}^{F}.

3.3.2 Impact of Dopants on Oxygen Stability

Generally, a similar range in E_{Ov}^{F} is present in the doped and delithiated structures, though doping is seen to alter the distribution and magnitude of these energies. Al, Ti, Co and Mo were selected as representative dopants for further analysis, either showing little (Al, Ti) or notable changes (Co, Mo) in E_{Ov}^{F}. Of the simulated dopants, Mo and Ru are predicted to raise the E_{Ov}^{F} of the lowest energy site for oxygen release. Despite Ru having shown an enhanced E_{Ov}^{F}, as well as interesting properties when used in lithium rich layered oxides, showing the formation of peroxo-like species on discharge,[50] the advantages of Ru doping are far outweighed by its cost, and hence will not be further discussed as a dopant in this work. Similar to the undoped scenario, the lowest E_{Ov}^{F} is present at same local environment displaying the near-trigonal planar configuration. Al and Ti are further discussed for analytical comparison due to the calculated E_{Ov}^{F} being similar to that of the undoped material, and are of further interest due to their reduced cost and low toxicity,

respectively. Last, Co was selected due to its predicted decrease in E_{Ov}^F, enhancing oxygen release, and its relevance in commercial cathode use. Co is also unique in that its predicted location is in proximity to the most volatile oxygen site (i.e., lowest E_{Ov}^F), which may further promote instability and oxygen loss.

To rationalize this predicted oxygen vacancy formation energy change, a site-dependent analysis of the delithiated charge density distribution and density of states (DOS) were performed to determine if the dopant affected the electronic behavior of the cathode material. First, a Bader charge analysis was performed to observe trends in electron density with the incorporation of dopants. In previous oxygen vacancy formation studies,[63,65] oxygen sites with the lowest Bader charge and largest Bader charge difference between pristine and delithiated states are supposed to evolve most easily, and these sites are generally used for the E_{Ov}^F calculations. While this is the case for incorporated 3d transition metal dopants, Mo-doping shows a discrepancy between oxygen sites with maximum Bader charge difference and minimum E_{Ov}^F. Mo-doping also shows the highest net increase in charge density associated with oxygen sites. Last, a correlation is observed between average change in Bader charge upon delithiation and average E_{Ov}^F.
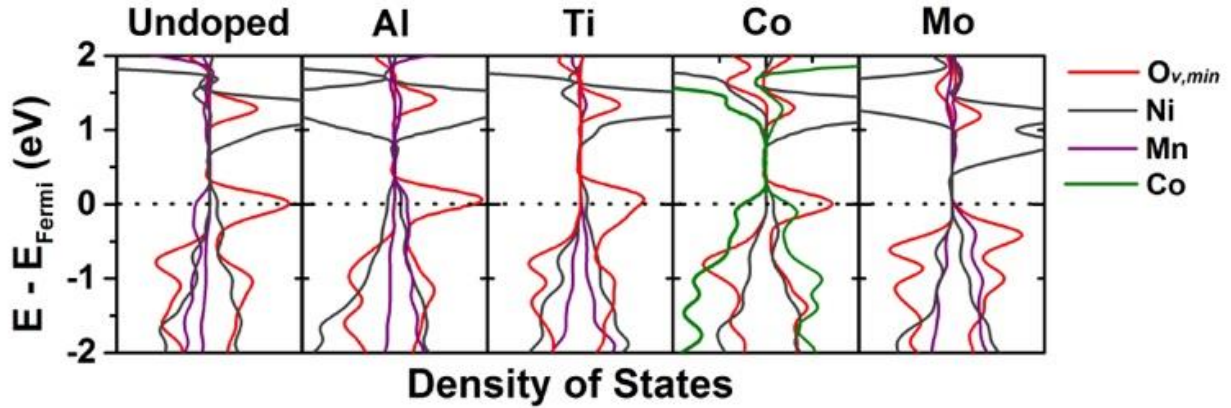
Figure 3.3. The partial density of states for the lowest E_{Ov}^{F} site and neighbouring transition metals prior to oxygen removal. analysis shows that Mo doping shifts the bonding states below the Fermi energy, and increases the electron density below the Fermi energy, a potential source of anion stabilization.

To better understand electron charge redistribution, charge density differences were calculated (Figure 3.3). For clarity, charge density differences between undoped and doped structures were calculated for the same dopant site, and in the case of Co will not reflect the exact bonding environment present in the minimum E_{Ov}^{F} value. However, for the intent of observing change in charge distribution, the simulation yields fundamentally applicable results. Intuitively, Al-doping presents a local charge deficiency, and the redistribution of charge on surrounding O 2p orbitals is a coulombic effect; this redistribution is local, and does not extend far beyond the immediate AlO6 octahedron. Converse to Al, Ti-doping predicts an increased charge density on the oxygen in the surrounding TiO6 octahedron; though similarly, the charge redistribution does not extend beyond the octahedrally coordinated oxygen. Variations in the charge density of Co- and Ti-doped structures reflect the modified bonding relative to the original Mn environment. The Co bonding results in a charge reduction on surrounding oxygen ions; as this Co is actually neighboring the lowest E_{Ov}^{F} site, this oxygen ion will directly experience the reduced charge density and will more directly impact this site. Last, Mo shows the most significant charge redistribution,

increasing charge density to local oxygen p orbitals. Interestingly this charge redistribution extends beyond the MoO6 octahedron, increasing the charge density of the trigonal-planer-like oxygen site, a potential source of reduction of E_{Ov}^F.

E_{Ov}^F results are further described by the DOS calculations of the lowest E_{Ov}^F oxygen site and surrounding ions. Figure 3.4 shows that most dopants have little local impact on the DOS of this site, but for the case of the Mo-dopant a notable shift of the energy of local bonding orbitals below the Fermi energy is observed. This shift creates a barrier to charge transfer between bonding and antibonding orbitals for this particular oxygen ion, subsequently impeding the removal of oxygen from the oxygen sublattice. Integration of the oxygen DOS between the Fermi energy and -1.5 eV shows a 27% increase in the electron density in the O 2p orbitals. This extra charge, due to the charge reconfiguration from Mo-doping, is the likely source of the relatively increased Fermi energy of the local bonding orbitals.
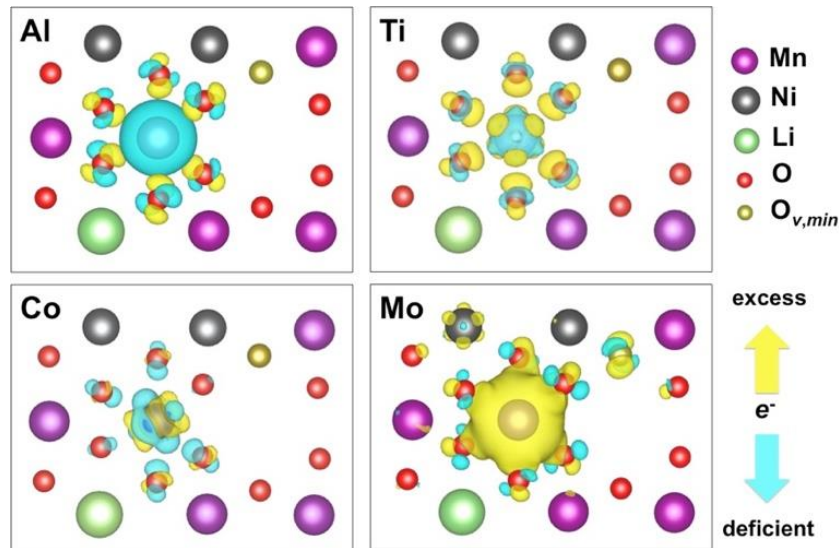
Figure 3.4. The difference in charge densities between undoped and doped structures (delithiated state; iso-surface of 0.01 electrons/Bohr^3) elucidates the alteration of electron distribution and bonding upon introduction of a dopant. Most notably, Mo-doping results in diffusely distributed electron excess, having a more notable change to the most susceptible bonding environment to oxygen loss. $E_{Ov,min}^F$ (gold ion) denotes the minimum E_{Ov}^F site.

3.3.3. Experimental Observations

Guided by the E_{Ov}^{F} calculations, synthesis preceded with the dopants previously discussed in terms of calculation results: Co, Mo, Al, and Ti are incorporated into pristine Li-rich layered oxide cathode (LNMLO). Co-doped LNMO (LNMLO-Co) was examined to observe the potential decrease in oxygen stability of the cathode material. It is known that Co readily forms a solid solution with LNMLO at large concentrations, allowing an amount of Co to be doped into LNMLO consistent with calculations. Shown in the works of Deng et al.[14] and Wang et al.,[61] electrochemical cycling can be partially described in terms of the calculated oxygen stability. The initial charging plateau in the cycling profile is attributed to both reversible anion redox and irreversible oxygen evolution. As predicted computationally, the Co-doped sample shows an extended initial charging plateau relative to the undoped material. As shown in Figure 3.5a, the plateau length of LNMLO is 228.0 mAh/g, while that of LNMLO-Co increases to 266.9 mAh/g. Cycling instability of the material is further presented in the form of the severe voltage decay after 50 cycles, shown in Figure 3.5c. The average voltage retention after 50 cycles decreases from 97% to 93.6% after Co doping. As compared in Figure 5e, LNMLO-Co delivers significantly improved discharge capacities in the initial several cycles but drops sharply. The LNMLO-Co shows a first discharge capacity of 290 mAh/g, while that of pristine LNMLO only delivers 220 mAh/g reversible capacity. This increased capacity in LNMLO-Co may be due to the increased activation of redox-active oxygen. After 50 cycles, the capacity of LNMLO-Co only maintains 79.3% of initial capacity, 230 mAh/g. Yet, the capacity of LNMLO slightly increases to 232 mAh/g. The experimental observations are in complete agreement with the computational prediction that Co doping leads to decreased oxygen stability, resulting in increased irreversible oxygen gas evolution.
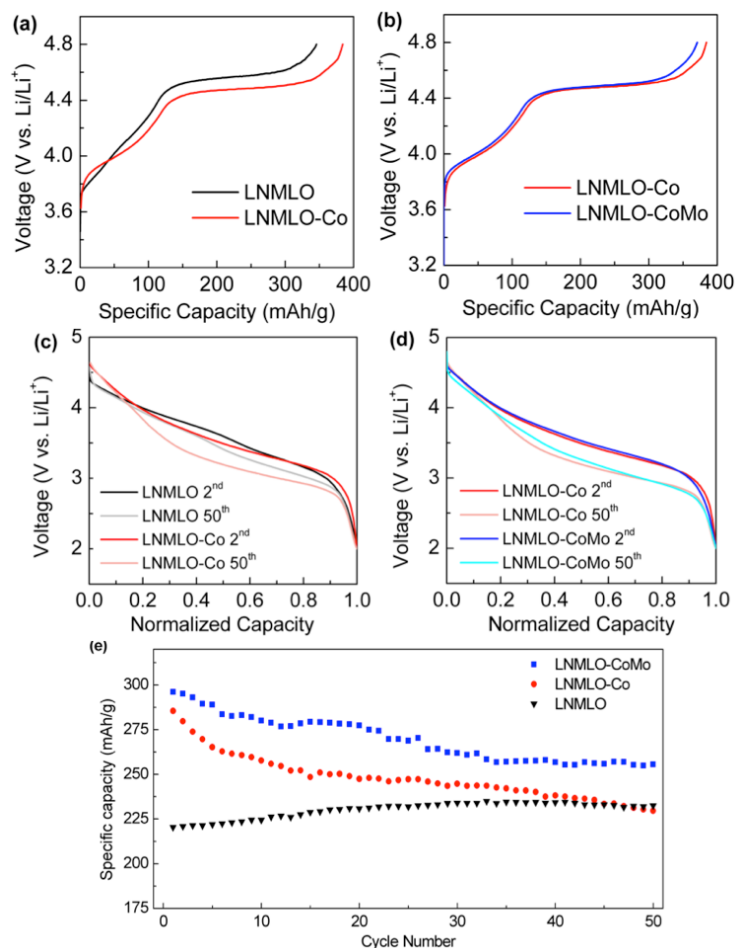
Figure 3.5. Cycling results of LNMLO, LNMLO-Co, and LNMLO-CoMo. Incorporation of Co (a) is shown to increase the initial charging plateau, where Mo-doping (b) reduces the plateau, suggesting reduced oxygen gas evolution. Mo-doping further shows reduced voltage decay (d) and improved capacity retention (e).

Table 3.1. A comparison of electrochemical performance parameters of LNMLO, LNMLO-Co and LNMLO-CoMo.

	Plateau length (mAh/g)	Average voltage (Cycle 50)	Specific capacity (Cycle 1/50, mAh/g)	Capacity retention (Cycle 50)
LNMLO	228.0	97.0%	220/232	105%
LNMLO-Co	266.9	93.6%	290/230	79.30%
LNMLO-CoMo	253.4	94.2%	297/256	86.50%

Aiming to provide insight for practical application, obtaining high energy density while maintaining excellent cycling stability, Mo doping is performed on LNMLO-Co material (LNMLO-CoMo). 1% of Mo was doped into bulk of LNMLO-Co, as will be evident. Doping of 3% of Mo into LNMLO-Co structure was also attempted; however, impurity peaks appear, consistent with previous literature. 1% is likely near the maximum amount of doping into the structure, due to the large ionic radius of Mo.[73] The first charging curve of LNMLO-CoMo (Figure 3.5b) shows a reduced initial charging plateau (253.4 mAh/g) compared with LNMLO-Co (266.9 mAh/g). This indicates, conversely to the Co material, a reduction in electron charge transfer from oxygen, which would otherwise accompany the irreversible oxygen loss from the lattice. The material also shows moderately less voltage decay after 50 cycles (Figure 3.5d). The average voltage retention improves by 0.6% with Mo doping. Last, and most notably, the specific capacity and cycling stability are greatly improved. As shown in Figure 3.5e, LNMLO-CoMo delivers a high reversible capacity of 297 mAh/g. After 50 cycles, the capacity remains 256 mAh/g with retention of 86.5%. Note that the coulombic efficiency can be further improved upon application of surface treatment,[12] though in this work we focus on the bulk doping only. A detailed electrochemical performance comparison of the three samples is shown in Table 3.1. EIS measurements are also carried out to understand the variation in electrochemical behaviour of LNMLO-Co and LNMLO-CoMo. In the pristine state, both compositions are dominated by charge transfer resistance, and after 30 cycles an SEI component is observed. Though the Mo-doped sample shows reduced charge transfer resistance before and after cycling, and much smaller SEI component after 30 cycles, indicating improved electron transfer and lithium ion diffusion with only 1% incorporation of Mo. The above results clearly demonstrate the positive effect of Mo doping on electrochemical performance.
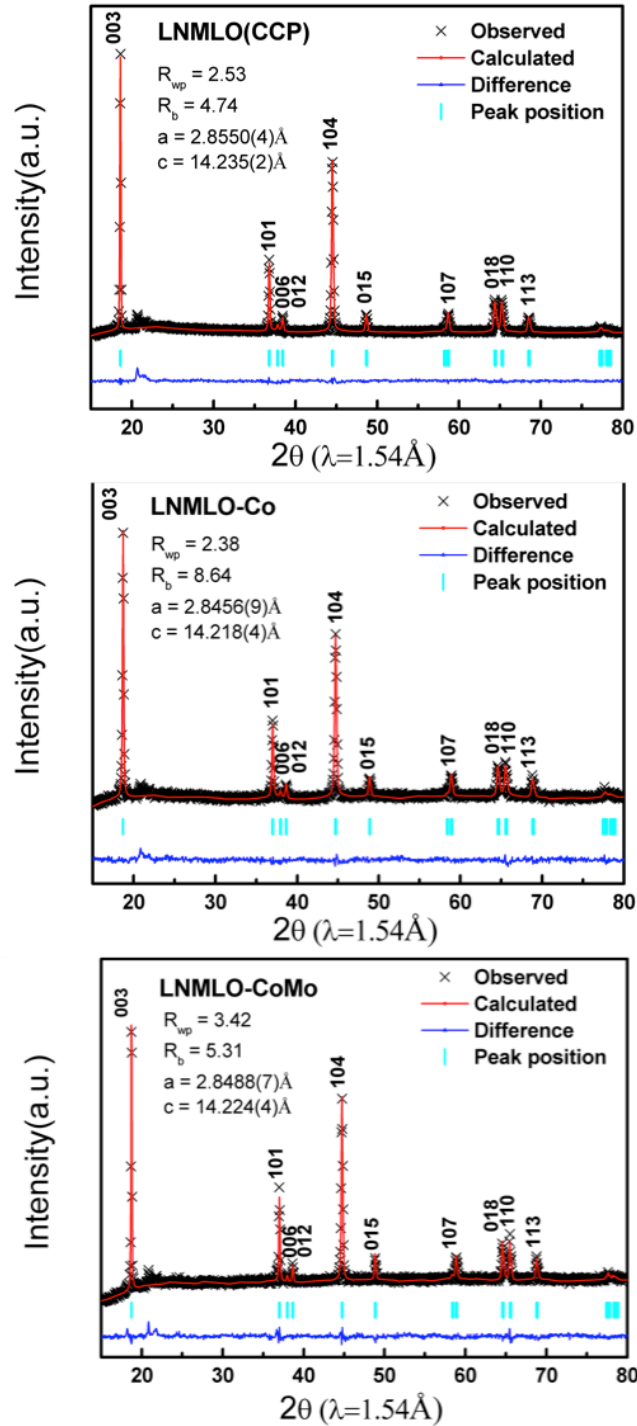
Figure 3.6. X-ray diffraction and Rietveld refinement of LNMLO, LNMLO-Co, LNMLO-CoMo,. As the ionic radius of Co^{3+} is smaller than Ni^{2+} and close to Mn^{4+}, NMC shows shrink lattice parameters. After 1% of Mo doping, both a- and c- of LNMLO-CoMo increase compared with LNMLO-Co, indicating Mo has been successfully doped into LNMLO-Co structure.

The incorporation of Mo into the structure was verified by XRD, XPS, STEM, and EDS: (1) Via XRD and Rietveld the lattice parameter variation trends of the three materials are determined (Figure 3.6). Co^{3+} (0.545 Å) doping leads to shrinking of a- and c-lattice parameters compared with pristine LNMLO. A slight a-lattice expansion is caused by Mo^{5+} (0.61 Å) substitution into the structure, also noting that Mo^{5+} doping causes significant expansion of the c-lattice parameter due to the increased Mo-O bond length. The increased c-lattice parameter facilitates Li^+ diffusion, explaining in part the increment of capacity in LNMLO-CoMo material. (2) Figure 3.7 compares the XPS analysis of LNMLO-Co and LNMLO-CoMo samples. Results of the XPS suggest that most of the Mo dopant takes the Mo^{5+} oxidation state in the pristine state. Specifically, the two peaks at binding energies of 231.7 eV and 234.8 eV are attributed to Mo^{5+}. Weak shoulders at higher binding energy of 232.8 eV and 236 eV indicate a small amount of Mo^{6+}.[74] Oxidation states of TM's are predicted using magnetization data from DFT calculations, and calculate Mo in the pristine state to have a +5 charge. This dopant is predicted to be oxidized to Mo^{6+} on the first delithiation, not explored in this work. Oxidation states of Ni show no change,
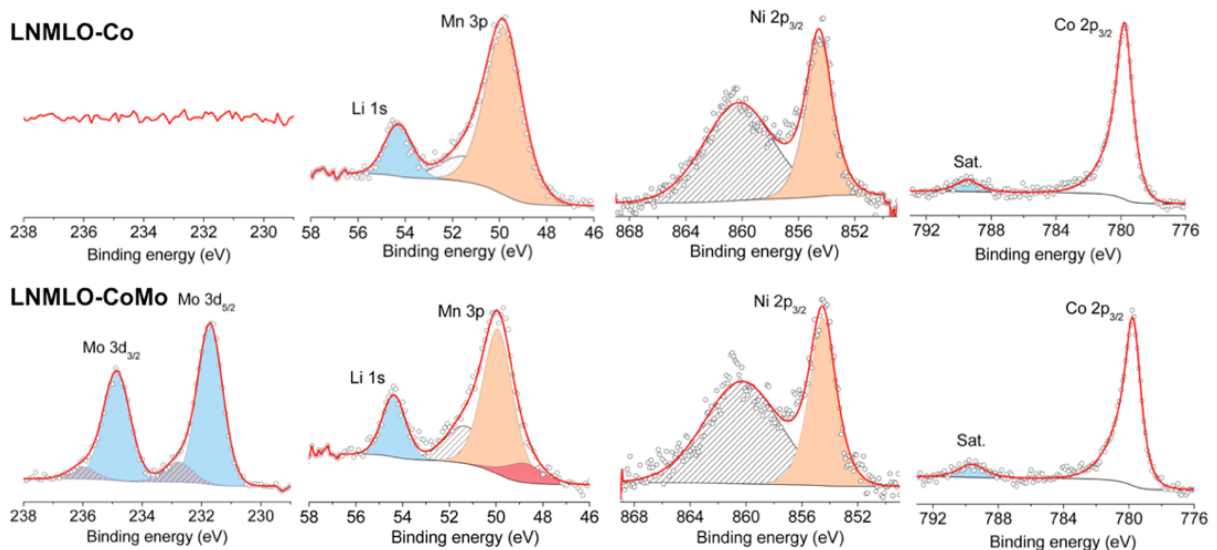
Figure 3.7. XPS of LNMLO-Co and LNMLO-CoMo show that Mo took the predicted Mo^{5+} valence. Results further show a portion of the Mn is reduced from Mn^{4+} to Mn^{3+} with the incorporation of Mo.

as the peak at 854.5 eV does not shift after Mo doping. Mn appears to be slightly reduced, again consistent with computation results. The predicted mixed valence of Mn may enhance the conductivity of the material, partially explaining the increased specific capacity.[73] Co is slightly reduced after Mo doping, as the satellite peak area increases from 6.84% to 8.99% after doping.[75] (3) The most convincing evidence comes in the form of aberration corrected high angle annular dark field (HAADF) STEM images of pristine particles (Figure 3.8). Incorporation of Mo is clearly
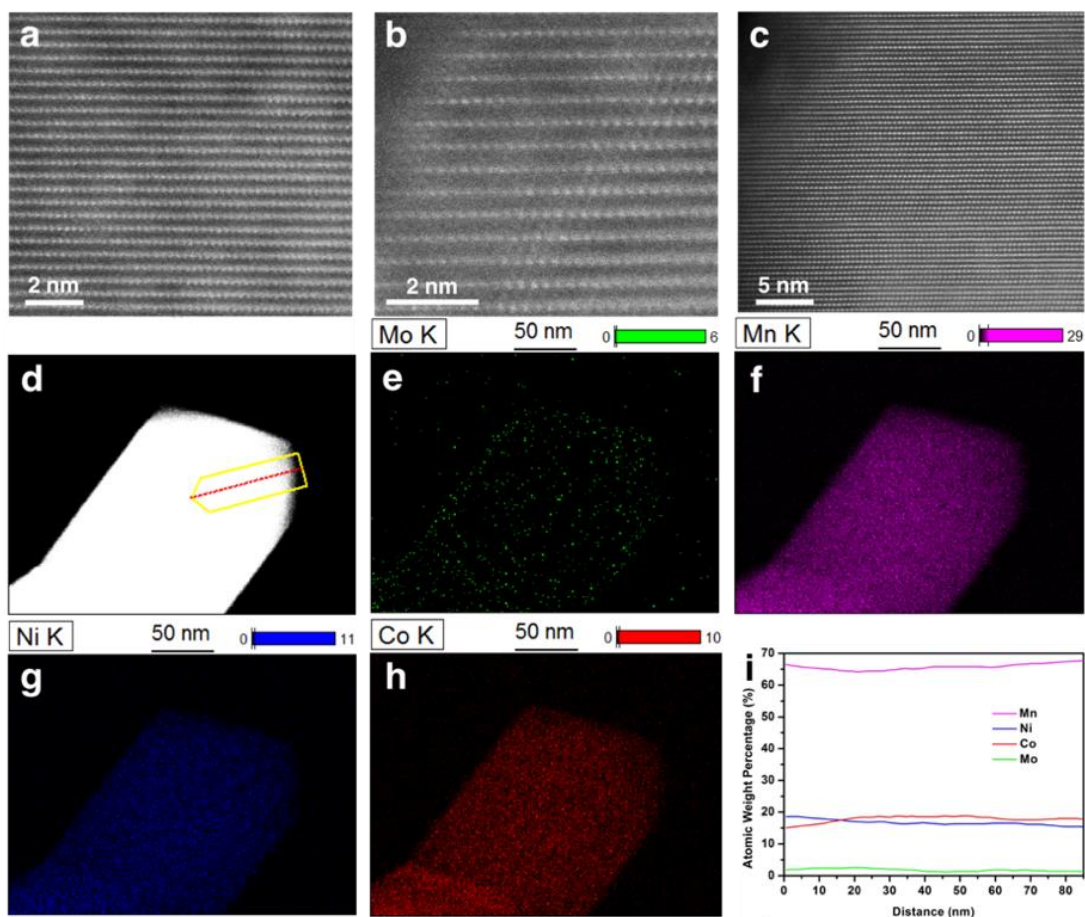
Figure 3.8. HAADF images of pristine LRLO-CoMo (a) bulk and (b) surface, and (c) pristine LRLO-Co, showing both surface and bulk. STEM/EDS mapping of a primary particle shows a uniform distribution of all constituents (e-h). Quantitative analysis (i) was attained by an EDS line-scan, acquired along the red line in the direction of the yellow arrow in (d).

correlated with an increase in lattice strain, as evident by the contrast non-uniformity in the doped particle (Figure 3.8a). Transition metal migration to the lithium layer was observed near the particle sub-surface, likely correlated with the increased strain (Figure 3.8b).[53] HAADF image of the pristine LNMLO-Co shows a typical structure with well layered properties in the bulk of the pristine material extended to the surface (Figure 3.8c). (4) EDS mapping of a primary particle of LNMLO-CoMo acquired in STEM shows a uniform distribution of all transition metal constituents (Figure 3.8e-h). Quantitative data acquired by line scan (Figure 3.8d) show the transition metals in the appropriate concentration from synthesis, and further illustrate the uniform distribution through the surface and bulk (Figure 3.8i). Mo distribution homogeneity was also observed by EDS of cross-sectioned secondary particles within a dual-beam FIB/SEM. It is noted that Mo-doping has indeed been explored for lithium rich layered oxides Li_2MnO_3,[76] $Li[Li_{0.2}Ni_{0.2}Mn_{0.6}]O_2$,[73] and $Li[Li_{0.2}Mn_{0.54}Ni_{0.13}Co_{0.13}]O_2$,[77,78] and in the case of Li_2MnO_3, Mo^{5+} was observed by X-ray absorption spectroscopy. Though again, little to no emphasis was placed on the stabilization of oxygen within the lattice in these prior works. We further incorporated Al and Ti dopants into the pristine LRLO structure, as discussed in the Supplemental Information, showing results commensurate with calculated prediction, with little to no change is observed in the length of the high voltage oxygen-redox plateau.

Experimentally, a variety of dopants, including Al, Ti, Co and Mo, were selected to evaluate the impact on initial charge plateau, voltage fade, and capacity loss, and results are presented in the context of ab initio calculations. The observed electrochemical performance suggests that Al and Ti doping shows little impact on oxygen activities, having no effect on the width of the initial charging plateau; Co leads to decreased oxygen stability, increasing the width of the plateau; incorporation of Mo can mitigate oxygen loss from the lattice to some extent—

consistent with E^F_{Ov} calculations. In this work, both theoretical and experimental findings show Mo-doped LNMLO shows the highest specific capacity and improved cycling stability.

3.4. Conclusions

Oxygen vacancy formation energies, E^F_{Ov}, were calculated for a wide range of dopants using ab initio calculations. The range of calculated E^F_{Ov} were shown to be strongly dependent on local environment, both compositionally and structurally. The source of E^F_{Ov} change between dopants was attributed to the charge density modification and subsequent change in band structure, increasing the E^F_{Ov} in the case of a Mo dopant. These calculated E^F_{Ov} values guided experimental doping, showing results in line with computational prediction. Al- and Ti-doped materials showed little change to the initial charging plateaus, consistent with the predicted E^F_{Ov}, where Co-doping showed an increase in the plateau width, indicating exaggerated oxygen loss from the lattice. Mo-doping experiments shows improved cycling stability through reduced voltage decay, suggesting oxygen is stabilized by the incorporation of Mo. Experiments show the presence of a majority of Mo^{5+} ions, as predicted. When considering the nature of oxygen activity within cathode material, it is clear that the formation of molecular oxygen in the bulk of the material accounts for the majority of this irreversible capacity loss. As such, methods of mitigating must extend beyond surface modification. Calculation results show that doping of particular elements (Mo and Ru) work to reduce the degree of oxygen loss from the lattice, while leaving the oxygen available for redox. However, the degree of dopant incorporation is limited by solubility of the dopant in the structure. This work validates cationic substitution as a fundamental method of improving capacity retention of lithium rich layered oxide cathodes, and should be combined with advanced surface modification to result in improved high capacity cathodes. This work further demonstrates the

application of density functional theory towards the rational design of cathode materials, streamlining the design process and speeding the optimization of these materials.

Chapter 3, in part, is a reprint of the material as it appears in the Journal of Materials Chemistry A. Wynn, Thomas A.; Fang, Chengcheng; Zhang, Minghao; Liu, Haodong; Davies, Daniel M.; Wang, Xuefeng; Lau, Derek; Lee, Jungwoo Z.; Huang, Bo-Yuan; Fung, Kuan-Zong; Ni, Chung-Ta; Meng, Ying Shirley, Journal of Materials Chemistry A, 6 (2018) 24651-24659. The dissertation/thesis author was the co-primary investigator and author of this paper.

Chapter 4. Resolving the structure of amorphous solid-electrolyte LiPON

4.1 Introduction

Solid-state lithium ion conductors are attractive electrolytes for next generation lithium ion batteries due to their improved safety and their potential to improve energy density by enabling lithium metal anodes. Though the fundamental properties leading to their relative stability against lithium metal, with the goals of achieving high coulombic efficiency and preventing catastrophic failure via cell shorting, are currently disputed. Electrochemical stability of solid-state interfaces has recently been described by modified phase diagrams, as suggested by computational thermodynamic evaluations. This work has predicted the electrochemical stability windows of a wide range of solid electrolytes, drawing parallels between solid and liquid electrolytes by the formation of interphases.[18,28] However, mechanisms of electrochemical decomposition are incomplete, generally lacking kinetics of models. Tang et al. applied ab initio molecular dynamics (AIMD) to simulate dynamic decomposition at a well-defined crystalline interface of sodium metal and sodium thiophosphate.[79] Crystalline compounds have been particularly straightforward in prediction, however compounds of interest such as amorphous lithium phosphorus oxynitride (LiPON) and amorphous lithium thiophoshates (LPS) are both experimentally and computationally complicated: experimentally, methods for explicit structural determination are limited; computationally, disordered solids are more difficult given the prevalence of periodic boundary conditions in most theory. Existing kinetic models for the Li/LiPON interface have generally utilized configurations incommensurate with recent literature, overestimating structural instability through an overabundance of metastable coordinations. In this regard, accurate local structural descriptions are of utmost importance in describing the chemical environments leading to their varied degrees of stability.

LiPON, the focus of this work, is particularly interesting due to its remarkable cyclability against lithium metal—a crucial requirement for next-generation lithium ion components.[21] This stability has been attributed to a number of features of the solid electrolyte: highly electrically insulating and ionically conducting decomposition products, Li_3P, Li_3N, Li_2O, as predicted via density functional theory (DFT) and suggested by in situ x-ray photoelectron spectroscopy (XPS)[17–19]; kinetic stability of the interface components[80]; low electronic conductivity (10^{-15}-10^{-12} S cm^{-1})[27], and supposed mechanical rigidity[81] are among a few. However, recent work regarding the local bonding environments of the glassy electrolyte suggests that much of the work previously used to describe the significance of LiPON's structure may require reinterpretation. Guille et al. and Lacivita et al. have recently reframed the impact of N in the amorphous LiPON structure, proposing the commonly interpreted triply-bonded N, N_t, rather be a substitution of an oxygen in a PO_4 tetrahedron, referred to as apical N, or N_a.[82,83] Efforts to describe the local structure have been performed via neutron pair distribution function (PDF) analysis on RF sputtered thin films and NMR on ion-beam-assisted deposition (IBAD)[84] and bulk lithium phosphonitride glasses,[85] though NPD leaves structural ambiguity between N and O environments, and bulk and IBAD LiPON glasses have not exhibited the notable stability of thin film batteries produced via RF-sputtering, capable of producing films with reasonably high ionic conductivity (2-3x10^{-6} S cm^{-1}). As attempts to produce LiPON via other routes (atomic layer deposition, pulsed laser deposition, bulk glass processing, etc.) have proven less effective, it begs to question the significance of RF sputtering in the production of an effective LiPON electrolyte. In this work, we employ nuclear magnetic resonance (NMR), particularly 2D techniques to differentiate the local chemical shift anisotropic features further permitting structural determination, to unequivocally resolve the local structure of RF-deposited LiPON, and the relationship between processing method and its relative

stability as a glassy solid electrolyte. Density functional theory is employed using the gauge included projector augmented wave (GIPAW) framework to calculate the chemical shifts of a variety of lithiated phosphate glasses, developing a database of local bonding environments and their relative chemical shielding, which are correlated to the measured chemical shifts from NMR measurements. These results are then used to validate AIMD-driven amorphization of LiPON solid electrolyte. Structural validation is crucial in future evaluation of the high degree of cyclability observed in this material, as well as developing an atomic level understanding of the (electro)chemical stability of this electrolyte when paired with lithium metal.

4.2 Results and discussion

4.2.1 Baseline properties of thin film amorphous LiPON

LiPON thin films were tested for ionic conductivity, bonding and stoichiometry using electrochemical impedance spectroscopy (EIS) and x-ray photoelectron spectroscopy (XPS), respectively. EIS, performed in parallel plate configuration with Pt blocking electrodes, produced an ionic conductivity of 2×10^{-6} S/cm, on the order of those produced in literature via RF sputtering (Figure 4.1a). XPS (Figure 4.1b) results are consistent with literature, showing minimal surface contamination, viewed through the C intensities, and bonding consistent with films previously reported. However, per recent literature discussion,[82] the peak observed around 399 eV is attributed to the apical nitrogen sites, rather than the commonly interpreted N_t. Fit parameters of the XPS data is shown Table 4.1.
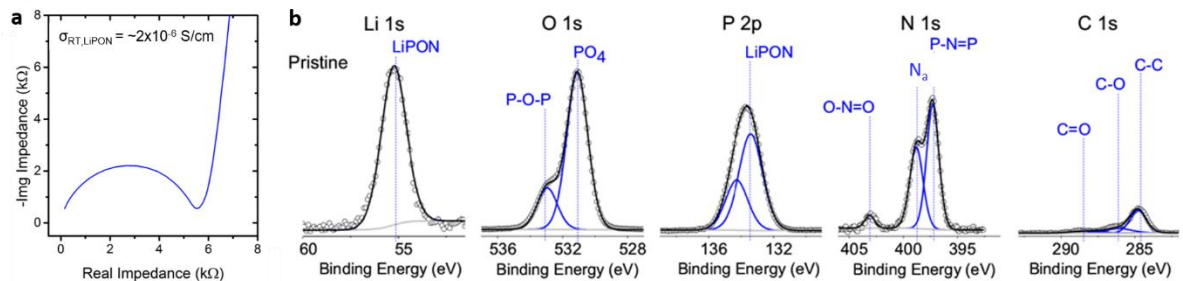
Figure 4.1. Baseline properties of LiPON determined by (a) electrochemical impedance spectroscopy and (b) x-ray photoelectron spectroscopy.

Table 4.1. Fit for LiPON XPS spectrum.

	Li 1s	O 1s	P 2p	N 1s	C 1s
LiPON	55.1		133.0		
	55.0 55.6		132.8[7]		
	55.4[8] 55.8		133.6		
P-O-P		532.6			
		532.7 532.8			
		533.0[6] 532.3[9]			
PO_4		531.0			
		530.6[5] 531.3[9]			
		531.4[6]			
O-N=O				403.1	
				~404[10]	
$P-N_a$				398.7	
				398.6[5] 399.0[6]	
				398.9[10] 399.4[9]	
P-N=P				397.2	
				396.6[5] 397.6[6]	
				397.4[10] 397.8[9]	
Li_2CO_3	55.3	531.6			289.6
	55.3[11]	531.9[11]			290.1[11]
	55.2[12]	531.5[12]			289.8[12]
LiOH	54.6	531.1			
	54.7[11]	531.1[11]			
	54.9[12]	531.3[12]			
NH_3				398.6	
				398.5-400.9[13, 14]	

4.2.1 Isotropic chemical shift of Li_3PO_4 and LiPON thin films

Magic angle spinning NMR was performed on crystalline Li_3PO_4 (c-LPO) target material and RF-sputtered amorphous films of Li_3PO_4 (a-LPO) and LiPON, shown in Figure 4.2 and Figure 4.3. NMR is sensitive to short range structure, making it an invaluable tool for structural identification of glasses wherein the connectivity of structural units are resolved as separate

chemical shifts. The typical connectivity nomenclature for phosphate glasses is given by the number of bridging oxygens per tetrahedral P atom, Q^n, where n is the number of bridging atoms. A network composed of Q^3 units is three dimensional, whereas a Q^2 network is defined by chains.[86] In the case of highly lithiated phosphate glasses, cations act to depolymerize the network by forming non-bridging oxygen atoms randomly throughout the network, thus direct insight into the network connectivity is gained by tracking the population of the Q units. The ^{31}P chemical shift for c-LPO has a sharp peak at 9.6 ppm in accordance with phosphate tetrahedra having four non-bridging oxygen, Q^0, and deemed 'isolated' tetrahedra as they do not share any oxygen atoms with neighboring P tetrahedra (Figure 4.2a). After amorphization, a-LPO shows a broadening of the Q^0 peak indicating structural disorder from a distribution of bond lengths and angles producing a distribution of the chemical shifts (Figure 4.2b). A shoulder is observable at 2.97 ppm that can be attributed to dimeric P_2O_7 units, Q^1, suggesting that some Li is lost during the sputtering process, as alkali phosphate glasses follow a random binary distribution in terms of Q speciation with cation concentration.[87]
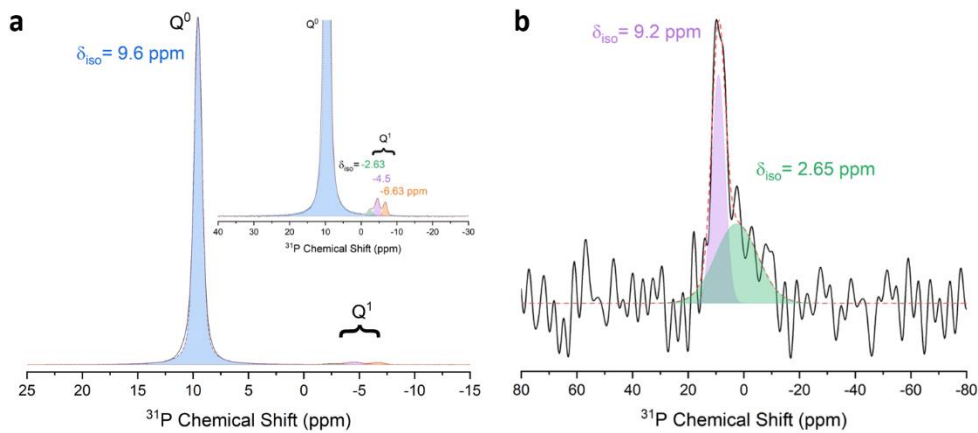
Figure 4.2. ^{31}P NMR spectra of (a) Li$_3$PO$_4$ target and (b) amorphouse Li$_3$PO$_4$ thin film.
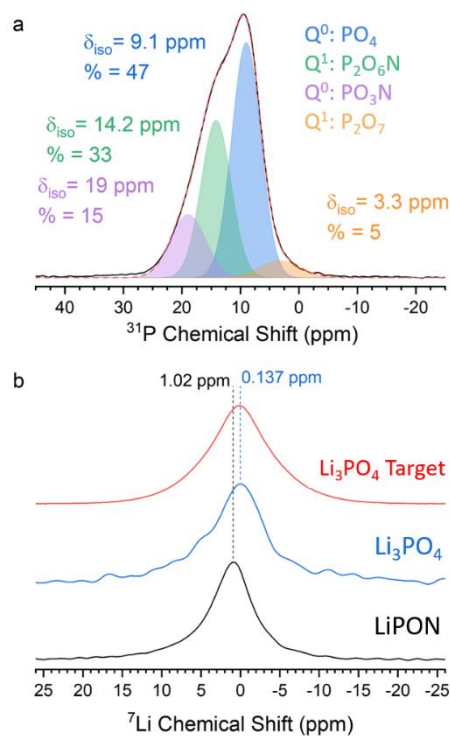
Figure 4.3. (a) ^{31}P MAS NMR spectra of thin film LiPON, (b) ^{7}Li MAS NMR spectra of Li$_3$PO$_4$, amorphous Li$_3$PO$_4$, and LiPON.

The MAS ^{31}P spectrum of a LiPON film (Figure 4.3a) bears resemblance to the a-LPO spectra with the predominant intensity at 9.1 ppm and a small tail around 3 ppm; these sites can be comfortably assigned to Q^0 and Q^1 phosphate species. However, in contrast to the a-LPO film, there are additional shoulders to higher chemical shift that are presumed to be phosphorus bonded to N. Deconvolution of this spectra is non-trivial, especially the region association with nitrided species, as there are very few ^{31}P NMR reports from literature on alkali oxynitride phosphorus compounds and how N is incorporated into alkali rich phosphate glass compositions is not known a priori. All previous studies investigating the effect of nitridation have focused on metaphosphate compositions. The result of an exhaustive NMR investigation combined with first principle calculations on a database of relevant lithium containing oxynitride phosphorus compounds and AIMD simulations of LiPON provides guidance into deconvoluting this region and elucidating

their chemical environments. These efforts are outlined below and are detailed in the Supplementary Information. The ^{31}P spectra of LiPON is deconvoluted into 4 peaks, the majority of which is composed of Q^0 PO$_4$ units at 9 ppm, followed by Q^1 PO$_3$N dimer units in which the N is bridging two PO$_3$ tetrahedra whose δ_{iso}=14.2 ppm; the other nitride species at 19 ppm is assigned to Q^0 PO$_3$N units, and a minor amount of Q^1 PO$_4$ dimers as previously mentioned. These assignments give important insight into how N is incorporated into the LPO network, suggesting that N acts very similarly to O, as an anion forming bridging (as that observed in the Q^1 site) and non-bridging (in the Q^0 site) nitrogen. One of the key benefits of NMR, especially in nuclei such as ^{31}P which are 100% abundant, is that it is a quantitative technique and can help further understand and put constraints on modelling the local structure for future studies. The overall line shape is generally similar to that of previously published NMR of IBAD deposited LiPON, with similar peak broadening associated with the wide range of environments with N incorporation.[84] However, results of this fitting show that RF-sputtering introduces larger amounts of Q^0 and Q^1 groups with N content; this is reasonable, as RF-sputtered films interact directly with the nitrogen plasma, and IBAD films were observed to contain notable N$_2$ gas content.[84] ^{6}Li and ^{7}Li chemical shifts were also observed to vary between the lithium phosphate and LiPON samples. Both ^{6}Li and ^{7}Li shifts of LiPON increase by 1 ppm relative to c-LPO target and amorphous lithium phosphate thin films as a result of the nitrogen deshielding the lithium nuclei. The ^{7}Li line shape of LiPON is narrowed slightly relative to a-LPO suggesting increased Li conductivity, in agreement with dielectric spectroscopy measurements.[88] It should be noted, the ^{7}Li LiPON lineshape has a Lorentzian character indicating the Li ions are rapidly exchanging with one another, hence a single peak is observed and all the Li ions are mobile within LiPON.

4.2.2 Computational spectroscopy of alkali nitridophosphates

To accurately correlate NMR chemical shifts with local structures and remove ambiguities in the isotropic environments, we employ DFT calculations to simulate the effective electronic shielding. Recent implementation of the GIPAW approach has enabled precise determination of electronic shielding effects on nuclei,[89] directly related to the chemical shifts determined via NMR measurements, specifically of the ^{31}P nuclei.[90] To resolve the data observed in literature, and to provide a map of the potential bonding environments present in lithiated phosphate glasses, the VASP implementation of the GIPAW approach was applied to a body of Li-P-O-N containing compounds of varied compositions and bonding environments.
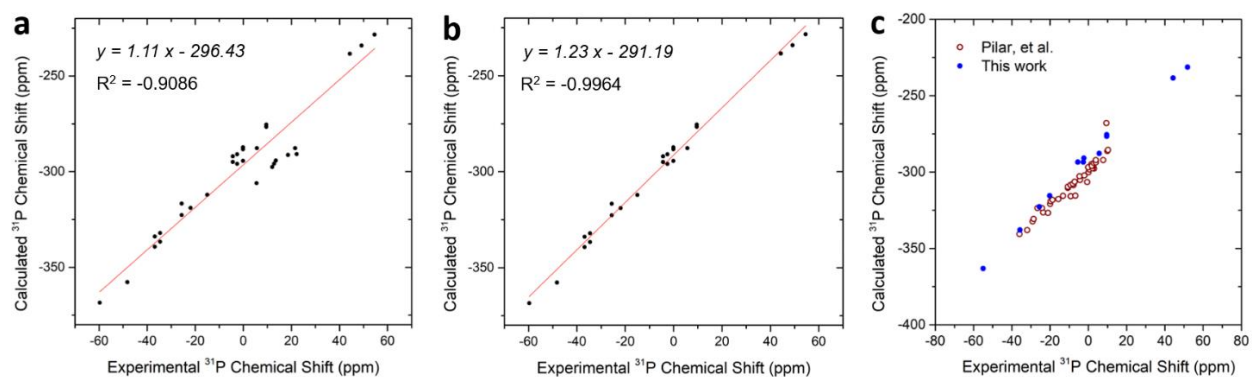
Figure 4.4. Comparison of calculated and experimental chemical shifts of lithiated phosphates to non-lithiated phosphates in literature (a) with and (b) without data from reference Pilar, et al., with an ambiguous reference. Lithiated phosphate data (c) follows an alternate trendline compared to reported calculated phosphates.

Previous work simulating the electronic shielding of a body of phosphates showed a direct linear trend between experiment and calculated chemical shifts, though Li_3PO_4 showed distinct deviation from linearity.[90] While limited experimental NMR data exists for the full range of calculated lithiated structures due to the metastability of many phosphonitride variants, those present show a distinct linear trend between experimental work in literature and the calculated chemical shifts Figure 4.4. We note a deviation of approximately 20 ppm consistently from one

57

research group; we attribute this deviation to a lack of appropriate standard corrections. To confirm prediction of known structural groups, calculations were performed for Li_3PO_4 (Q^0 PO_4), $Li_4P_2O_7$ (Q^1 PO_4 dimers), and $LiPO_3$ (Q^2 PO_4 chains), along with some phosphonitride and phosphorus oxynitride variants, shown in Figure 4.5; when fit, the isotropic chemical shift is accurately predicted for both crystalline Li_3PO_4 and the Q^1 groups present in the lithium deficient amorphous films.
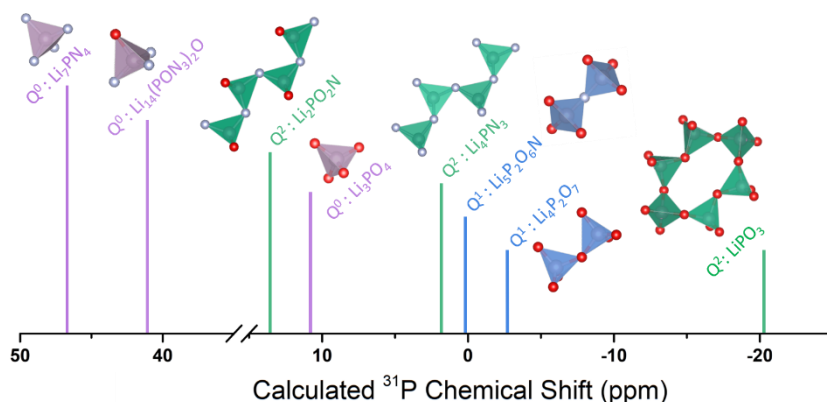
Figure 4.5. Calculated ^{31}P chemical shifts of a wide variety of structures containing structural units described above serve to guide peak fitting and determination of structural units.

Unsurprisingly, features associated with extended structures are not observed for sputtered lithium phosphate due to its high cation content. However, the lack of experimental data regarding lithiated nitridophosphates creates uncertainty in the fitting of 1D NMR spectra, requiring further exploration of the local structures by other means. Computational exploration of a variety of metastable compounds with local environments reminiscent of those present in LiPON hint at the importance of 2D NMR spectroscopic methods. The PO_4 tetrahedra serves as an ideal reference, due to its charge symmetry, showing minimal anisotropic signatures. Simulation of a body of lithiated PO, PN, and PON compounds (Figure 4.6) clearly shows that reduced Q^n results in an increased chemical shift. Reduced Q^n is generally accompanied by increased Li content, though the trends are convoluted with nitrogen incorporation. To decouple this convolution and enable

full structural determination, anisotropic shielding is employed (Figure 4.6); exploration of a series of Li-P-O-N compounds shows distinct clusters in isotropic shift and CSA based on Q^n speciation and composition, which can be used to identify local structures in unknown structures of similar composition. Interestingly, calculations of lithiated phosphates show a similar linearity based on lithium content (Figure 4.4c), with a varied slope from the non-lithiated phosphate species.
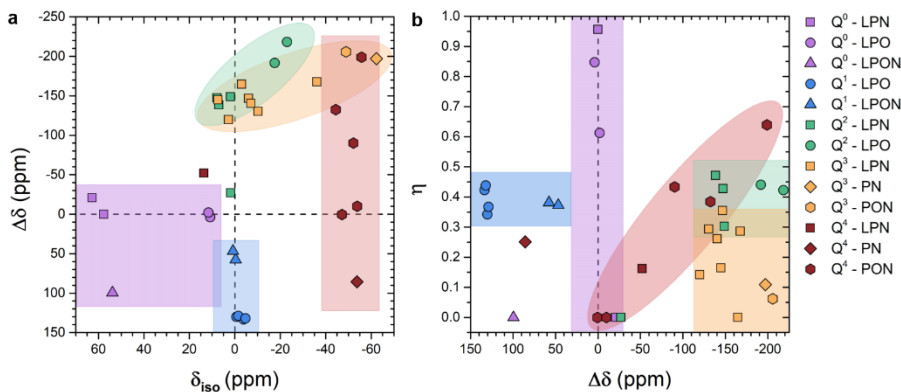
Figure 4.6. Calculated chemical anisotropy calculations for the range of Li-P-O-N based compounds show distinct groupings related to their bonding configuration and local composition.

Further insight may also be gained regarding the nature of N incorporation in LiPON. Many reports, primarily spurred by unvalidated XPS assignments, stated N is coordinated to 3 P (N_t) in LiPON and related phosphorus oxynitride glasses. This scenario would result in a tricluster of P tetrahedra linked together by the same N. However, N_t is not observed in any lithiated nitride-phosphorous compounds but rather in non-lithiated structures such as P_3N_5, P_4N_6O, and Si_3N_4. Further, in the case of P_3N_5 and P_4N_6O, both of which are isostructural, the N_t site includes one corner-sharing and two edge-sharing tetrahedra. Among all simulated compounds, bonding to N_t results in a calculated ^{31}P chemical shift of approximately 50 ppm lower relative to that coordinated to bridging N (N_b) and N_a, well beyond the range of observed calculated ^{31}P isotropic chemical shifts associated with Q^0 and Q^1 environments measured in LiPON. This finding is consistent with that of Lacivita, et al. and Guille et al., emphasizing the lack of N_t via NMR. Further literature

review of ^{31}P assignments in sodium nitrided metaphosphate glasses similarly assign a 30 ppm shift to N_t, however the expected chemical shift difference between a 2 and 3 coordinated N is calculated to be 70 ppm, further suggesting the unlikelihood of N_t in alkali metaphosphate glasses and emphasizing the misidentification of N_a across multiple experimental techniques and compounds. Further discussion of the N bonding environments is included in the Supplementary Information.

4.2.3 Computational spectroscopy of AIMD generated LiPON glasses

Vapor deposited glasses have the potential for remarkably enhanced stability, with densities approaching the limit of disordered structures.[91] This motivated application of NVT AIMD simulations, emulating the enhanced density present in vapor deposited films. To both confirm application of the structural database to the amorphous structure demonstrated in LiPON, AIMD approach is employed to generate an amorphous structure with a stoichiometry of $Li_{2.9}PO_{3.5}N_{0.31}$, shown in Figure 4.7a.[83] Previous work by Lacivita, et al. performed AIMD-based melt quenches on a variety of LiPON stoichiometries, clearly linking the Li and N content to the potential for bridging configurations, and concluding the low density achieved through AIMD melt/quenching rules out previous interpretations of the opening of the structure, identifying decreased density, as the source of this improved conductivity.[92] However, distinctions between classical metaphosphate glasses and vapor deposited glasses emphasize limitations of the melt-quench method for producing the high-density glasses generally attained through physical vapor deposition. To emulate the high density of a vapor deposited glass, NVT quenches with densities on the order of crystalline analogues were performed. The AIMD- determined structures are generally consistent with that of Lacivita, et al., however, upon repeated
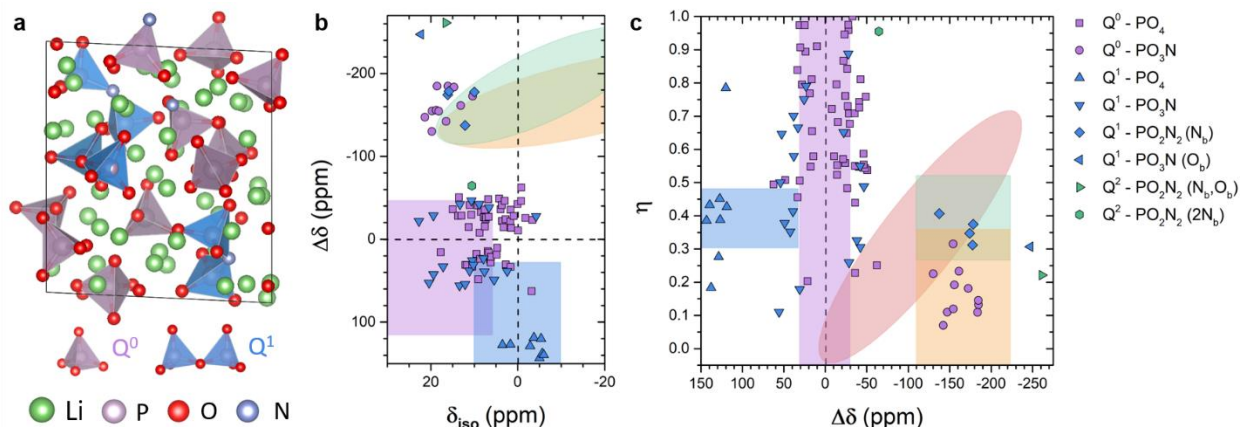
Figure 4.7. (a) The AIMD-generated structure of amorphous LiPON was used to calculate the (b,c) electronic shielding behavior used for determining the impact of local environment on chemical shift anisotropy.

melts and quenches, minor variations in coordination are observed including the formation of N_b trimers, clearly emphasizing the propensity for N as a bridging unit. Using this structure, GIPAW calculations are performed to calculate the relationship between bonding environment and electron shielding (Figure 4.7). Due to the variability of local lithium content within the structure, a wide range of isotropic shifts are present for the ^{31}P calculations. Consistent with fits performed for the calculated isotropic shifts, incorporation of N results in the highest among of de-shielding, where the lowest chemical shift is associated with bridging oxygen. More importantly, isotropic shift can be combined with CSA to couple these values, allowing clear resolution of the local structure, linking the anisotropic component to bridging coordinations. The combination of isotropic shift, $\Delta\delta$, and η clearly permit differentiation of ^{31}P associated with bridging O and N units, as described schematically in Figure 4.7b and Figure 4.7c. More notably, the incorporation of N appears as dominantly bridging and as apical, or non-bridging sites, as indicated by the peak shoulder observed around 19 ppm in Figure 1. Interestingly, simulations suggest that downshifts are attributed to both nitrogen- and oxygen-bridged dimers. However, through variations in symmetry

of charge density the local structure may be resolved. Here, the oxygen bridging species creates an asymmetry in one half of the P_2O_7 unit, resulting in a large anisotropic signature, whereas N bridging produces uniform electronic distribution around the P, showing little anisotropic shift.

4.2.4 2D NMR spectroscopy fitting of chemical shift anisotropies

Assignment of short-range structural environments in disordered materials relies not only on the isotropic chemical shift but also on the sites corresponding CSA. To separate the anisotropic component from NMR measurements, magic-angle turning and phase adjusted sideband separation (MATPASS) measurements and the $R12_5^4$ symmetry-based CSA recoupling sequence of the ^{31}P nuclei was performed. These measurements sequester the CSA into secondary dimension (y-axis), leaving the isotropic spectrum free of any CSA interactions and provides enhanced resolution. Additionally, these sequences provide the CSA for each isotropic chemical shift, allowing overlapping chemical shifts (like those observed here; see Figure 4.3) to be distinguished based on their CSA parameters.[93] Analyzing the CSA at various isotropic chemical shifts (Figure 4.8) reveals corresponding variations of the chemical shift anisotropy, Δ, and asymmetry parameter, η, with isotropic chemical shift. The two CSA correlation techniques reveal the CSA for all the chemical environments are similar, and only slightly vary with isotropic chemical shift.

Guided by results from the GIPAW calculations, fitting of the CSA recoupling reveals at least three unique sites. Two of the regions have similar Δ values but are distinguished by the difference in sign of Δ and a difference in their corresponding η, with the third region having relatively much higher CSA. These sites are respectively associated with (1) isolated or dimeric PO_3N tetrahedra, (2) isolated PO_4, again, accounting for majority of the bonding, and (3) dimeric PO_4 tetrahedra, confirming the convoluted fits of the isotropic chemical shift in Figure 4.3. In conjunction with the CSA correlation experiments, further insight into the chemical identity and
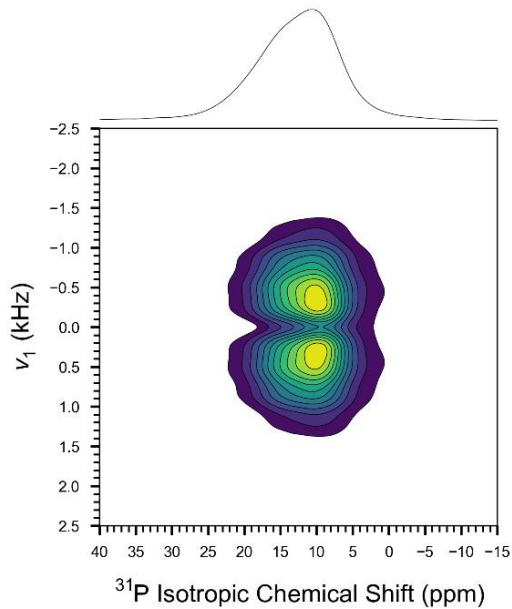
Figure 4.8. ^{31}P CSA recoupling contour plot.

connectivity of these P tetrahedra comes from double-quantum (DQ) correlation spectroscopy. The DQ correlation measurement relies on the short range homonuclear dipolar interaction and can reveal the connectivity of Q^n environments, potentially revealing details on extended chain environments. However, the DQ contour plot shows the intensity is smeared along the DQ-SQ diagonal, indicating that all P environments are auto-correlated with one another and any weaker homonuclear dipolar coupling are obscured by the broadening induced by structural disorder. These results further indicate there are no extended chain structures within LiPON and agree with the network structure dominated by isolated P tetrahedra (Q^0).

As LiPON is a glass, its extraordinary properties should be viewed in light of glass physics and chemistry. In most previous studies on nitride phosphate glasses, the modifier to glass former ratio is at or below 50% due to the difficulty in synthesizing crystal free glasses from cooling rates achievable through melt quenching.[94] Above 50% modifier, there is a strong driving force for crystallization, thus LiPON as a glass is beyond the compositional range typically investigated.

This is important to consider because of the network constraints the composition imposes: at low modifier content N_t can be accommodated into the network by the assumption that equal numbers of bridging O and non-bridging O are replaced requires three N_b species formed for every N_t species. N incorporation is not straightforward, and it could substitute with O, with little influence structure (dominant Q^0), or could act to connect the structure by forming Q^1 units through a bridged N.

In accordance to the ultra-stable glasses investigated by Ediger et al., vapor deposited glasses show remarkably low fictive temperatures indicating they are close to the bottom of the potential energy landscape, resulting in kinetic stabilities that cannot be reached by conventional heat treatments as the time scales exceed millions of years.[91] As LiPON is grown by RF sputtering (a form of physical vapor deposition), it is likely it too will display a low fictive temperature after deposition (results forthcoming in a future investigation). Previous work has explored the increased kinetic stabilization of LiPON via annealing at a variety of temperatures below the measured T_g of bulk counterparts. Among their results, heating temperature was shown to have little effect on elemental concentration, attributing all conductivity changes to structural and configurational modifications, albeit in 50 nm thick films.[95] While deposition is not controlled in these experiments, literature has reported an increase in temperature up to 110°C due to plasma heating of the film during deposition.[96] Such surface heating enhances mobility of surface ions, resulting in increased glass density and reduced entropy.[97] Coincidentally, this is below the critical annealing temperature observed before a severe ionic conductivity drop is observed (~150°C),[98] which may account for the variability in both Li and N content as a function of thickness. The potential for plasma heating is one further variable among the LiPON deposition field, and likely accounts for variable performance and stability. The implication of LiPON as a low fictive

temperature glass is that the energy difference between the glassy state and the corresponding crystalline state is minute, minimizing the thermodynamic driving force for crystallization and the enthalpy barriers for initiating that crystallization are too high to overcome on an experimental timescale. This enhanced kinetic stability observed in ultra-stable glasses could explain the superior electrochemical stability LiPON presents with Li metal. Even with the interfacial driving force to decompose, the kinetic stability of LiPON in its metastable form prevents the decomposition from occurring at a reasonable rate. The prevalence of Q^0 tetrahedra hint at the thermodynamic stability of the electrolyte itself, and if the temperature doesn't exceed T_g, LiPON remains a highly stable compound. However, at interfaces, particularly with Li, where it is thermodynamically predicted to decompose to constituents Li_3P, Li_3N, and Li_2O,[17,18] the high bond strength would suggest sluggish kinetics for decomposition. While some past studies disagree on the source of the enhanced ionic conductivity, whether related to the atomic packing density or to the nitrogen content, it is clear from both studies that N incorporation indeed alters the chemical environment of Li, and that critically dense structure may result in reduced ionic conductivity.

Last, there are important implications of the lack of connectivity observed in the highly lithiated phosphate glasses. The first takeaway from this new structural resolution, that largely agrees with the structural model presented by Lacivita, et al. using neutron scattering, indicates previous structural modelling attempts based on crystalline analogues with highly connected structures are not accurate representations of LiPON's structure. As the structure is dominated by Q^0 PO_4 and PO_3N groups with N acting to bridge about 30% of the phosphate tetrahedra as dimeric units, the overall LiPON network structure clearly does not contain any extended chain structures as indicated by absence of cross peaks in the DQ contour plot and by the large CSA values expected for Q^2 environments. The thermodynamic stability of the PO_4 tetrahedra is then a paramount

consideration. With respect to bond strength, N incorporation has been clearly identified as essential to the enhanced ionic conductivity of LiPON. Mechanically, the lack of connectivity coupled with the high cation concentration would suggest a lack of mechanical rigidity. Free-standing films of LiPON are produced, exhibiting a high degree of flexibility (Figure 4.9), albeit brittle in tension. Finally, the lack of long-term connectivity with the presence of mobile cations will undoubtedly promote time-dependent mechanical behavior, to be explored in future work.
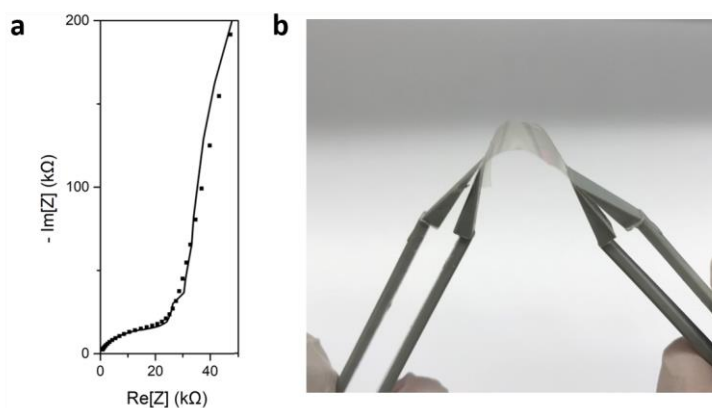
Figure 4.9. A free-standing LiPON film exhibits (a) an ionic conductivity consistent with its substrate-bound counterpart and (b) shows a remarkably compliant behavior.

4.3 Conclusion

Using 1D and 2D solid-state NMR methodologies, the local structure of amorphous LiPON is resolved, showing the prevalence of Q^0 tetrahedra and identifying the substitution of O for N_a and N_b sites. GIPAW methodologies permit calculation of a range of phosphate-based compounds, clearly identifying trends in chemical shift anisotropy as a function of composition. Fitting of chemical shift anisotropy parameters of LiPON are determined by combining AIMD to amorphize of LiPON and GIPAW methodologies for calculation of the electronic shielding associated with chemical shifts observed in NMR. The high stability of LiPON is described structurally as a combination of the low connectivity of the structure as well as the hyperannealing that occurs with physical vapor deposition. Free-standing films of LiPON are produced, exhibiting a high degree

of flexibility, and hence compliance, which further supports the lack of long-range order and questions the role of mechanical properties in the cyclability of LiPON.

Chapter 5. Cryogenic focused ion beam characterization

Cryogenic electron microscopy (cryo-EM) has recently been extended from its traditional role for visualizing structural biomolecules,[99] and has demonstrated the ability to preserve beam-sensitive alkali metals as well. This is particularly relevant as the Li-metal anode has been the focus of intense study, though interference from beam damage effects has proven troublesome. By using liquid nitrogen, samples may be held at -170dC during imaging, showing remarkable stabilization compared to room temperature. This was recently demonstrated recently through analysis of the impact of additives on the morphological growth of the solid electrolyte interphase (SEI) as well as the chemical composition of the SEIs.[100,101] However, these techniques have yet to be implemented in solid-state interfaces.
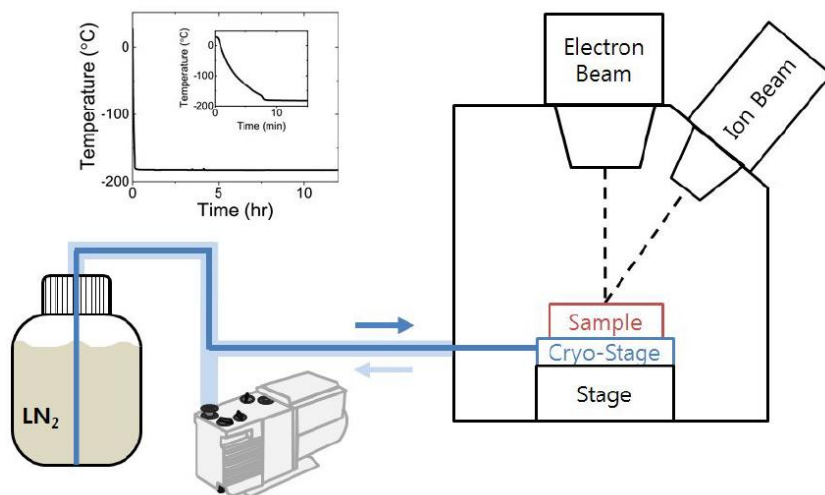
Figure 5.1. Schematic of the cryogenic focused ion beam shows cooling of the stage occurs through the flow of a chilled nitrogen gas.[102]

Application of the FIB has proven essential in the analysis of buried interfaces. Similarly to the case of cryo-TEM, cryogenic FIB (cryo-FIB, shown schematically in Figure 5.1) has been employed in the biological field for sectioning and maintaining biological samples under liquid nitrogen temperature from preparation to observation within the TEM. Interestingly, during

milling pristine Li metal foils were shown to form porous structures while heavily oxidizing and reacting with gallium ions used to mill the material. This is assumed to be from a combination of alloying reactions, high degrees of implantation due to the low density of Li metal, and evaporation of Li due to its low vapor pressure.[44] Reduction in beam voltage produces conditions insufficient for sputtering relative to the rate of redeposition. Application of cryo-FIB showed the preservation of the pristine Li metal as well as the reduction in implantation of Ga and oxidation of Li during milling (Figure 5.2).
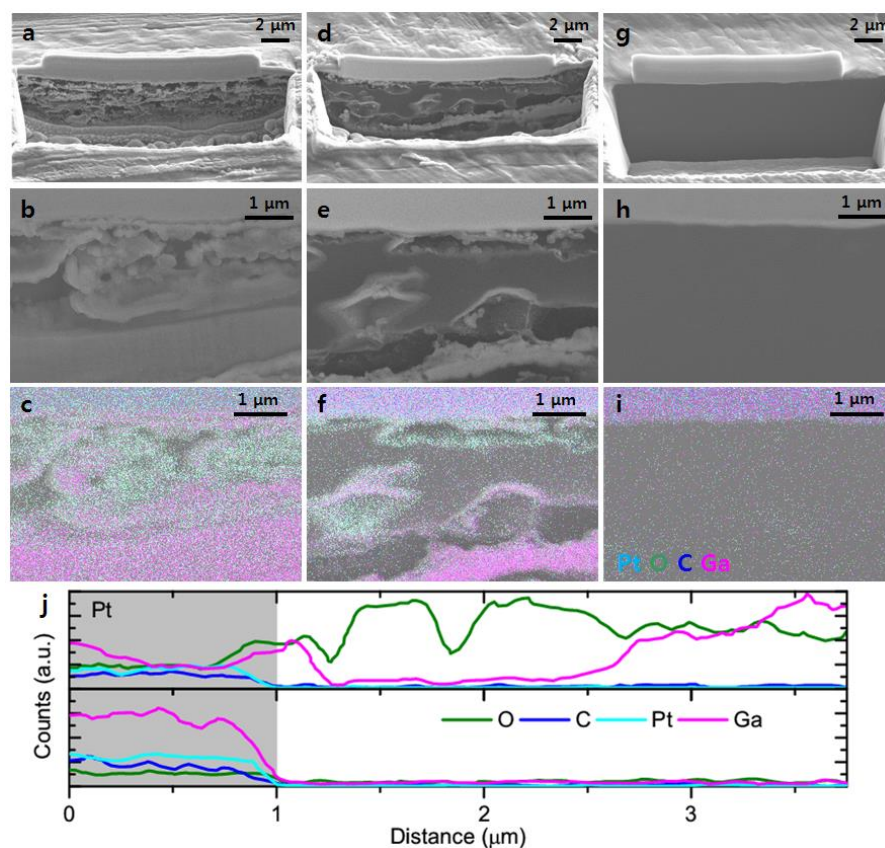
Figure 5.2. Scanning electron microscopy (SEM) images and energy dispersive spectroscopy (EDS) elemental mapping of cross-sections of commercial Li metal foil (a-c) cross-sectioned and cleaned at room temperature, (d-f) cross-sectioned at room temperature and cleaned at cryogenic temperature, and (g-i) cross-sectioned and cleaned at cryogenic temperature. (j) Quantitative elemental line scans through room temperature (top) and cryogenic temperature (bottom) cross-sections.[102]

Further, cryo-FIB may be used to explore the morphology of sensitive materials. In the case of plated Li metal, morphology was explored as a function of electrolyte, showing a strong impact on high concentration electrolytes on the plating density. To quantify the density and morphological features, slice-and-view was performed, shown schematically in Figure 5.3. Slice-and-view, coupled with cryo-FIB, provides data capable of being reconstructed into three-dimensional datasets and permits volumetric reconstruction which can provide further quantification. We use this technique in the following section to elucidate causes of premature capacity fade in a NCA/PEO composite.
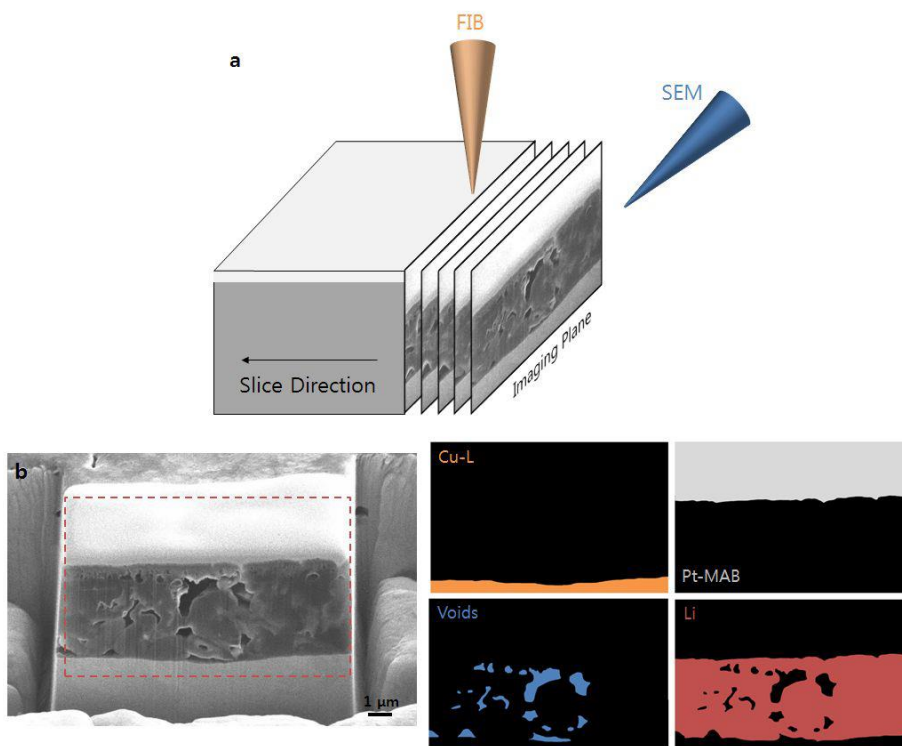
Figure 5.3. Schematic of the slice and view process, showing the process of serial slicing prior to three-dimensional reconstruction.[102]

5.1 Cryogenic characterization of composite PEO/NCA electrodes

5.1.1 Introduction

Lithium ion batteries are ubiquitous modern society, powering a handheld device revolution, promising emission-free electric vehicles, and providing hope for the implementation of an increased reliance on renewable energy for grid supply. Market-driven need for improved energy and power density has consequently increased safety concerns in modern devices. Solid-state electrolytes have been looked to as a solution to improve energy density by enabling lithium metal anodes while simultaneous improving safety through the removal of liquid carbonate electrolytes. One such variety of solid-state electrolytes, polymer electrolytes have exhibited stability against lithium metal anodes at reasonably high voltage, with the general drawback of a somewhat low ionic conductivity. However, manufacturers have indeed produced automobiles capable of running on lithium-metal/solid-polymer electrolytes at elevated temperatures. Such polymer electrolytes are produced by dissolving a lithium salt within a polymeric matrix, either crystalline or amorphous. Polyethylene oxide (PEO) is a polymer electrolyte known for its stability against Li metal, good solubility with conductive Li salts, and low T_g.[103] Further, PEO has been shown to conduct cations in its crystalline state, enhancing mechanical rigidity.[104]

Positive electrodes are incorporated into solid electrolytes in a variety of methods. Thin film batteries utilize thin, fully dense electrodes, maximizing connectivity with a planar solid electrolyte.[105] More commonly, large scale SSBs place cathode particles within a matrix of solid electrolyte and conductive binder to enhance the accessible surface area. Despite their advantages, integration of SSEs has been hindered by issues of chemical compatibility as well as a variety of electro-chemo-mechanical issues such as strain evolution.[106] Full surface coverage is essential and

71

is easily accommodated by liquid counterparts, which have the advantage of penetrating cracks within cathode particles, assuring the potential to access all surfaces of the cathode particles.

Here, we investigate potential sources of capacity fade in a PEO/NCA composite cathode. Utilizing cryogenic electron microscopy techniques including cryogenic focused ion beam (cryo-FIB) and cryogenic transmission electron microscopy (TEM), we demonstrate the high susceptibility of crystalline PEO to damage and amorphization via FIB, clearly differentiating decomposed PEO held at high state of charge from Ga-ion beam-induce damage. Cryo-EM is shown to preserve the solid polymer electrolyte, permitting quantifiable analyses of three-dimensional cross-sections of the composite. Non-uniform coverage shows catastrophic failure of the cathode particles, causing large amounts of intergranular and intragranular cracking. High-voltage storage causes notable decomposition of the electrolyte, exacerbating the non-uniform coverage of the cathode particles.

5.1.2 Methodologies

Cryogenic focused ion beam characterization is performed using an FEI DualBeam Scios equipped with a Ga ion beam. Cross-sectional preparation was performed at 30kV with currents ranging from 3 nA to 10 pA. Liquid nitrogen chills nitrogen gas which is flowed to the sample stage, reducing the temperature of the sample to -170 °C. Slice and view was performed on cross-sectional areas 30 μm wide, deep enough to image the thickness of the electrode, and slice thicknesses of 100 nm. Slices were cut at 30kV and 3nA, and phase contrast could be achieved without further cleaning. However, TEM lamella preparation required reduced voltages and current (5kV, 8pA). TEM was performed on a JEOL 2100F TEM and JEOL 2800 scanning transmission electron microscopy (STEM). Imaging was performed with a beam voltage of 200kV.

5.1.3 Cryogenic preservation of PEO crystallinity

To address concern in the solid state, cathode particles are often mixed with solid electrolytes and conductive carbon to promote uniform coating of the particles. This strategy is essential to maximize electrode kinetics, as solid-state ion conductors generally have higher ionic conductivities than cathodes. Limited surface coverage would result in bottlenecks for Li migration. While this strategy has proven effective in highly formable compounds, as in sulfide electrolytes, more rigid matrices such as polymers require in situ synthesis methods, synthesizing the polymer around cathode particles. We employ cryogenic electron microscopy techniques to preserve the structure and morphology of a polymer composite cathode and enable accurate quantification of the surfaces and interfaces within. Analysis of the cathode composites are performed in three states: (a) pristine, (b) discharged, and (c) charged states.

Composites were first analyzed via SEM and EDS, permitting clear differentiation of the cathode particles from the PEO matrix by the presence of Ni. Initial observations of the disassembled cells show a degree of delamination associated with those cells held at high state of charge, providing the first evidence of reduced cohesion to the current collector, clear through secondary electron imaging (Figure 5.4). Here we clearly observe variation between the pristine and cycled composite electrodes. In the case of the cycled electrode, some degree of electrode is removed during cell disassembly, though in the case of the cell disassembled in the charged state, a high degree of electrode removal is observed. As will be seen from three-dimensional analyses via FIB, this is likely due to the reduced contact area of the PEO matrix to the current collector.
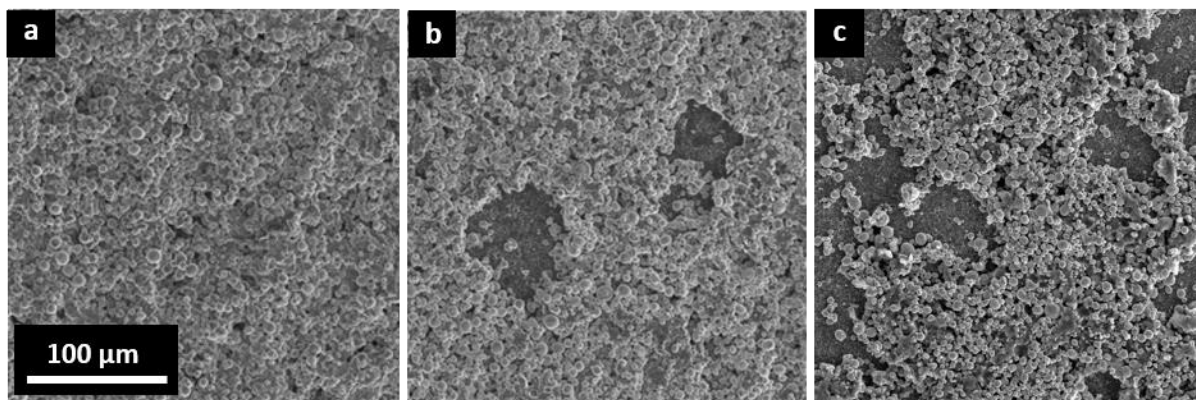
Figure 5.4. Secondary electron SEM images of (a) a pristine composite cathode, (b) a cycled cathode in the in the discharged state, and (c) a cycled cathode held in the charged state.

To determine the depth of this reduced connectivity, and associated it with morphological evolution, cross-sectional analyses are performed using a focused ion beam. In the biology field, it is well-known that beam-damage may induce degradation of samples. We have recently demonstrated this to be similarly the case in alkali metals, where interaction with the gallium beam under vacuum was shown to cause melting, oxidation, and Ga implantation, severely impacting the morphology of the cathodes. To explore the potential susceptibility of PEO to beam damage, we perform room temperature and cryogenic FIB preparation of TEM lamella. Room temperature milling clearly shows degradation of the PEO, manifest as a high degree of porosity induced during preparation (Figure 5.5). This degree of degradation suggests the Ga$^+$ beam is inducing degradation
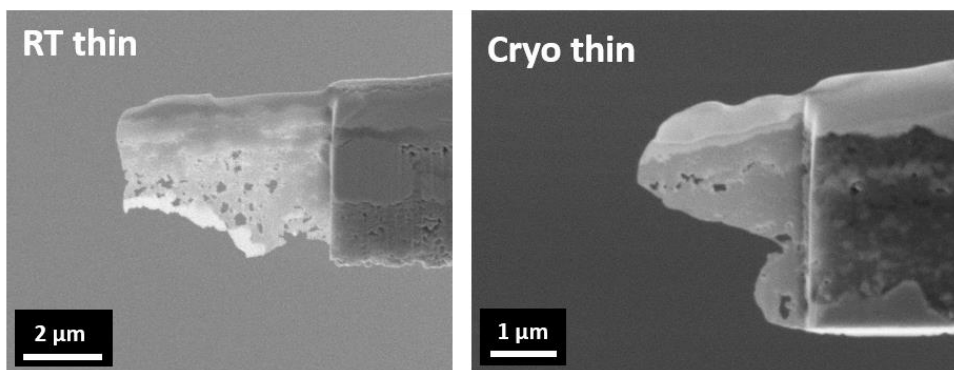
Figure 5.5. Room temperature thinning (left) shows the formation of a large number of pores in the bulk of the PEO, while cryogenic thinning (right) shows PEO bulk to exhibit low porosity.

to the PEO itself as well as the potential to induce morphological change. High resolution TEM (HRTEM) confirms that the degree of damage creates further disorder in the solid. PEO prepared at room temperature shows a complete lack of crystallinity, where that prepared by cryo-FIB distinctly shows the preservation of the crystallinity of PEO (Figure 5.6).
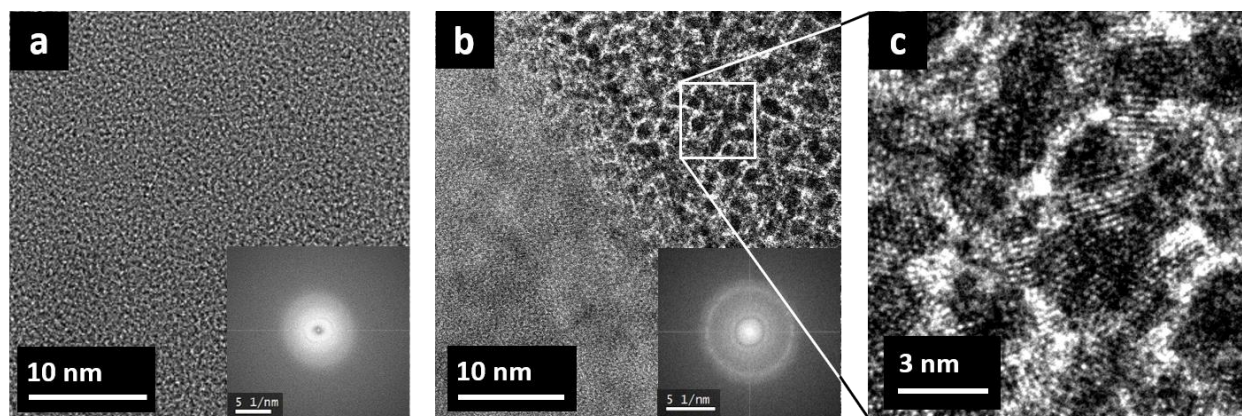
Figure 5.6. TEM analysis of a FIB lamella prepared at room temperature (a) shows complete amorphization of crystalline PEO during thinning. Preparation of FIB lamella at cryogenic temperatures (b,c) show the preservation of the crystalline structure.

5.1.4 Three-dimensional characterization of PEO/NCA composite cathodes

To explore of the sources of the rapid capacity fade associated with the composite cathodes, we perform cross-sectional analyses coupled with three-dimensional techniques to quantify the surfaces and interfaces within the composite cathodes. Initial imaging is performed using cryo-FIB cross-sections of the composite, to prevent morphological evolution, shown in Figure 5.7. Past work applying broad-area ion milling on similar NCA/PEO samples clearly showed preparation-induced decomposition.[107] The first notable observation is the incomplete coverage of the NCA particles by the PEO matrix. Implications of this incomplete coverage will be discussed further. More notably, samples charged and held at high state of charge are observed to decompose. This is apparent both within the PEO matrix, and through a decreased interfacial contact to the NCA

particles. Decomposition of the PEO is also observed in the bulk, through finer porosity. These fine pores also manifest at the interface between the PEO and current collector.
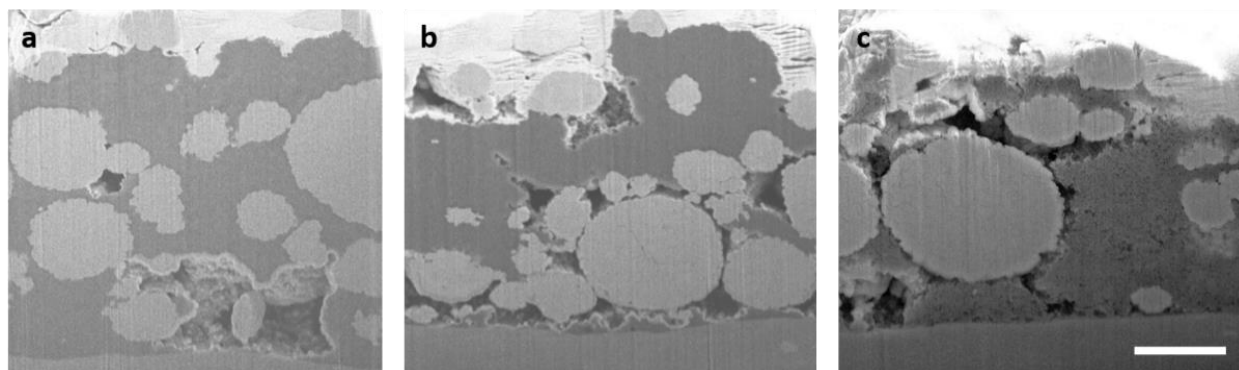
Figure 5.7 Cryo-FIB cross-sections of NCA/PEO composites in the (a) pristine state, (b) discharged state, and (c) stored in the charged state. Scale bar is 5 µm.

While clear through qualitative analysis, three-dimensional datasets are required for improved statistics and morphological understandings of the distribution of particles and void space. Three-dimensional datasets are acquired using Slice-and-View software, creating an image stack 30 images thick with slice thicknesses of 200 nm, totaling samples of approximately 6 µm in total thickness. Image stacks were then aligned, filtered, and segmented using Avizo software. An example of a processed dataset is shown in Figure 5.8. Segmentation and analysis of the three-dimensional datasets enable quantitative information through the thickness of the electrodes, clearly identifying trends in surface and interface evolution. It is important note the poor coverage present in the pristine samples, which may drive premature capacity fade. The pristine and discharged states show similar amounts of coverage and interfacial content both between the PEO:NCA and Void:NCA. However, the charged sample shows notably increased Void:NCA surface area, indicating that the high voltage storage is inducing decomposition of the PEO electrolyte. These results ultimately highlight the instability of the PEO at high voltage, with some

degradation observed in the discharged sample, but more pronounced in the case of that stored at high voltage.
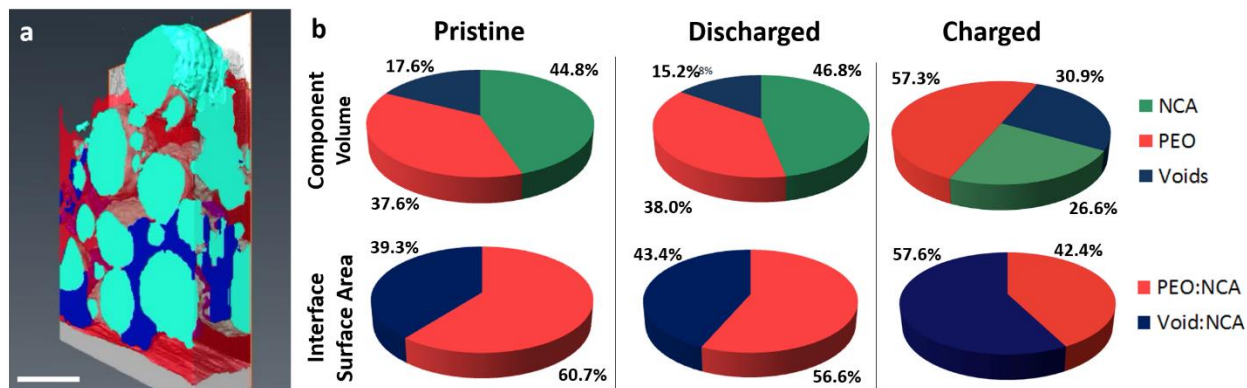
Figure 5.8. Example of 3D reconstruction from cryo-slice-and-view of a pristine NCA/PEO composite cathode (scale bar is 5 µm); and (b) statistical distribution of relative phases shows a large increase in the void fraction and subsequently decreased surface contact between PEO and NCA particles due to PEO decomposition.

5.1.4 Structural characterization of NCA via TEM

While the rapid degradation of the PEO is likely responsible for the cycling failure of the NCA, we need to observe the NCA cathode material to determine how these effects manifest on the cathode material. Through the preparation of many secondary particles, we observe no structural changes present in the NCA, regardless of its proximity to the PEO. This can be clearly seen via fast Fourier transforms (FFTs) of high resolution TEM (HRTEM) imaging in Figure 5.9.

Strikingly, large particle cracking can be observed, even with the FIB cross-sections imaged by SEM (Figure 5.10a). A closer look via HRTEM will show that this cracking takes two forms, present both at primary particle boundaries as well as within the primary particles themselves, suggesting the presence of significant amounts of strain accumulation. This level of cracking would not be expected in the early cycling during liquid electrolyte and is clearly due to effects of cycling within the PEO composite. There is some debate whether cracking of secondary particles is beneficial or not, permitting liquid electrolyte access deep within secondary particles,
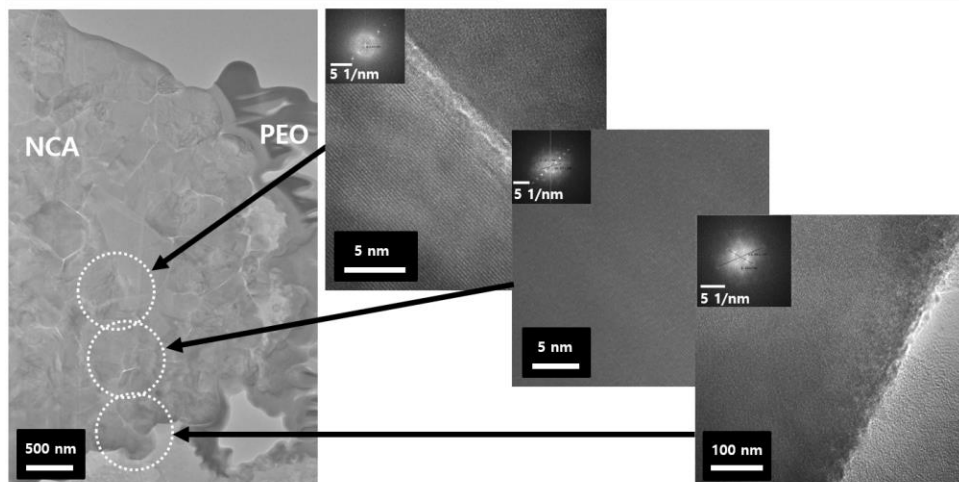
Figure 5.9. High resolution bright field TEM images of a secondary particle of NCA shows no structural variation through its thickness.

which would enhance kinetics of delithiation of the cathode material as the liquid electrolyte ionic conductivity exceeds that of the cathode particles. However, cracking in the case of SSE matrices undoubtedly reduces the accessibility of lithium within the secondary particles, which may in part be the source of the cracking: with limited pathways due to the uneven coverage of the particles, lithium may experience bottlenecks causing lithiation gradients to occur within particles. This has been observed spectrally via the Ni redox state in scanning transmission x-ray microscopy (STXM) showing clear nonuniformity through the particles.[107]
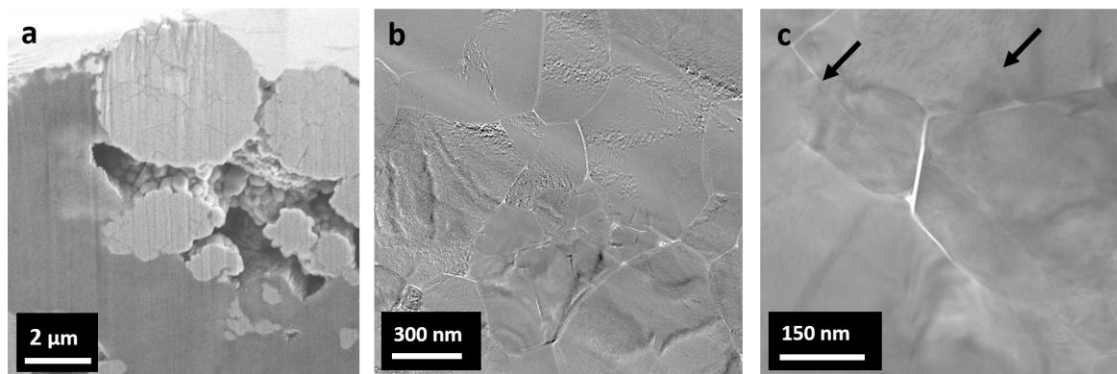
Figure 5.10. Interparticle cracking is observed in secondary particles of NCA via (a) FIB and (b) TEM. TEM also shows instances of intraparticle cracking of in cycled particles (c).

5.1.4 Summary and conclusion

Cryo-FIB was used to cross-section composite NCA/PEO electrodes for solid-state batteries. Cryo-FIB was demonstrated to prevent beam-induced decomposition as well as prevent amorphization due to local beam damage, as determined by HRTEM. Cross-sectional analysis also showed that the pristine electrode exhibited low particle coverage. Using three-dimensional slice-and-view techniques coupled with cryogenic temperatures, full reconstructions of the particles were made, permitting statistical analyses of particle coverage, electrode coverage, and void fractions. Samples held at high state of charge show PEO readily decomposes, further reducing particle coverage and enhancing capacity fade. HRTEM shows that such nonuniform coverage seems to be responsible for extensive inter- and intra-particle gracing.

Chapter 6. In situ methodologies for solid-solid interface analysis

6.1 Current state of in situ solid-state characterization

The future of electrochemical energy storage depends on the concurrent advancement of constituent component materials and their satisfactory interaction with one another. We primarily look to (1) increase the energy and power density of electrochemical cells through increasing electrode capacity, and (2) remove the chemical energy available for release during device failure, as present in modern flammable organic liquid electrolytes used in lithium-ion batteries.[108] Solid-state electrolytes (SSEs) may satisfy both these requirements, serving as a safe replacement for their organic liquid counterparts, while potentially enabling alkali metal anodes.

However, the introduction of SSEs into full cell batteries is accompanied by other constraints, both intrinsic and extrinsic.[25] Intrinsically, though many SSEs exhibit high bulk ionic conductivity, grain boundaries may ultimately reduce the effective ionic conductivity to unusable levels, as in the case of solid oxide perovskite lithium lanthanum titanate (LLTO),[109] and may serve as regions of mechanical susceptibility, aiding lithium dendrite nucleation and penetration.[110] Extrinsically, questions of electrolyte/electrode interfacial impedance, resulting from space charge [111] and chemical and electrochemical compatibility [17,18] of solid–solid interfaces, come into play. Despite the importance of these interfaces in the functionality of next-generation solid-state devices, there are surprisingly few studies focused on characterization of their interfaces, and even fewer providing in situ and operando insights.

In the past decade there have been significant efforts in applying in situ and operando measurements to electrochemical systems, though most work is limited to liquid electrolyte systems. Development of intricate electrochemical testing cells for synchrotron end stations have enabled in situ and operando x-ray diffraction (XRD), x-ray absorption spectroscopy (XAS), and x-ray photoelectron spectroscopy (XPS).[112] In situ holders for electron microscopy have similarly

progressed, [113–116] aided by the collaborative environment established by developers of transmission electron microscopy (TEM) holders. These methods have enabled dynamic observation of the complex changes within electrode materials during electrochemical cycling and have provided a variety of insights, including the dynamics of lithiation, phase transformations, and the elusive nature of the solid-electrolyte interface (SEI) formation. Such in situ electrochemical liquid testing methods are extensively described in previous review articles. [112–116]

Attempts to observe similar processes in solid-state materials have added degrees of complexity due to their buried interfaces, often requiring the expansion of existing techniques and the development of entirely new methodologies. This perspective aims to review advanced characterization techniques applied to solid–solid interfaces, working toward in situ and operando characterization to elucidate the less-understood dynamic behavior and heterogeneous characteristics present at these interfaces.

6.1.1 Techniques to characterize buried solid-solid interfaces

Until recently, electrochemical techniques, primarily cyclic voltammetry (CV) and electrochemical impedance spectroscopy (EIS), were the main methods of characterizing buried interface resistances. These studies are prevalent in characterization of all-solid-state batteries, such as $LiCoO_2$ (LCO)/lithium phosphorus oxynitride (LiPON)/Li [117] and $LCO/Li_{1.5}Al_{0.5}Ti_{1.5}(PO_4)_3$ (LATP) [118] chemistries. Electrochemical testing of such cells suggested growing interfacial impedance, vaguely attributed to modified chemical bonding impacting charge-transfer characteristics. [117] Thermal annealing studies showed reduced interfacial resistances and improved cyclability of the LCO/LiPON/Li cells, though physical interpretation was speculative, lacking further experimental evidence and simply attributing the change to modified bonding at the LCO/LiPON interface. [117] The LCO/LATP cell utilized in situ formation

of the anode, showing low charge-transfer resistance, though the nature of the anode was unknown at the time of the electrochemical testing. [118]

Similar studies further evaluated the stability of an interface or interlayer, such as the insertion of a Nb interlayer between LCO and lithium lanthanum zirconium oxide (LLZO) electrolyte, observing reduced interfacial impedance without explicit mechanistic descriptions. [119] That is not to say that electrochemical methods are insufficient methods of probing such interfaces. In scenarios where constituents are expected to be kinetically stable, careful experimental design promotes isolation of such effects, as in the case of idealized solid-state interfaces such as some silver conductors.[120] Control of materials selection can allow electrochemical methodologies to effectively isolate sources of charge-transfer resistance to the impact of lattice mismatch, defect chemistry, and equilibrium potentials. [121] Indeed, an entire field has been based around this ideology—solid-state ionics/nanoionics—however, this will not be covered in this article to focus on adapting advanced characterization techniques to more commercially relevant systems.

Until recently, the nature of stability of solid-state interfaces in applied lithium-ion battery materials was largely unknown, and questions of compatibility at interfaces was ascribed generally to issues of charge transfer across interfaces. Density functional theory (DFT) calculations were successfully employed to predict engineered interphases to counteract the effects of space charge, uncovering lithium niobate ($LiNbO_3$) as a candidate to stabilize the cathode/sulfide–electrolyte interface.[122] The insertion of a $LiNbO_3$ interlayer at the LCO/LiPON interface was shown via XPS to modify lithium concentration, attributed to non-faradaic Li migration. [123] A following body of computational research opened the question as to the thermodynamic stability of these interfaces— a fundamentally important step in interpreting the nature of these buried interfaces, providing potential explanations for the presence of interfacial resistances at solid☐solid interfaces.[17,18,28]

This work suggests that stable solid-state interphases effectively bridge the electrochemical window in much the same way the solid–electrolyte interface (SEI) does in their liquid electrolyte counterpart.

Thermodynamically driven decomposition is most clearly shown after applying high-temperature processing methods, as in the case of spinel cathodes interfaced with LATP; here, the increased temperature drives decomposition to a degree detectable by x-ray diffraction (XRD)—intuitively ruling out high-temperature co-sintering as a processing method. [124] Combining results of electrochemical testing with ex situ evaluation has proven to be an effective technique for a more comprehensive understanding of the stability of solid–solid interfaces, and has yielded results consistent with computational predictions.

For the case of LCO/LiPON, LCO was predicted to decompose into a variety of constituents, dependent on the local bonding environment and lithiation state. [28] Experimentally, it was observed that cycling LCO/LiPON/Li thin-film batteries at elevated temperatures resulted in increasing interfacial impedance values. When extracted by a focused ion beam (FIB) system and observed by scanning transmission electron microscopy coupled with electron energy loss spectroscopy (STEM/EELS), the increased interfacial impedance was correlated with the growth of a structurally decomposed LCO interlayer, exhibiting chemical signals consistent with Li_2O and disordered rock salt Co_3O_4. [125] X-ray photoelectron spectroscopy (XPS) was similarly applied to explain growing impedance in Na-metal/Na-sulfide symmetric cells; as predicted by computational modeling, Cl-doping was observed to promote the formation of NaCl, which stabilized the interface, preventing further electrolyte decomposition. [126] Similar to the case of LCO/LiPON, DFT modeling of phase diagrams is partially correct, yet it generally fails to differentiate the kinetics of phase formation.

Though ex situ methods have proven convenient for interpreting interfacial behavior, they are ineffective for certain material classes. For example, despite the importance Li-metal anodes play in increasing energy densities of next-generation electrochemical cells, methods for structural characterization have been limited until recently. There are many reasons for this, including Li-metal's high reactivity and soft mechanical properties, forming native oxides under environments controlled to below ppm of oxygen and moisture, and its susceptibility to melting/vaporization under exposure to high-energy probes, as in FIB preparation methods. [102]

Cryogenic electron microscopy (cryo-EM), a tool commonplace to the biological field, has recently secured its place as a necessary tool in the characterization of lithium metal. With cryogenic TEM (cryo-TEM) the sample temperature is maintained low enough to counteract local heating during exposure to an electron beam. Such recent work has elucidated the amorphous nature of electrodeposited lithium under certain plating conditions,[100] demonstrating the stability of lithium while imaging at atomic resolution. [101] Similarly, recent work has shown the necessity of cryogenic temperatures during FIB milling (cryo-FIB) of alkali metals. Room-temperature melting has been shown to drastically alter lithium morphology, obscuring the nature of lithium stripping and plating, and rendering the Li-metal/SSE interface unstable. Indeed, there is further demonstration of the effectiveness of cryo-FIB in maintaining morphological features present in stripping/plating experiments under a variety of electrolytes. [102] Having demonstrated the relative importance of maintaining cryogenic temperatures while exposing lithium metal to electron beams, a next step would be to apply such cryo-EM analyses to the Li/SSE interfaces. Needless to say, this would require complete environmental isolation of the FIB-prepared sample from milling to insertion into the TEM—a markedly difficult task.

6.1.2 In situ observation of thermodynamic interface modification

Furthering the notion of thermodynamic incompatibility/decomposition, a variety of in situ observations of solid–solid interface reactions have been pursued through XPS and TEM. Utilizing high-vacuum-transfer systems, a number of researchers have taken surface-science approaches, combining surface sensitive XPS with intermittent growth of various materials to measure modification in chemical bonds as materials are grown upon one another (Figure 6.1a). Such results have been useful in characterizing the chemical bonding and intrinsic band-structure modification, as well as observing chemical decomposition at solid–solid interfaces. Examples include the deposition of Li metal on LiPON, suggesting the chemical formation of computationally predicted species (Li_2O, Li_3PO_4, and Li_3N),[19] direct observation of titanium reduction at the LLTO/Li interface,[127] and similarly the decomposition of $L_{10}GeP_2S_{12}$ into Li_3P, Li_2S, and a Li-Ge alloy upon deposition of Li;[128] these techniques have provided valuable explanations of increased interfacial impedance and validated existing thermodynamic models, though such methods lack the crucial effect of the electrochemical probe present in actual devices.

Monitoring in situ reactions within a STEM was performed using a lithium-coated probe, made to contact aluminum-doped garnet LLZO ($Li_{7-3x}Al_xLa_3Zr_2O_{12}$), shown in Figure 6.1b. STEM coupled with EELS provides the capability to characterize a material structurally, probing with atomic-scale resolution, and adds the advantage of mapping detailed chemical states. In this work, when the Li probe was brought into contact with the LLZO, a distinct chemical change was observed, showing a modified oxygen K-edge, suggesting the loss of the cubic phase, Li K-edge changes, consistent with the presence of excess Li, and Zr L-edge modification consistent with Zr reduction. Interestingly, these results do not show decomposition of the electrolyte, but rather the modification to tetragonal LLZO, a less conductive interphase, but negligibly so, given the

thickness of the interlayer.[20] The results emphasize the importance of kinetically limited reactions at these interfaces, and suggest that while more reactive materials will thermodynamically decompose in the presence of highly reducing lithium metal, certain electrolytes possess some degree of stability and will at least require external sources of energy to drive decomposition.
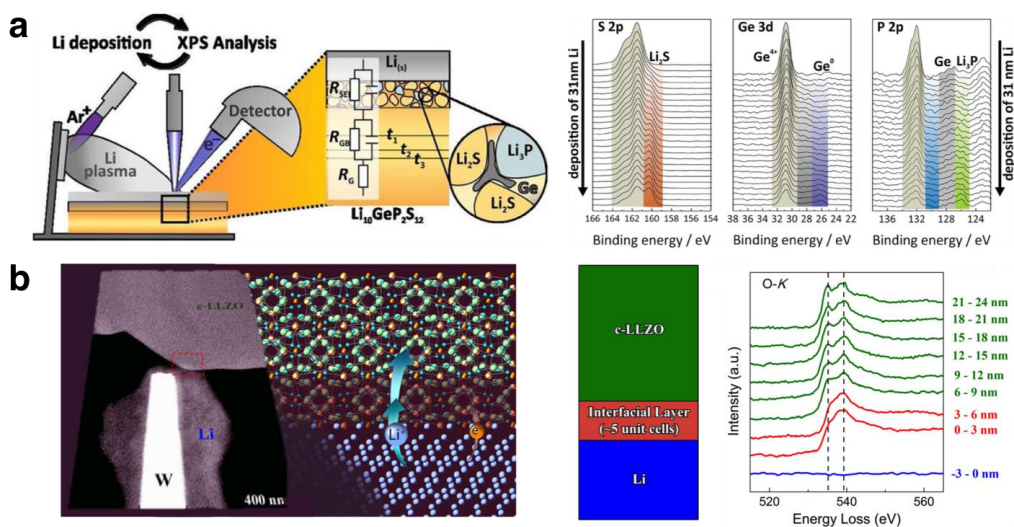
Figure 6.1. In situ techniques have been developed to characterize the thermodynamic and kinetic stability of solid-state interphases as formed in controlled environments. (a) In situ deposition of lithium upon solid electrolytes coupled with x-ray photoelectron spectroscopy has been applied to a number of systems, here showing decomposition of $L_{10}GeP_2S_{12}$ when coated with Li;[128] Adapted with permission from ref [128]. Copyright 2016 American Chemical Society. (b) physical contact between Li and solid electrolyte LLZO in a transmission electron microscope with electron energy loss spectrometer, showing fine structure modification commensurate with structural modification.[20] Adapted with permission from ref [20]. Copyright 2016 American Chemical Society.

6.1.3 In situ observation of electrochemically driven interface modification

Electrochemical in situ experiments involve the design and fabrication of electrochemically-active devices, with an ultimate goal of elucidating links between state of charge and the nature of the interface, yet very few techniques have successfully developed with this capability. The first demonstration of an electrochemically active device in TEM involved an LiCoO$_2$ cathode and Li$_{1+x+y}$Al$_y$Ti$_{2\square y}$Si$_x$P$_{3\square x}$O$_{12}$ electrolyte, forming the anode in situ during charge

(Figure 6.2a). A cross-section of the cathode/electrolyte interface was thinned via FIB, allowing a range of TEM characterization to be performed. Primary findings via electron holography allowed mapping of the electric potential as a function of state of charge. The potential distribution showed a sharp potential drop at the cathode/electrolyte interface, with linear decreases through each component. This technique was more recently applied to observe the potential distribution as a function of voltage in LiPON solid electrolyte [133]. Beyond the exposure of only one interface in the full cell device, the bulk of the device likely dominates the electrochemical performance, leaving to question the magnitude of the field distribution within the thinned region. Nevertheless, an electron-transparent region in an electrochemically-active battery was an important step in the development of TEM-based in situ techniques.
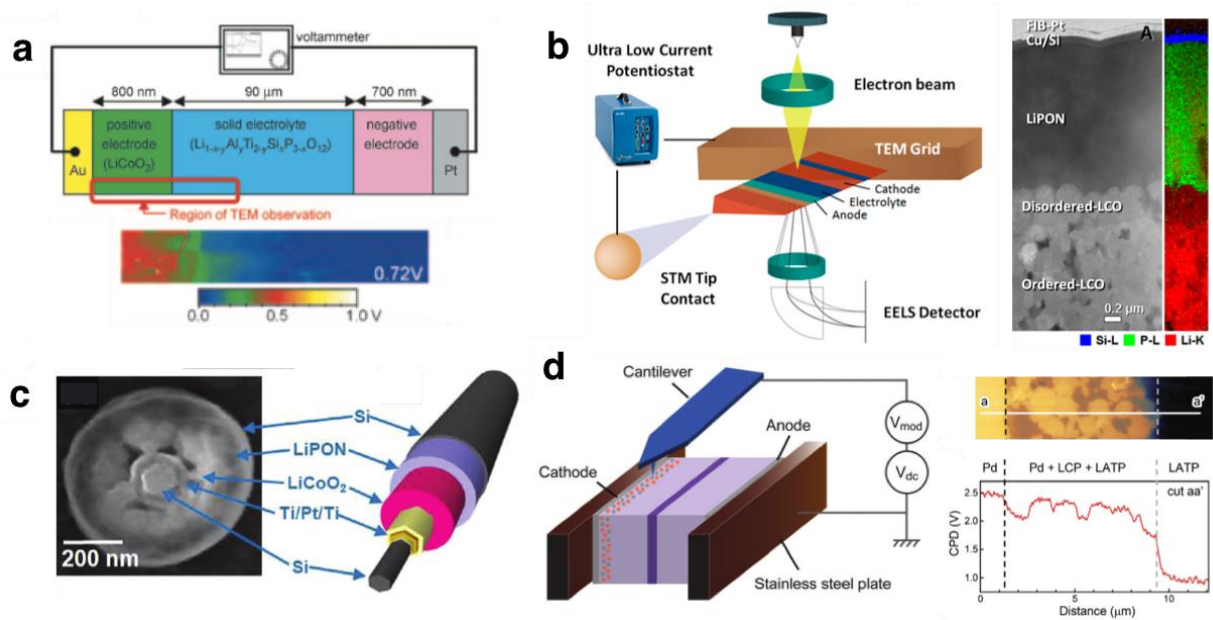
Figure 6.2. Advanced methods for local in situ interface characterization via (a) electron holography,[129] (b) STEM/EELS,[130] (c) TEM of 3D nanowire-based batteries,[131] and (d) Kelvin probe force microscopy of potential distribution across all-solid-state battery cross-sections.[132]

The first true electrochemically active nanobattery to expose all active interfaces was prepared by extracting a cross-section of a full-cell thin film battery via FIB (Figure 6.2b). Work by Santhanogopalan demonstrated electrochemical performance of a cross-section of a LCO/LiPON/amorphous-Si full cell first within the FIB, demonstrating the importance of the dwell time during preparation in preventing damage and decomposition of the LiPON solid electrolyte.[134] A similar wedge-shaped nanobattery was then transferred to a scanning tunneling microscope holder, allowing precise manipulation of an electrical contact, used for in situ biasing within the TEM. This probe, coupled with a low-current potentiostat, allowed the first demonstration of potentiostatic in situ cycling of a solid-state device in the TEM, while maintaining current densities consistent with functioning devices. Using scanning transmission electron microscopy coupled with electron energy loss spectroscopy (STEM/EELS), an interphase of decomposed LCO was observed, chemically reminiscent of a combination of Co_3O_4 and Li_2O. This work not only uncovered the interfacial phenomena responsible for the increasing charge transfer resistance at the LCO/LiPON interface, but demonstrated the importance in in situ methodologies to mitigate the effects of sample exposure to ambient conditions.[135]

An alternative design, fabricating the nanobattery in a core-shell configuration around a conductive nano-wire is shown in Figure 6.2c.[131] After isolating the electrochemically active material from the base of the nanowire, the nanowire is biased with a similar mechanically manipulated probe tip, as mentioned previously. Using this technique, it was determined that the critical component to prevent shorting is the thickness of the LiPON layer. When too thin, the layer was observed self-discharge, and via bright field TEM the electrochemically-driven formation of voids within LiPON was observed. The 3-dimensional configuration of the nanobattery makes

88

chemical evaluation of the interfaces ambiguous, though enabled explanation of the shorting phenomena in these 3D devices.

In situ Kelvin probe force microscopy (KPFM) has been employed to explore the electric potential distribution across cross-sections of solid-state batteries,[132] similar to that observed via electron holography (Figure 2d).[133] Here, a potential is measured through the scanning probe tip across the battery cross-section, effectively measuring the electrical potential distribution across the battery, and showing regions of lithium depletion.[132] This technique offers the advantage of imaging more area of larger devices than possible in TEM. Though this technique requires cross-sectioning using an ion mill with environmental isolation capabilities, along with a scanning probe within an inert environment. This work was performed on a composite electrode—one would imagine performing this similar technique on a thin film configuration may provide a more pertinent look at field distribution in parallel cells. Such a test, coupled with chemical probing of the interfaces, may allow deconvolution of space charge effects.

Other non-local efforts to characterize solid-state interfaces have been made via solid-state nuclear magnetoresonance (NMR) and magnetic resonance imaging (MRI) of Li^7 ions, as in the case of the $Li/Li_{10}GeP_2S_{12}/Li$ symmetric configuration.[136] In situ MRI provided the ability to map Li distribution through the thickness of the electrolyte as a function of state of charge, and correlated this distribution to an inhomogeneous strain state through the thickness of the electrolyte. With continuous cycling, Li distribution clearly correlates with cracking within the electrolyte.
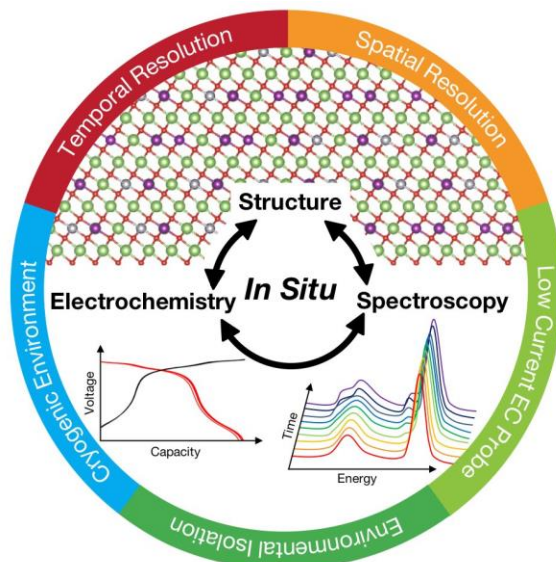
Figure 6.3. In situ probing of solid-state interfaces requires development of a range of aspects, including increasing temporal and spatial resolution, enabling low current measurements with minimal noise, environmental transfer capabilities, and application of cryogenic temperatures.

6.1.4 Remaining challenges and the future of in situ and operando techniques

While the techniques described here have effectively been employed to characterize interfaces, there is ample room for improvement, with the goal of simultaneously extracting chemical, structural, and mechanical information as a function of state of charge. It is worth noting that synchrotron x-ray methods have not played a big role in the characterization of solid-state interfaces, likely due to the complexities in data convolution in buried interfaces of complex devices. Electron microscopy at the present time is the only method capable of collecting structural and chemical information under electrochemical stimulus for solid state interfaces. Advancement of in situ and operando electron microscopy methodologies requires further development in the current state of the art, reducing beam-material interaction induced damage while improving spatial and temporal resolution during data acquisition; an ideal characterization technique would meet most of the requirements outlined in Figure 6.3.

Use of high-energy probes is accompanied by many practical considerations, primarily beam damage effects. High-energy electrons damage materials through radiolysis (decomposition due to ionizing radiation), primary knock-on damage, and local heating effects.[41] Solid electrolytes are electronically insulating out of necessity and are often amorphous, and as such are generally susceptible to thermally degradation. Traditional methods of combating heating effects, such as carbon coating, are incompatible with in situ biasing (i.e., device shorting), but rather require fine control of the experimental design by limiting electron dose and selecting more robust electrolytes. It is noted in works of Santhanagopalan [135] and Wang, [130] and similarly by the community of electron microscopists, [114] that the electron dose is of critical importance both for the stability of the materials being probed and in the interpretation of electronic probe outputs, and should be recorded and reported carefully. Selection of electrolytes that are more robust to beam exposure, such as oxides LLTO or LLZO, will enable quantitative observation of dynamic cathodic/anodic behaviors.

Beyond damaging effects, electron probes also have the potential to alter the total current injected into the battery. Revisiting the length scale of nanobatteries, the necessarily small cross section required for TEM analysis demands similarly low currents to promote reasonable electrochemical behavior. For example, a dense $LiCoO_2$ nanobattery with a cross section of 10 μm^2 and cathode thickness of 2 μm demands a current on the order of 10 pA to achieve a cycling rate of 1 C, though lower charge rates are required for systems with sluggish kinetics or large interfacial transfer impedance. While this current may be on the order of magnitude of STEM probe currents, the likelihood of the electron probe interacting with the electrochemical probe is minimal due to the low degree of internal scattering; however, the degree of scattering is dependent on the material density and the sample geometry. Currents below the pA range may be impacted

by electromagnetic noise within instruments, and reduced current testing within a TEM is currently being evaluated.

Improved detector acquisition rates have the potential to capture reconstruction in solid-state interphases, as in the case of atomically resolved grain-boundary dynamics reconstructions.[137] Direct-detection cameras have further enabled reduced-dose image acquisition, as effectively demonstrated in biological sciences,[138] and will likely be useful in capturing dynamic phenomena in sensitive battery materials. However, such high-speed comes with the downside of yielding overwhelmingly large data sets. Direct detection cameras capable of capturing 24 megapixel images at a rate of 1500 frames per s, producing datasets on the order of terabytes, are nearing the limit of modern hard drive technology. Efficient storage protocol and automated large-data set analysis methods are areas of great interest to the field.

When characterizing nanoscale devices, it behooves the researcher to keep a realistic picture of the nature of the modifications to their device. For example, the reduced in-plane length scale of a nanobattery used in the in situ TEM methodologies is notably different from that of its parent device. Fabrication of the nanobattery increases the edge/interface ratio otherwise negligible in a thin-film device. Arguments as to field distribution should incorporate models with geometric considerations, as free surfaces likely alter the equilibrium field distribution through the bulk of the nanobattery.[108] Similarly, kinetic limitations of the electrodes place an upper bound on the applied current densities. Analogous to alkali metal ions' propensity to form dendrites in liquid cells, the presence of an exposed interface may provide a low energy site for nucleation should the conditions present themselves, ultimately resulting in "dead" metal extruding outside of the device; such material may be rendered largely inactive due to its position outside of the electric field potential. Attempts to bypass the complexities associated with full cell devices include an FIB-

assembled nanobattery, with an FIB-thinned LiCoO2 particle as the cathode, FIB lamella of LLZO as electrolyte, and Au anode, all affixed together using FIB-deposited Pt.[139] While such fabrication methods may provide insight into the dynamic nature of cathode materials under extreme conditions, such construction requires careful evaluation of the input current to make any link between the electrochemical state of a device and the phenomena being observed. In such work, with a cross section required to achieve atomic-scale resolution via conventional TEM, structural change was observed with the application of current on the order of 1 mA;[139] considering the size of the cross section for imaging, this translates to a current density on the order of 10^8 mA/cm^2— in excess of current densities present in conventional devices. Such approximations are necessary, and as long as they are addressed appropriately, they do not limit the impact of the results presented.

Further, studying electrochemical evolution of alkali-metal anodes will in itself require a host of engineering accommodations. Environmental isolation is paramount in the case of alkali metal anode-based batteries, as the reduced dimensions greatly increase the surface-to-volume ratio. Even if environmental isolation can be accomplished, there is the question of stability under the electron beam, which has been demonstrated to be mitigated by cryo-EM techniques. Finally, to apply electrochemical methods requires the in situ biasing capabilities demonstrated in past work.

However, one may note an inherent incompatibility between cryogenic temperatures and the reduced kinetics of interfacial decomposition at reduced temperatures. While cryo-EM has proven to be very useful, further work is needed to study variability in holder temperature with respect to lithium stability under the electron beam. A researcher could imagine tuning temperatures for (1) lithium/interface stability, (2) interface kinetics, and (3) lithium transport

within the device. Conversely, in situ heating holders, coupled with in situ biasing holders, would promote thermodynamic decomposition, emulating the effect of cycling batteries at elevated temperatures.

6.1.5 Summary and Outlook

In spite of fundamental limitations, the outlined techniques are currently the only methodologies capable of locally probing buried solid-state interfaces, enabling simultaneous structural and chemical characterization as a function of state of charge. The most striking aspect of the development of solid-state electrolytes, as evident from this analysis or from a similar literature search, is the limited number of studies devoted to explaining poor materials compatibility. Understandably, the degree of incompatibility was only recently called into question in the host of DFT studies, and similarly due to the complexity of analysis of these systems. Even in the limit of ex situ analyses, these materials are inherently reactive under ambient conditions, often shrouding the true electrochemical modifications present. And while thermodynamic stability is in question in many compounds, kinetics of decomposition serves as a further variable, likely resulting in discrepancy between theory and experiment. Only through the application of in situ methodologies, can we capture the dynamic chemical nature of interfaces, preventing environmental effects from taking hold, and further preventing electrochemical relaxation when the device is removed from a circuit.

6.2 Protocol for the fabrication of electrochemically active solid-state nanobatteries

Solid-state electrolytes are a promising replacement for current organic liquid electrolytes, enabling higher energy densities and improved safety of lithium-ion (Li-ion) batteries. However, a number of setbacks prevent their integration into commercial devices. The main limiting factor is due to nanoscale phenomena occurring at the electrode/electrolyte interfaces, ultimately leading to degradation of battery operation. These key problems are highly challenging to observe and characterize as these batteries contain multiple buried interfaces. One approach for direct observation of interfacial phenomena in thin film batteries is through the fabrication of electrochemically active nanobatteries by focused ion beam (FIB). As such, a reliable technique to fabricate nanobatteries was developed and demonstrated in recent work. Herein, a detailed protocol with the step-by-step process is presented to enable the reproduction of the nanobattery fabrication process.

6.2.1 Introduction

Focused ion beams (FIB) have been used chiefly for transmission electron microscopy (TEM) specimen preparation and circuit editing.[44,140] Nanofabrication using FIB has progressed significantly during the last two decades with much focus on semiconductor materials.[141] Major concerns with FIB techniques have been surface damage, re-deposition and preferential sputtering due to high current density.[142,143] There have been several articles on the FIB damage of bulk materials during preparation of TEM specimens and possible methods to reduce this damage have been proposed.[144–147] However, FIB fabrication of active devices that consist multilayers with different functionality are still limited. For solid-state devices, especially in the field of energy storage, interfaces play a crucial role, and the solid-solid interface is most often seen as a dominant source of impedance.[125] These interfaces are particularly difficult to characterize, due to a

combination of their buried nature and data convolution in the presence of multiple interfaces in a single device. The fabrication of all-solid-state nanobatteries is critical to probe and understand the dynamic nature of these interfaces, ultimately impacting the electrochemical processes in batteries. Thin film batteries based on lithium phosphorous oxynitride (LiPON) have been demonstrated more than two decades ago.[148] FIB fabrication of electrochemically active nanobatteries from a thin film battery is critical for enabling in situ evaluation of interfaces. However, most attempts to fabricate nanobatteries using FIB fail to retain the electrochemical activity due to short-circuiting. Initial attempts at in situ cycling thinned only a small portion of the nanobattery, to observe the lithium distribution by electron holography.[133] More recent work has demonstrated the successful FIB fabrication of electrochemically active nanobatteries, which enabled both ex situ and in situ STEM/EELS characterization of interfacial phenomenon.[130,135] Important FIB fabrication parameters that help to retain the electrochemical activity have been indicated in ref. [135], and a further detailed protocol is presented in this manuscript. This procedure is based on a $LiCoO_2$/LiPON/a-Si battery, but will ultimately enable exploration of further thin film battery chemistries.

6.2.2 Protocol for fabrication of a nanobattery

Thin film battery deposition (mostly using physical vapor deposition techniques) is not described as part of this work, though the components of the complete battery used in this study are described below. Details of the complete thin film battery deposition process may be found in the literature.[149,150] A complete thin film battery consists of, a gold current collector, typically 100 – 150 nm in thickness, on an Al_2O_3 substrate; a cathode (in the present work, approximately 2 µm thick $LiCoO_2$) is deposited on top of the gold current collector using a physical mask, to leave gold exposed for making electrical contact; a LiPON solid-electrolyte (of 1 – 1.5 µm thickness) is

deposited with a profile larger than the cathode, to prevent shorting; an anode is deposited (in the present case amorphous silicon of about 80 nm in thickness) with an area roughly the same as the cathode; and a thin-film copper current collector. The thin film battery is mounted on to a SEM stub made of aluminum, and use colloidal silver paste to connect the cathode current collector. Prior to pumping down the chamber, it is necessary to ensure a proper electrical pathway exists between the copper grid, which the nanobattery will be mounted to and will serve as the conductive pathway to the cathode, shown in Figure 6.4. Depending on the grounding of the instrument's stage, this may be performed by connecting the cathode connection of the potentiostat to the stage grounding. It is important to note that this may disable touch alarm capability of the instrument, and should only be done when no further tilting of the stage is necessary. Alternatively, cathode may be accessed by through an electrical vacuum feedthrough. Similarly, ensure a conductive pathway from the micromanipulator tip to the outside of the probe's module exists. A connection to a common micromanipulator equipped on commercial FIB's (Omni-probe^{TM}) is shown in Figure 6.4b.
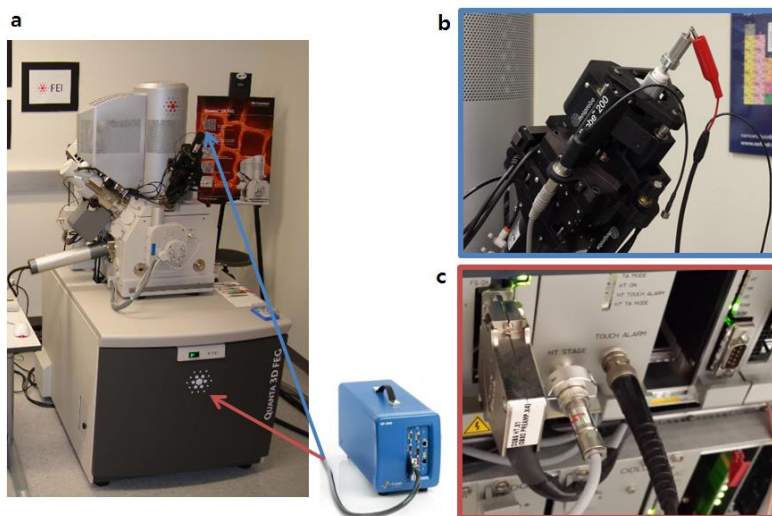
Figure 6.4. (a) External electrical connections to the potentiostat (b) to the anode through the micromanipulator and (c) to the cathode through the instrument's stage.

A Pt protective layer is depositited 1.5 to 2 µm thick using an ion beam with a current of around 0.3 nA and dwell time of 200 ns over an area of 25 x 2 µm^2 on the copper current collector of the thin-film battery. A cross-sectional FIB milling option is then used to isolate the nanobattery by FIB milling around the Pt-deposit. The milling current should be ≤ 2.8 nA and dwell time = 100 ns. The depth of milling and area of milling depends on thickness of the thin film battery stack. In the present case, the depth of milling was fixed to 7-8 µm, as the total thickness of the stack was less than 5 µm. Use a cross-section cleaning procedure with an ion beam current ≤ 0.3 nA and dwell time of 100 ns. The depth of milling is sufficient when the Al$_2$O$_3$ substrate below the gold current collector is exposed. Perform the under-cuts at a stage tilt of 0 degrees, beam current ≤ 2.8 nA, and a dwell time of 100 ns to completely isolate the nanobattery and lift out using the typical Micromanipulator lift out procedure (Figure 6.5).[140] Longer cross-section allows fabricating multiple nanobatteries in a single liftout.
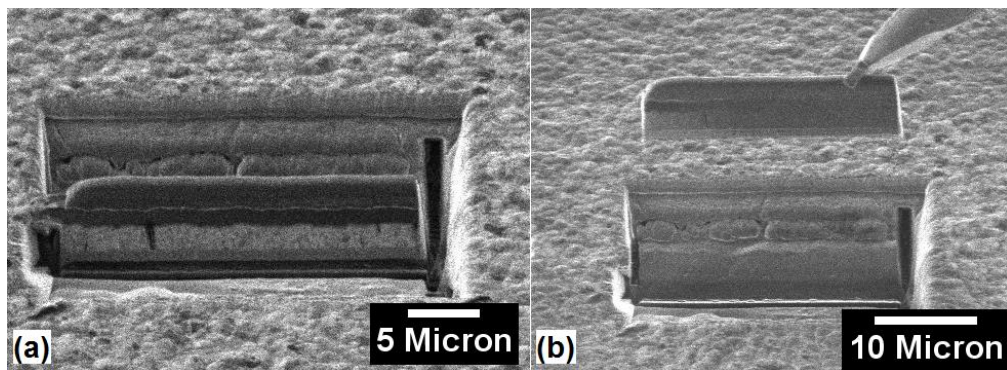
Figure 6.5. FIB image of (a) isolated cross-section with under-cut and (b) liftout of the isolated cross-section.

The Micromanipulator grid mounted nanobattery section needs further processing to enable electrochemical activity, since the as-mounted nanobattery is covered with re-deposited layer due to lift-out procedure and without any electrical contact to the current collectors. Both electron and ion beam imaging should be minimized. Whenever required, imaging is performed

with electrons at low pixel dwell times and with the ion beams at lower beam current (usually in pA) and low dwell time (100 ns). Most of the time, high dwell time electron beam imaging produce visible changes on the LiPON electrolyte. The re-deposited insulating layer on grid-mounted nanobattery section must be removed to expose the electrochemically active core of the nanobattery. Use a cross-sectional cleaning procedure in the FIB software to remove re-deposited material over a 5 μm wide section of the nanobattery near the Cu grid that leads to a clear image of all the layers of the nanobattery (Figure 6.6a).
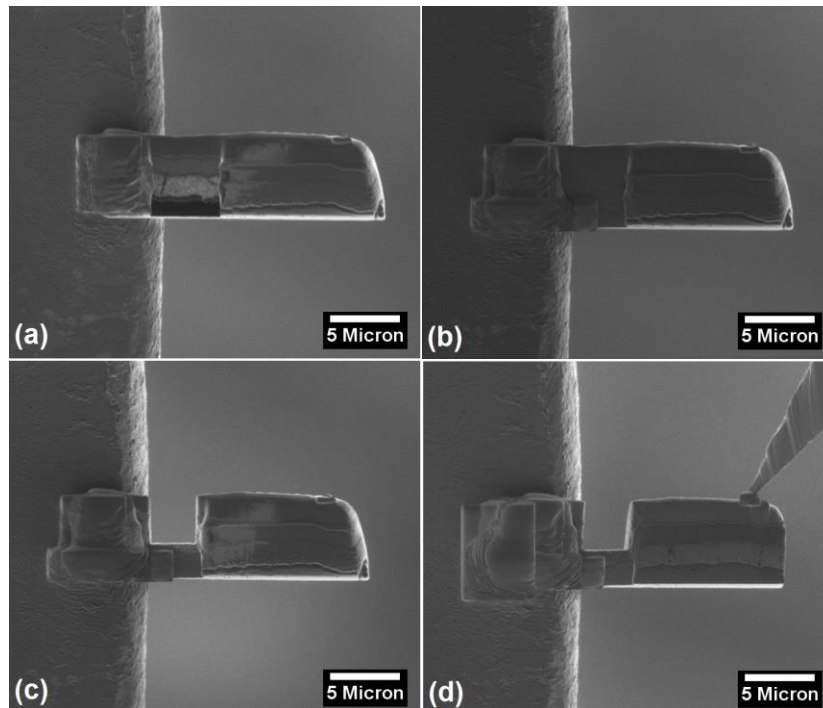
Figure 6.6. FIB images of (a) cleaning the part of the nanobattery cross-section (b) contact grid and cathode current collector by platinum deposition (c) cut to isolate anode from shorting due to platinum deposition (d) cleaning cross-section (both front and back side of the view presented) and contact anode using Micromanipulator for biasing.

Use the FIB-Pt deposition to create an electrical contact between the cathode current collector and the metallic grid (Figure 6.6b). Make a vertical rectangle cut to isolate the anode from the Cu grid and consequently the cathode (Figure 6.6c). It is noted that the re-deposition

during anode isolation and FIB-Pt deposition covers across the layers of the nanobattery, and the cross-section cleaning procedure is used to remove this re-deposited layer until all the individual layers are distinctly visible as shown in Figure 6.6d. Afterwards the micromanipulator is inserted and used for making contact with anode with the FIB-Pt deposition.

The micromanipulator is in contact to the anode, while the cathode is connected to the stage through the grid for electrochemical cycling without exposing the nanobattery to atmospheric conditions (i.e. without breaking the FIB chamber vacuum). Make the external connections with the low-current potentiostat as shown in Figure 6.4. Once the micromanipulator needle is connected to the nanobattery, minimize contact with the FIB as any vibration can destroy the nanobattery. Electrochemical cycling parameters will depend on the cross-sectional area nanobattery.

6.2.5 Representative results.

A representative solid-state Li-ion nanobattery fabrication process is described step-by-step in the protocol. Figure 6.7 shows in situ testing of electrochemical charging profiles of two cells that were fabricated. Both the profiles clearly show a 3.6 V plateau corresponding to $LiCoO_2$-Si full cell chemistry and oxidation of $Co^{3+} \rightarrow Co^{4+}$. Cell-1 (Figure 6.7a) was tested at lower current density (50 $\mu A/cm^2$) limiting the charge capacity to 12.5 $\mu Ah/cm^2$. Cell-2 (Figure 6.7b) presents charging profile at higher current density 1.25 mA/cm^2 that was limited by the upper cut-off voltage of 4.2 V. The capacity recorded was about 105 $\mu Ah/cm^2$, close to the theoretical capacity of the Cell-2 (110 ~ 120 $\mu Ah/cm^2$). The first discharge capacity of the nanobatteries has been poor while the subsequent cycle capacities (both charge and discharge) were limited due to the first cycle irreversibility. The discharge process of nanobatteries is still under optimization and hence not presented here.
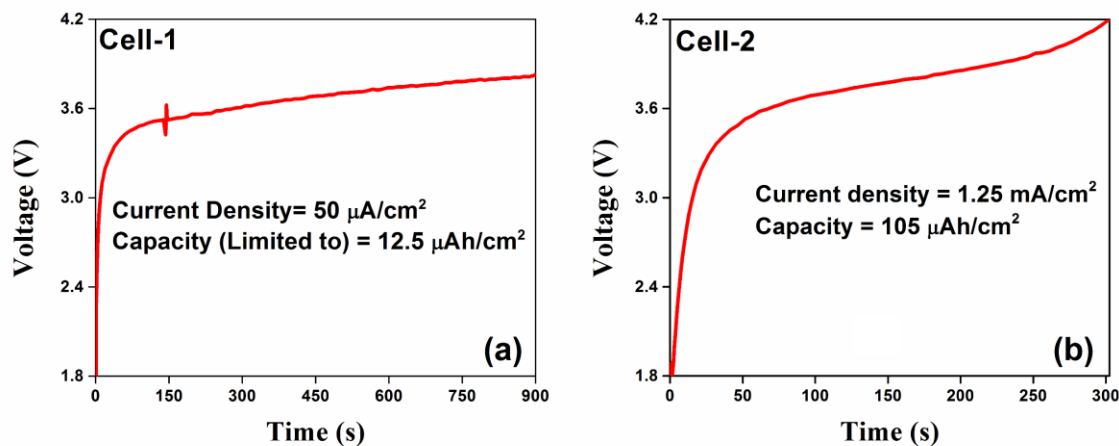
Figure 6.7. FIB fabricated nanobattery electrochemical charging profile at different current densities of (a) capacity limited to 12.5 µAh/cm^2 and (b) voltage limited to 4.2 V cut-off.

6.2.6. Discussion

Of all steps in the FIB fabrication of a nanobattery, the most critical considerations are the use of low beam current and dwell time to minimize damage.[135] During the fabrication process, proper care must be taken to make contact between the cathode current collector and the grid properly. It is similarly important to maintain the micromanipulator contact to the anode; as seen in Figure 6.7a, at around 150s, a spike in the electrochemical data corresponds to a vibration induced contact issue with the anode. Given the potential for instability of the micromanipulator-anode contact, the in situ testing time is minimized by limiting the nanobattery capacity, in turn reducing the charging time. If the voltage profile is not consistent with the thin film battery, the cleaning procedure is repeated. This cleaning procedure decreases the thickness of the nanobattery cross-section, so the current density should be corrected accordingly. It is noted that ion beam damage cannot be completely avoided and it is limited to between a few nm to a maximum of 25 nm into the surface as calculated from ion scattering simulations SRIM program for 30 keV Ga$^+$ into the electrode materials.[151] Low energy processing can reduce the damage to a large extent.[19] The FIB process demonstrated here is unique, and fabrication, manipulation and in situ testing of

101

nanodevices is enabled FIB-SEM dual beam systems. It is possible to extend the process to any other battery chemistries and other nanoscale devices.
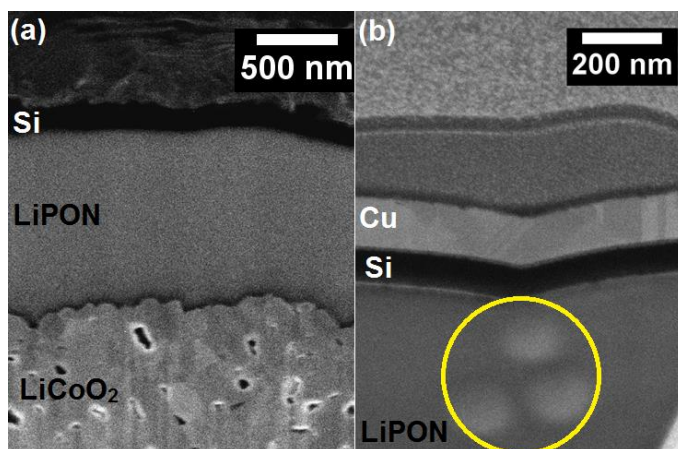
Figure 6.8. SEM images nanobattery cross-section (a) undamaged LiPON layer and (b) imaging at higher magnification induced damaged in LiPON layer indicated by the circle.

6.3 Summary and future outlook

Here we have described the current state of in situ testing for solid-state battery interfaces, and a refined procedure for the production of nanobatteries for testing within the TEM. Indeed, the number of feasible methods for performing such testing is limited, due to the complex nature of deconvoluting signals from buried material as well as the probe sensitivity associated with these materials. With the drive for lithium-metal-based devices, these in situ methodologies are further complicated. Indeed, to fully permit quantitative electrochemical analyses of Li-metal/SSE interfaces, a combination of the in situ methodologies discussed here must be combined with the cryogenic techniques described in Chapter 5 to preserve lithium metal for testing. Cryogenic TEM will also be required for imaging within the TEM, though kinetic considerations will complicate the interpretation of results. Preliminary efforts will be described in Chapter 7.

However, one characterization technique has yet to be utilized for solid-state in situ measurements: solid state NMR. Solid-state NMR provides the added benefit of being able to characterize changes in local structure of disordered solids, of particularly interest to LiPON-type

electrolytes. This difficulty is primarily due to the requirement of a high speed spinning sample (on the order of kHz). As such, attempts to make physical contact between the spinning rotor and an electrochemical source have been limited. Future work will explore the possibility of combining in situ testing with remote energy transmission to the rotor.

Chapter 6, in part, is a reprint of the material as it appears in the MRS Bulletin and the Journal of Visualized Experiments. Wynn, Thomas A.; Lee, Jungwoo Z.; Banerjee, Abhik,; Meng, Ying Shirley, MRS Bulletin, 43 (2018) 768-774 and Lee, Jungwoo Z.; Wynn, Thomas A.; Meng, Ying Shirley; Santhanagopalan, Dhamodaran, Journal of Visualized Experiments, 133 (2018) e56259. The dissertation/thesis author was the co-primary investigator and co-first author of these papers.

Chapter 7. Future work

7.1 Anode/solid electrolyte interface

Cryo-FIB was demonstrated as an essential too for the preservation of alkali metal anodes and was similarly successful in the preservation of cross-sections of crystalline PEO such that they could be observed in HRTEM. This work emphasizes the importance of cryogenic techniques for the preparation of any crystalline polymers and interfaces for TEM analysis. Since Li metal anodes remain a major focus of research efforts, Li-metal/SSE interfaces are being pursued using the cryo-EM methodologies described. As mentioned in past work, future HRTEM studies may be performed on a variety of solid-state interfaces. In the Li metal study performed, a LiCoO$_2$/LiPON/Li-metal thin film battery was successfully cross-sectioned for TEM preparation (Figure 7.1).
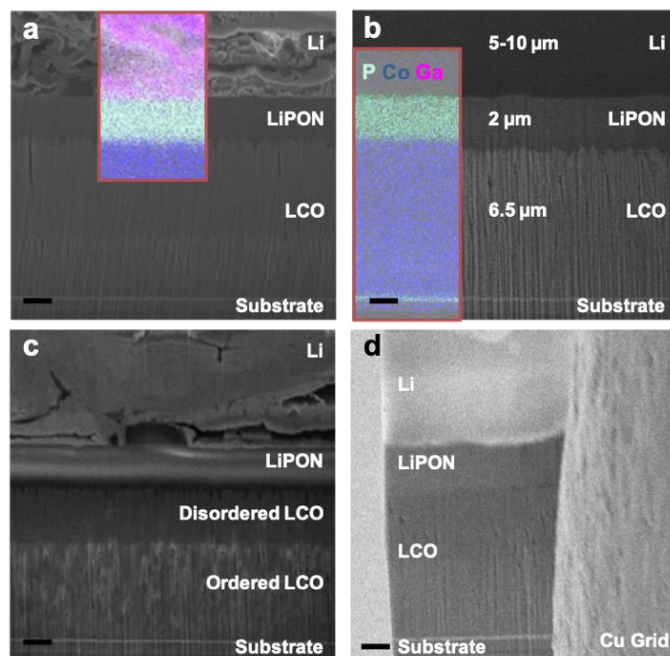
Figure 7.1. SEM image and EDS elemental map of cross-section of pristine Li metal thin film battery prepared at (a) room temperature and (b) under cryogenic conditions (layer thicknesses shown). (c) SEM image of sample after catastrophic failure. (d) TEM lamella of commercial Li metal thin film battery to enable future studies of Li metal/electrolyte interfaces. Scale bars are 1 μm. [102]

Future work will focus on the structure and chemistry of such interfaces. Here, we emphasize the importance of cryo-TEM as well, required by both Li-metal and LiPON alike. LiPON had been shown to be beam sensitive in previous work, clearly decomposing under the electron beam.[135] However, realization of the characterization of Li-metal-containing interfaces requires a complex set of environmental isolation technologies from FIB to TEM. Methods are currently being explored, including the potential to maintain cryogenic temperatures from start to finish, to reduce kinetics of reaction in ambient conditions. However, similar to the biology field, water crystallization continues to be an issue.[152]

7.2 Cathode/solid electrolyte interface

The high cyclability of the thin film battery $LiNi_{0.5}Mn_{1.5}O_4$ (LNMO)/LiPON/Li-metal has brought more focus the Li-LiPON interface. Yet little work has been focused on the LNMO/LiPON interface. Interestingly, when LNMO is coated with LiPON or Li_3PO_4, a large excess capacity (on the order of 20%) is observed during first charge. This is generally associated with $Mn^{3+/4+}$ redox couple at around 3.9V,[21] though in the case of Li_3PO_4 this redox is observed around 2.9V.[153] Interestingly, experimental work has shown that this excess redox is not present when similar cathodes are cycled in liquid electrolytes, and further, the excess capacity remains when LNMO is coated with LiPON and cycled within a liquid electrolyte, decoupling effects of the Li/LiPON interface. Despite being identified as a low-resistance interface, many questions remain regarding the source of the excess Li.[153] Two questions may be pursued from this finding. First, what is the source of the overlithiation of the spinel cathode when in contact with highly lithiated phosphate glasses? It may either be thermodynamic, driven by the varied chemical potential of Li with LiPON versus LNMO. However, if this were the case, what is the source of the irreversibility? Alternatively, it may be a result of processing. RF sputtering is known to

provide some excess heating, which may temporarily modify the phase chemical potential of Li at the interface during heating. Should the Li be inserted in a metastable state, Mn^{3+} formation may drive internal strain via the Jahn-Teller distortion. Last, the distribution of the Li within LNMO is unknown. This may be probed by neutron depth profiling.
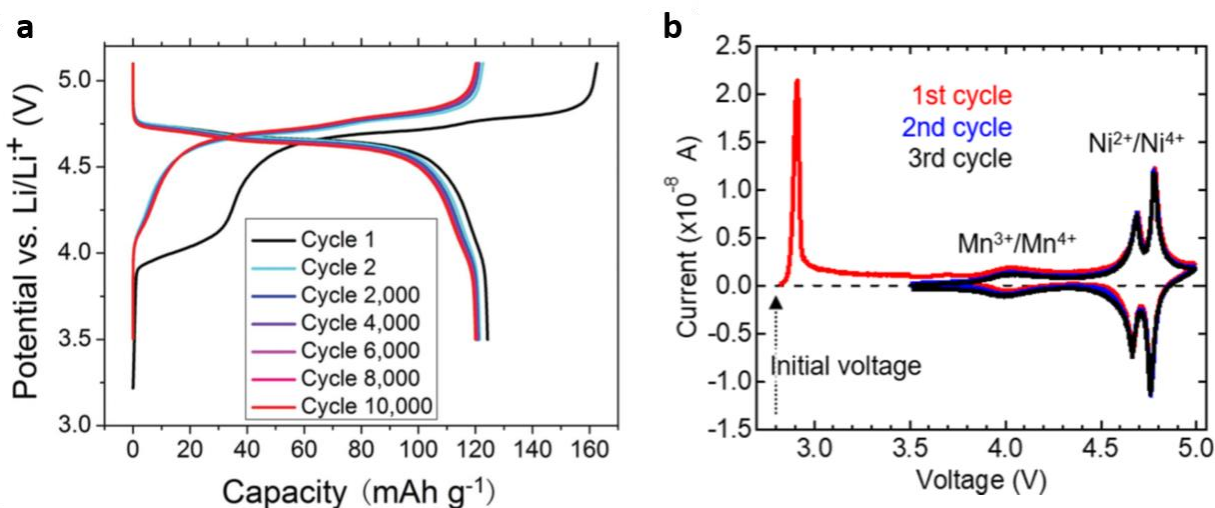
Figure 7.2. (a) Cycling data from an LNMO/LiPON/Li-metal cell[21] and (b) CV from an epitaxial LNMO/Li$_3$PO$_4$/Li-metal cell.[153]

7.3 Exploration of interfaces using in situ TEM methodology

Questions from the previous two sections may be further supported by in situ TEM methodologies described in Chapter 6. Questions of the cathode/electrolyte interface can be more deeply characterized by observing the kinetics of strain evolution of the cathode, dynamics of lithiation and delithiation, and potentially modification of the cathode electrolyte interface (CEI) through spectral analysis via electron energy loss spectroscopy (EELS). These methodologies have been applied to the LiCoO$_2$/LiPON/Li interface in work by Wang, et al. This work found a highly disordered region with reduced lithium kinetics at the interface (Figure 7.3). The decomposition of this interface was roughly predicted by computational work. However, the method for formation remains in question. Results attained from a repeated experiment using LNMO/LiPON/amorphous

silicon (a-Si) chemistry will provide valuable insight into the nature of this overlithiation, and perhaps explain the cause of the decomposition of the $LiCoO_2$ in LiPON-based thin film batteries. Further, chemical mapping of the Ni edge will provide understanding of the delithiation routes present in a fully dense cathode material.
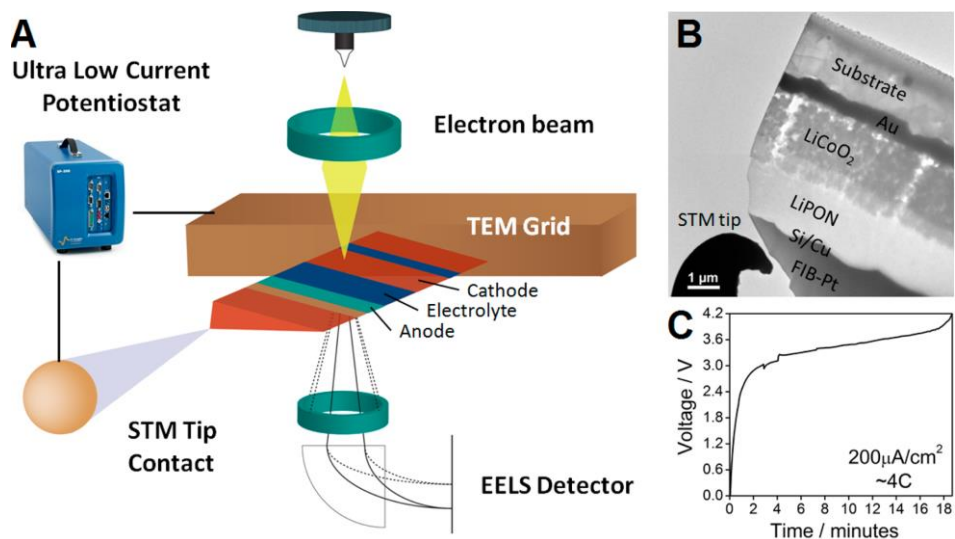
Figure 7.3. (a) Schematic of in situ TEM methodology for all-solid-state nanobatteries, (b) the method implemented in TEM, and (c) a representative charge curve.[130]

This methodology will also provide insight into both anode dynamics as well as the anode/SSE interface, using such as a-Si, Ti, etc. It is important to note that Li-metal cannot be adequately captured dynamically due to the sensitivity of Li metal to probe damage, as discussed in Chapter 5.

7.3 Cryogenic in situ methodology development

With continued interest in Li metal as an anode, new methods of characterization are required. Using the cryo-FIB methodology described in Chapter 5, insight into its plating morphology along with statistical analyses were enabled by preventing damage via FIB.[102] Li

metal was also able to be imaged in HRTEM using cryo-TEM, providing valuable insight into the effect of additives in its plating morphology.[100] However, the field is generally lacking methods for observing and quantifying lithium dynamics, both in nucleation and in growth. We propose development of a combined cryogenic-biasing TEM holder to permit nucleation and growth of Li metal while preserving the Li during imaging under cryogenic temperatures. Such a method will be difficult, as it will need to be adapted to a chip-based formation. Though attempts to do perform such experiments have been achieved in focused ion beam (FIB), shown in Figure 7.4. An idealized system was designed where the general configuration shows the application of a potentiostat to Li metal and a Cu nanowire. To allow dendrite formation, application of a solid electrolyte is required; in this proof of concept, application of N_2 will result in the formation of Li_3N, previously described as a superionic conductor. Such testing will prove essential in capturing the initial states of Li nucleation at the SSE interface.

Figure 7.4. (a) Schematic and (b) experimental configurations, demonstrating lithium plating on an in situ formed Li_3N solid electrolyte. Plating electrochemical profile (c) is consistent with that observed on coin cell Li plating experiments.

References

1   H. Ritchie and M. Roser, Our World Data.

2   R. A. Huggins, Advanced batteries: Materials science aspects, Springer, 2009.

3   M. S. Whittingham, Chem. Rev., 2004, **104**, 4271–4302.

4   Z. Lu, D. D. MacNeil and J. R. Dahn, Electrochem. Solid-State Lett., 2001, **4**, A200–A203.

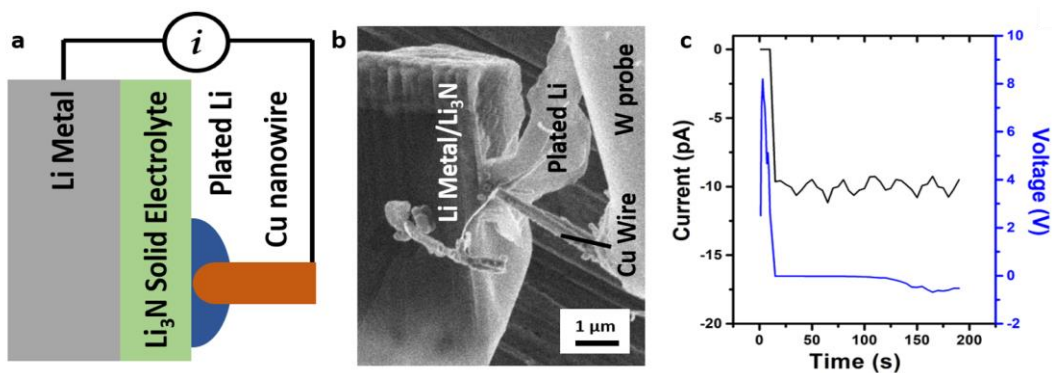5   H. Koga, L. Croguennec, M. Ménétrier, K. Douhil, S. Belin, L. Bourgeois, E. Suard, F. Weill and C. Delmas, J. Electrochem. Soc., 2013, **160**, A786–A792.

6   A. Singer, M. Zhang, S. Hy, D. Cela, C. Fang, T. A. Wynn, B. Qiu, Y. Xia, Z. Liu, A. Ulvestad, N. Hua, J. Wingert, H. Liu, M. Sprung, A. V. Zozulya, E. Maxey, R. Harder, Y. S. Meng and O. G. Shpyrko, Nat. Energy, 2018, **3**, 641–647.

7   J. Hong, W. E. Gent, P. Xiao, K. Lim, D. H. Seo, J. Wu, P. M. Csernica, C. J. Takacs, D. Nordlund, C. J. Sun, K. H. Stone, D. Passarello, W. Yang, D. Prendergast, G. Ceder, M. F. Toney and W. C. Chueh, Nat. Mater., 2019, **18**, 256–265.

8   S. Hy, H. Liu, D. Qian, M. Zhang, B.-J. J. Hwang, Y. S. Meng, D. Qian, B.-J. J. Hwang, Y. S. Meng, M. Duttine, E. Suard, C. Delmas, K.-W. Nam, X.-Q. Yang, J. Liu, C. M. Wang, R. Shahbazian-Yassar, J. G. Zhang, C. M. Wang, A. Mineshige, Y. Uchimoto and Z. Ogumi, Energy Environ. Sci., 2016, **9**, 1931–1954.

9   K. Luo, M. R. Roberts, R. Hao, N. Guerrini, D. M. Pickup, Y.-S. Liu, K. Edström, J. Guo, A. V. Chadwick, L. C. Duda and P. G. Bruce, Nat. Chem., 2016, **8**, 684–691.

10   D. Seo, J. Lee, A. Urban, R. Malik, S. Kang and G. Ceder, Nat. Chem., 2016, **8**, 692–697.

11   K. Luo, M. R. Roberts, R. Hao, N. Guerrini, E. Liberti, C. S. Allen, A. I. Kirkland and P. G. Bruce, Nano Lett., 2016, **16**, 7503–7508.

12   B. Qiu, M. Zhang, L. Wu, J. Wang, Y. Xia, D. Qian, H. Liu, S. Hy, Y. Chen, K. An, Y. Zhu, Z. Liu and Y. S. Meng, Nat. Commun., 2016, **7**, 12108.

13   B. Qiu, J. Wang, Y. Xia, Z. Wei, S. Han and Z. Liu, ACS Appl. Mater. Interfaces, 2014, **6**, 9185–9193.

14   Z. Q. Deng and A. Manthiram, J. Phys. Chem. C, 2011, **115**, 7097–7103.

15   N. Kamaya, K. Homma, Y. Yamakawa, M. Hirayama, R. Kanno, M. Yonemura, T. Kamiyama, Y. Kato, S. Hama, K. Kawamoto and A. Mitsui, Nat. Mater., 2011, **10**, 682–686.

16   I. H. Chu, C. S. Kompella, H. Nguyen, Z. Zhu, S. Hy, Z. Deng, Y. S. Meng and S. P. Ong, Sci. Rep., 2016, **6**, 33733.

17   Y. Zhu, X. He and Y. Mo, ACS Appl. Mater. Interfaces, 2015, **7**, 23685–23693.

18   W. D. Richards, L. J. Miara, Y. Wang, J. C. Kim and G. Ceder, Chem. Mater., 2016, **28**, 266–273.

19   A. Schwöbel, R. Hausbrand and W. Jaegermann, Solid State Ionics, 2015, **273**, 51–54.

20   C. Ma, Y. Cheng, K. Yin, J. Luo, A. Sharafi, J. Sakamoto, J. Li, K. L. More, N. J. Dudney and M. Chi, Nano Lett., 2016, **16**, 7030–7036.

21   J. Li, C. Ma, M. Chi, C. Liang and N. J. Dudney, Adv. Energy Mater., 2015, **5**, 1401408.

22   D. Lin, Y. Liu and Y. Cui, Nat. Nanotechnol., 2017, **12**, 194–206.

23   X. B. Cheng, R. Zhang, C. Z. Zhao and Q. Zhang, Chem. Rev., 2017, **117**, 10403–10473.

24   C. Fang, J. Li, M. Zhang, Y. Zhang, F. Yang, J. Z. Lee, M. H. Lee, J. Alvarado, M. A. Schroeder, Y. Yang, B. Lu, N. Williams, M. Ceja, L. Yang, M. Cai, J. Gu, K. Xu, X. Wang and Y. S. Meng, Nature, 2019, 572, 511–515.

25   K. Kerman, A. Luntz, V. Viswanathan, Y.-M. Chiang and Z. Chen, J. Electrochem. Soc., 2017, **164**, A1731–A1744.

26   A. J. Louli, M. Genovese, R. Weber, S. G. Hames, E. R. Logan and J. R. Dahn, J. Electrochem. Soc., 2019, **166**, A1291–A1299.

27   F. Han, A. S. Westover, J. Yue, X. Fan, F. Wang, M. Chi, D. N. Leonard, N. J. Dudney, H. Wang and C. Wang, Nat. Energy, , DOI:10.1038/s41560-018-0312-z.

28   Y. Zhu, X. He and Y. Mo, J. Mater. Chem. A, 2015, **4**, 1–14.

29   R. Akolkar, J. Power Sources, 2013, **232**, 23–28.

30   C. Monroe and J. Newman, J. Electrochem. Soc., 2003, **150**, A1377.

31   F. Sagane, R. Shimokawa, H. Sano, H. Sakaebe and Y. Iriyama, J. Power Sources, 2013, **225**, 245–250.

32   Ohring, Materials Science of Thin Films, Academic Press, 2002.

33   R. Eason, Pulsed Laser Deposition of Thin Films: Application-Led Growth of Functional Materials, John Wiley & Sons, Inc., 2006.

34   P. Hohenberg and W. Kohn, Phys. Rev., 1964, **136**, B864–B871.

35   M. Born and R. Oppenheimer, Ann. Phys., 1927, **389**, 457–484.

36   W. Kohn and L. J. Sham, Phys. Rev., 1965, **140**, A1133–A1138.

37   D. R. Hartree, Math. Proc. Cambridge Philos. Soc., 1928, **24**, 89–110.

38   J. P. Perdew, J. A. Chevary, S. H. Vosko, K. A. Jackson, M. R. Pederson, D. J. Singh and C. Fiolhais, Phys. Rev. B, 1992, **46**, 6671–6687.

39   D. S. Sholl and J. A. Steckel, Density Functional Theory, John Wiley & Sons, Inc., 2009.

40   V. Pecharsky, P. Zavalij, J. R. Votano, M. Parham and L. H. Hall, Fundamentals of Powder Diffraction and Structural Characterization of Materials, Second Edition, Springer, 2009.

41   D. B. Williams and C. B. Carter, Transmission Electron Microscopy: A Textbook for Materials Science, Springer, 2009, vol. 1–4.

42   N. A. Mara, D. Bhattacharyya, P. Dickerson, R. G. Hoagland and A. Misra, Appl. Phys. Lett., 2008, **92**, 231901.

43   J. I. Goldstein, D. E. Newbury, J. R. Michael, N. W. M. Ritchie, J. H. J. Scott and D. C. Joy, Scanning electron microscopy and x-ray microanalysis, Springer, 2017.

44   L. A. Giannuzzi and F. A. Stevie, Introduction to focused ion beams: Instrumentation, theory, techniques and practice, Springer, 2005.

45   T. L. Burnett, R. Kelley, B. Winiarski, L. Contreras, M. Daly, A. Gholinia, M. G. Burke and P. J. Withers, Ultramicroscopy, 2016, **161**, 119–129.

46   V. I. Bakhmutov, Solid-state NMR in materials science: Principles and applications, CRC Press, 2016.

47   J. B. Goodenough and Y. Kim, Chem. Mater., 2010, **22**, 587–603.

48   J.-M. Tarascon and M. Armand, Nature, 2001, **414**, 359–367.

49   H. Yu and H. Zhou, J Phys Chem Lett, 2013, **4**, 1268–1280.

50   M. Sathiya, G. Rousse, K. Ramesha, C. P. Laisa, H. Vezin, M. T. Sougrati, M.-L. Doublet, D. Foix, D. Gonbeau, W. Walker, a S. Prakash, M. Ben Hassine, L. Dupont and J.-M. Tarascon, Nat. Mater., 2013, **12**, 827–835.

51   K. Luo, M. R. Roberts, N. Guerrini, N. Tapia-Ruiz, R. Hao, F. Massel, D. M. Pickup, S. Ramos, Y. S. Liu, J. Guo, A. V Chadwick, L. C. Duda and P. G. Bruce, J. Am. Chem. Soc., 2016, **138**, 11211–11218.

52   G. Assat and J. M. Tarascon, Nat. Energy, 2018, **3**, 373–386.

53   C. R. Fell, D. Qian, K. J. Carroll, M. Chi, J. L. Jones and Y. S. Meng, Chem. Mater., 2013, **25**, 1621–1629.

54   B. Xu, C. R. Fell, M. Chi and Y. S. Meng, Energy Environ. Sci., 2011, **4**, 2223–2233.

55   A. R. Armstrong, M. Holzapfel, P. Novák, C. S. Johnson, S. H. Kang, M. M. Thackeray and P. G. Bruce, J. Am. Chem. Soc., 2006, **128**, 8694–8698.

56   H. Liu, Y. Chen, S. Hy, K. An, S. Venkatachalam, D. Qian, M. Zhang and Y. S. Meng, Adv. Energy Mater., 2016, **6**, 1502143.

57   D. Qian, B. Xu, M. Chi and Y. S. Meng, Phys. Chem. Chem. Phys., 2014, **16**, 14665–14668.

58   H. Liu, J. Huang, D. Qian, S. Hy, C. Fang, J. Luo and Y. S. Meng, J. Electrochem. Soc., 2016, **163**, A971–A973.

59   G. R. Li, X. Feng, Y. Ding, S. H. Ye and X. P. Gao, Electrochim. Acta, 2012, **78**, 308–315.

60   E. McCalla, M. T. Sougrati, G. Rousse, E. J. Berg, A. Abakumov, N. Recham, K. Ramesha, M. Sathiya, R. Dominko, G. Van Tendeloo, P. Novák and J. M. Tarascon, J. Am. Chem. Soc., 2015, **137**, 4804–4814.

61   C.-C. Wang and A. Manthiram, J. Mater. Chem. A, 2013, **1**, 10209–10217.

62   P. Xiao, Z. Q. Deng, A. Manthiram and G. Henkelman, J. Phys. Chem. C, 2012, **116**, 23201–23204.

63   Y. Gao, X. Wang, J. Ma, Z. Wang and L. Chen, Chem. Mater., 2015, **27**, 3456–3461.

64   F. Kong, R. C. Longo, M.-S. Park, J. Yoon, D.-H. Yeon, J.-H. Park, W.-H. Wang, S. Kc, S.-G. Doo and K. Cho, J. Mater. Chem. A, 2015, **3**, 8489–8500.

65   Y. Gao, J. Ma, X. Wang, X. Lu, Y. Bai, Z. Wang and L. Chen, J. Mater. Chem. A, 2014, **2**, 4811–4818.

66   J. Li, C. Zhan, J. Lu, Y. Yuan, R. Shahbazian-Yassar, X. Qiu and K. Amine, ACS Appl. Mater. Interfaces, 2015, **7**, 16040–16045.

67   J. Liu, S. Wang, Z. Ding, R. Zhou, Q. Xia, J. Zhang, L. Chen, W. Wei and P. Wang, ACS Appl. Mater. Interfaces, 2016, **8**, 18008–18017.

68   B. Li, H. Yan, Y. Zuo and D. Xia, Chem. Mater., 2017, **29**, 2811–2818.

69   A. I. Liechtenstein, V. I. Anisimov and J. Zaanen, Phys. Rev. B, 1995, **52**, R5467.

70   L. Wang, T. Maxisch and G. Ceder, Phys. Rev. B, 2006, **73**, 195107.

71   E. McCalla, A. M. Abakumov, M. Saubanère, D. Foix, E. J. Berg, G. Rousse, M.-L. Doublet, D. Gonbeau, P. Novák, G. Van Tendeloo, R. Dominko and J.-M. Tarascon, Science, 2015, **350**, 1516–1521.

72   M. Saubanère, E. McCalla, J.-M. Tarascon, M.-L. Doublet, M. Saubanere, E. McCalla, J.-M. Tarascon and M.-L. Doublet, Energy Environ. Sci., 2016, **9**, 984–991.

73   Y. Zang, C.-X. Ding, X.-C. Wang, Z.-Y. Wen and C.-H. Chen, Electrochim. Acta, 2015, **168**, 234–239.

74   X. Deng, S. Y. Quek, M. M. Biener, J. Biener, D. H. Kang, R. Schalek, E. Kaxiras, C. M. Firend, X. Deng, S. Y. Quek, M. M. Biener, J. Biener, D. H. Kang, R. Schalek, E. Kaxiras and C. M. Friend, Surf. Sci., 2007, **602**, 1166–1174.

75   S. Verdier, L. El Ouatani, R. Dedryvère, F. Bonhomme, P. Biensan and D. Gonbeau, J. Electrochem. Soc., 2007, **154**, A1088.

76   J. Ma, Y.-N. Zhou, Y. Gao, Q. Kong, Z. Wang, X.-Q. Yang and L. Chen, Chem. - A Eur. J., 2014, **20**, 8723–8730.

77   X. Yuan, Q. Xu, X. Liu, W. Shen, H. Liu and Y. Xia, Electrochim. Acta, 2016, **207**, 120–129.

78   J. Du, Z. Shan, K. Zhu, X. Liu, J. Tian and H. Du, J. Solid State Electrochem., 2015, **19**, 1037–1044.

79   H. Tang, Z. Deng, Z. Lin, Z. Wang, I. H. Chu, C. Chen, Z. Zhu, C. Zheng and S. P. Ong, Chem. Mater., 2018, **30**, 163–173.

80   K. Leung, A. J. Pearse, A. A. Talin, E. J. Fuller, G. W. Rubloff and N. A. Modine, ChemSusChem, 2018, **11**, 1956–1969.

81   E. G. Herbert, W. E. Tenhaeff, N. J. Dudney and G. M. Pharr, Thin Solid Films, 2011, **520**, 413–418.

82   É. Guille, G. Vallverdu, Y. Tison, D. Bégué and I. Baraille, J. Phys. Chem. C, 2015, **119**, 23379–23387.

83   V. Lacivita, A. S. Westover, A. Kercher, N. D. Phillip, G. Yang, G. Veith, G. Ceder and N. J. Dudney, J. Am. Chem. Soc., 2018, **140**, 11029–11038.

84   P. E. Stallworth, F. Vereda, S. G. Greenbaum, T. E. Haas, P. Zerigian and R. B. Goldner, J. Electrochem. Soc., 2005, **152**, A516.

85   N. Mascaraque, A. Durán, F. Muñoz and G. Tricot, Int. J. Appl. Glas. Sci., 2016, **7**, 69–79.

86   T. M. Alam and R. K. Brow, J. Non. Cryst. Solids, 1998, **223**, 1–20.

87   R. K. Brow, J. Non. Cryst. Solids, 2000, 263–264, 1–28.

88   L. Le Van-Jodin, F. Ducroquet, F. Sabary and I. Chevalier, Solid State Ionics, 2013, **253**, 151–156.

89   C. J. Pickard and F. Mauri, Phys. Rev. B - Condens. Matter Mater. Phys., 2001, **63**, 2451011–2451013.

90   K. Pilar, Z. Deng, M. B. Preefer, J. A. Cooley, R. Clément, R. Seshadri and A. K. Cheetham, Phys. Chem. Chem. Phys., 2019, **21**, 10070–10074.

91   M. D. Ediger, J. Chem. Phys., 2017, **147**, 210901.

92   V. Lacivita, N. Artrith and G. Ceder, Chem. Mater., 2018, **30**, 7077–7090.

93   I. Hung, T. Edwards, S. Sen and Z. Gan, J. Magn. Reson., 2012, **221**, 103–109.

94   B. C. Bunker, D. R. Tallant, C. A. Balfe, R. J. Kirkpatrick, G. L. Turner and M. R. Reidmeyer, J. Am. Ceram. Soc., 1987, **70**, 675–681.

95   J. Li, N. J. Dudney, J. Nanda and C. Liang, ACS Appl. Mater. Interfaces, 2014, **6**, 10083–10088.

96   C. S. S. Nimisha, K. Y. Rao, G. Venkatesh, G. M. Rao and N. Munichandraiah, Thin Solid Films, 2011, **519**, 3401–3406.

97   S. F. Swallen, K. L. Kearns, M. K. Mapes, Y. S. Kim, R. J. McMahon, M. D. Ediger, T. Wu, L. Yu and S. Satija, Science (80-.)., 2007, **315**, 353–356.

98   A. Sepúlveda, F. Criscuolo, B. Put and P. M. Vereecken, Solid State Ionics, 2019, **337**, 24–32.

99   K. Murata and M. Wolf, Biochim. Biophys. Acta - Gen. Subj., 2018, 1862, 324–334.

100   X. Wang, M. Zhang, J. Alvarado, S. Wang, M. Sina, B. Lu, J. Bouwer, W. Xu, J. Xiao, J. G. Zhang, J. Liu and Y. S. Meng, Nano Lett., 2017, **17**, 7606–7612.

101   Y. Li, Y. Li, A. Pei, K. Yan, Y. Sun, C. L. Wu, L. M. Joubert, R. Chin, A. L. Koh, Y. Yu, J. Perrino, B. Butz, S. Chu and Y. Cui, Science (80-.)., 2017, **358**, 506–510.

102   J. Z. Lee, T. A. Wynn, M. A. Schroeder, J. Alvarado, X. Wang, K. Xu and Y. S. Meng, ACS Energy Lett., 2018, **4**, 489–493.

103   Y. Jiang, X. Yan, Z. Ma, P. Mei, W. Xiao, Q. You and Y. Zhang, Polymers (Basel)., 2018, 10, 1237.

104   Z. Gadjourova, Y. G. Andreev, D. P. Tunstall and P. G. Bruce, Nature, 2001, **412**, 520–523.

105   N. J. Dudney and B. J. Neudecker, Curr Opin Solid St M, 1999, **4**, 479–482.

106   J. A. Lewis, J. Tippens, F. J. Q. Cortes and M. T. McDowell, Cell Press Rev., 2019, **1**, 845–857.

107   M. M. Besli, S. Xia, S. Kuppan, Y. Huang, M. Metzger, A. K. Shukla, G. Schneider, S. Hellstrom, J. Christensen, M. M. Doeff and Y. Liu, Chem. Mater., 2019, **31**, 491–501.

108   N. Dudney, W. C. West and J. Nanda, Eds., Handbook of Solid State Batteries, World

Scientific, Singapore, 2nd edn., 2016.

109   C. W. Ban and G. M. Choi, Solid State Ionics, 2001, **140**, 285–292.

110   A. Varzi, R. Raccichini, S. Passerini and B. Scrosati, J. Mater. Chem. A, 2016, **4**, 17251–17259.

111   J. Maier, Berichte der Bunsengesellschaft für Phys. Chemie, 1989, **93**, 1468–1473.

112   C. T.-C. W. X.-Q. Y. Y. S. M. D. N. W. Y. M. M. D. Feng Lin, Yijin Liu, Xiqian Yu, Lei Cheng, Andrej Singer, Oleg G. Shpyrko, Huolin L. Xin, Nobumichi Tamura, Chem. Rev., 2017, **117**, 13123–13186.

113   B. L. Mehdi, M. Gu, L. R. Parent, W. Xu, E. N. Nasybulin, X. Chen, R. R. Unocic, P. Xu, D. A. Welch, P. Abellan, J. G. Zhang, J. Liu, C. M. Wang, I. Arslan, J. Evans and N. D. Browning, Microsc. Microanal., 2014, **20**, 484–492.

114   M. L. Taheri, E. A. Stach, I. Arslan, P. A. Crozier, B. C. Kabius, T. LaGrange, A. M. Minor, S. Takeda, M. Tanase, J. B. Wagner and R. Sharma, Ultramicroscopy, 2016, **170**, 86–95.

115   Y. Yuan, K. Amine, J. Lu and R. Shahbazian-Yassar, Nat. Commun., 2017, **8**, 1–14.

116   A. M. Tripathi, W.-N. Su and B. J. Hwang, Chem. Soc. Rev., 2018, **47**, 736–851.

117   Y. Iriyama, T. Kako, C. Yada, T. Abe and Z. Ogumi, Solid State Ionics, 2005, **176**, 2371–2376.

118   Y. Amiki, F. Sagane, K. Yamamoto, T. Hirayama, M. Sudoh, M. Motoyama and Y. Iriyama, J. Power Sources, 2013, **241**, 583–588.

119   T. Kato, T. Hamanaka, K. Yamamoto, T. Hirayama, F. Sagane, M. Motoyama and Y. Iriyama, J. Power Sources, 2014, **260**, 292–298.

120   J. Maier, Prog. Solid State Chem., 1995, **23**, 171–263.

121   N. Sata, K. Eberman, K. Eberl and J. Maier, Nature, 2000, **408**, 946–949.

122   J. Haruyama, K. Sodeyama, L. Han, K. Takada and Y. Tateyama, Chem. Mater., 2014, **26**, 4248–4255.

123   F. S. Gittleson and F. El Gabaly, Nano Lett., 2017, **17**, 6974–6982.

124   L. Miara, A. Windmüller, C. L. Tsai, W. D. Richards, Q. Ma, S. Uhlenbruck, O. Guillon and G. Ceder, ACS Appl. Mater. Interfaces, 2016, **8**, 26842–26850.

125   Z. Wang, J. Z. Lee, H. L. Xin, L. Han, N. Grillon, D. Guy-Bouyssou, E. Bouyssou, M. Proust and Y. S. Meng, J. Power Sources, 2016, **324**, 342–348.

126   E. A. Wu, C. S. Kompella, Z. Zhu, J. Z. Lee, S. C. Lee, I. H. Chu, H. Nguyen, S. P. Ong,

A. Banerjee and Y. S. Meng, ACS Appl. Mater. Interfaces, 2018, **10**, 10076–10086.

127   S. Wenzel, D. A. Weber, T. Leichtweiss, M. R. Busche, J. Sann and J. Janek, Solid State Ionics, 2016, **286**, 24–33.

128   S. Wenzel, S. Randau, T. Leichtweiß, D. A. Weber, J. Sann, W. G. Zeier and J. Janek, Chem. Mater., 2016, **28**, 2400–2407.

129   K. Yamamoto, Y. Iriyama, T. Asaka, T. Hirayama, H. Fujita, K. Nonaka, K. Miyahara, Y. Sugita and Z. Ogumi, Electrochem. commun., 2012, **20**, 113–116.

130   Z. Wang, D. Santhanagopalan, W. Zhang, F. Wang, H. L. Xin, K. He, J. Li, N. Dudney and Y. S. Meng, Nano Lett., 2016, **16**, 3760–3767.

131   D. Ruzmetov, V. P. Oleshko, P. M. Haney, H. J. Lezec, K. Karki, K. H. Baloch, A. K. Agrawal, A. V. Davydov, S. Krylyuk, Y. Liu, J. Huang, M. Tanase, J. Cumings and A. A. Talin, Nano Lett., 2012, **12**, 505–511.

132   H. Masuda, N. Ishida, Y. Ogata, D. Ito and D. Fujita, Nanoscale, 2017, **9**, 893–898.

133   K. Yamamoto, Y. Iriyama, T. Asaka, T. Hirayama, H. Fujita, C. A. J. Fisher, K. Nonaka, Y. Sugita and Z. Ogumi, Angew. Chemie - Int. Ed., 2010, **49**, 4414–4417.

134   Y. Aizawa, K. Yamamoto, T. Sato, H. Murata, R. Yoshida, C. A. J. Fisher, T. Kato, Y. Iriyama and T. Hirayama, Ultramicroscopy, 2017, **178**, 20–26.

135   D. Santhanagopalan, D. Qian, T. McGilvray, Z. Wang, F. Wang, F. Camino, J. Graetz, N. Dudney and Y. S. Meng, J. Phys. Chem. Lett., 2014, **5**, 298–303.

136   P.-H. Chien, X. Feng, M. Tang, J. T. Rosenberg, S. O'Neill, J. Zheng, S. C. Grant and Y.-Y. Hu, J. Phys. Chem. Lett., 2018, **9**, 1990–1998.

137   T. Radetic, A. Gautam, C. Ophus, C. Czarnik and U. Dahmen, Microsc. Microanal., 2014, **20**, 1594–1595.

138   A.-C. Milazzo, A. Cheng, A. Moeller, D. Lyumkis, E. Jacovetty, J. Polukas, M. H. Ellisman, N.-H. Xuong, B. Carragher and C. S. Potter, J. Struct. Biol., 2011, **173**, 404–408.

139   Y. Gong, J. Zhang, L. Jiang, J. A. Shi, Q. Zhang, Z. Yang, D. Zou, J. Wang, X. Yu, R. Xiao, Y. S. Hu, L. Gu, H. Li and L. Chen, J. Am. Chem. Soc., 2017, **139**, 4274–4277.

140   J. Mayer, L. A. Giannuzzi, T. Kamino and J. Michael, MRS Bull., 2007, **32**, 400–407.

141   J. G. Pellerin, J. Vac. Sci. Technol. B Microelectron. Nanom. Struct., 1990, **8**, 1945–1950.

142   S. Rubanov and P. R. Munroe, J. Mater. Sci. Lett., 2001, **20**, 1181–1183.

143   A. Lugstein, B. Basnar and E. Bertagnolli, J. Vac. Sci. Technol. B Microelectron. Nanom. Struct., 2002, **20**, 2238–2242.

144 N. I. Kato, J. Electron Microsc. (Tokyo)., 2004, 53, 451–458.

145 S. Bals, W. Tirry, R. Geurts, Y. Zhiqing and D. Schryvers, Microsc. Microanal., 2007, **13**, 80–86.

146 N. Miyajima, C. Holzapfel, Y. Asahara, L. Dubrovinsky, D. J. Frost, D. C. Rubie, M. Drechsler, K. Niwa, M. Ichihara and T. Yagi, J. Microsc., , DOI:10.1111/j.1365-2818.2009.03341.x.

147 M. Schaffer, B. Schaffer and Q. Ramasse, Ultramicroscopy, 2012, **114**, 62–71.

148 J. B. B. Bates, N. J. J. Dudney, G. R. R. Gruzalski, R. A. a. Zuhr, A. Choudhury, C. F. F. Luck and J. D. D. Robertson, J. Power Sources, 1993, **43–44**, 103–110.

149 Y.-I. Jang, N. J. Dudney, D. A. Blom and L. F. Allard, J. Electrochem. Soc., 2002, **149**, A1442–A1447.

150 B. J. Neudecker, R. A. Zuhr and J. B. Bates, J. Power Sources, 1999, **81–82**, 27–32.

151 J. F. Ziegler, in Nuclear Instruments and Methods in Physics Research, Section B: Beam Interactions with Materials and Atoms, 2004, vol. 219–220, pp. 1027–1036.

152 M. J. Zachman, E. Asenath-Smith, L. A. Estroff and L. F. Kourkoutis, Microsc. Microanal., 2016, **22**, 1338–1349.

153 H. Kawasoko, S. Shiraki, T. Suzuki, R. Shimizu and T. Hitosugi, ACS Appl. Mater. Interfaces, 2018, **10**, 27498–27502.